ABSTRACT

Title of dissertation: Electronic and Magnetic Properties of MnP-Type Binary Compounds

Daniel James Campbell
Doctor of Philosophy, 2019

Dissertation directed by: Professor Johnpierre Paglione
Department of Physics

The interactions between electrons, and the resulting impact on physical properties, are at the heart of present-day materials science. This thesis looks at this idea through the lens of several compounds from a single family: the MnP-type transition metal pnictides. FeAs and FeP show long range magnetic order with some similarities to the high temperature, unconventional iron-based superconductors. CoAs lies on the border of magnetism, with strong fluctuations but no stable ordered state. CoP, in contrast, shows no strong magnetic fluctuations but serves as a useful baseline in determining the origin (from composition, structure, or magnetic order) of behavior in the other materials.

For this work, single crystals were grown with two different techniques: solvent flux and chemical vapor transport. In the case of FeAs the flux method resulted in the highest quality crystals yet produced. Extensive work was then performed on these samples at the University of Maryland and the National High Magnetic Field Laboratory. Quantum oscillations observed in high magnetic fields, in combination

with density functional theory calculations, give insight into the Fermi surfaces of these materials. Large magnetoresistance in the phosphides, but not the arsenides, demonstrates differences in the choice of pnictogen atom that cannot be simply a product of electron count. Angle-dependent linear magnetoresistance in FeP is a sign of a possible Dirac dispersion and topological physics, as has been hinted it in other MnP-type materials. Ultimately, it is possible to examine results for all four compounds and draw conclusions on the role of each of the two elements in the formula, which can be extended to other members of this family.

ELECTRONIC AND MAGNETIC PROPERTIES OF MNP-TYPE BINARY COMPOUNDS

by

Daniel James Campbell

Dissertation submitted to the Faculty of the Graduate School of the
University of Maryland, College Park in partial fulfillment
of the requirements for the degree of
Doctor of Philosophy
2019

Advisory Committee:
Professor Johnpierre Paglione, Chair/Advisor
Professor Nicholas P. Butch
Professor Richard L. Greene
Professor Efrain E. Rodriguez, Dean's Representative
Professor James R. Williams

Foreword

The following is a list of all the papers that I have contributed to during my time as a graduate student, either published or intended for publication, starting with the most recent. Those whose results are covered extensively in this thesis are marked with an asterisk.

*__D.J. Campbell__, J. Collini, K. Wang, B. Wilfong, Y.S. Eo, P. Neves, D. Graf, E.E. Rodriguez, N.P. Butch, and J. Paglione, "Large, Anisotropic, Linear Magnetoresistance in FeP", *in preparation.*

__D.J. Campbell__, Z.E. Brubaker, C. Roncaioli, P. Saraf, Y. Xiao, P. Chow, C. Kenney-Benson, D. Popov, R.J. Zieve, J.R. Jeffries, and J. Paglione, "Pressure-Driven Valence Increase and Metallization in Kondo Insulator $Ce_3Bi_4Pt_3$", *arXiv:1907.09017.* [1]

K. Wang, R. Mori, Z. Wang, L. Wang, J.H.S. Ma, D.W. Latzke, D. Graf, J.D. Denlinger, __D.J. Campbell__, B.A. Bernevig, A. Lanzara, and J. Paglione, "Crystalline-Symmetry-Protected non-Trivial Topology in Prototype Compound $BaAl_4$", *under review.*

Y. Nakajima, T. Metz, C. Eckberg, K. Kirshenbaum, A. Hughes, R. Wang, L. Wang, S.R. Saha, I.-L. Liu, N.P. Butch, __D.J. Campbell__, Y.S. Eo, D. Graf, Z. Liu, S.V. Borisenko, P.Y. Zavalij, and J. Paglione, "Planckian dissipation and scale invariance in a quantum-critical disordered pnictide", *arXiv:1902.01034.* [2]

C. Eckberg, __D.J. Campbell__, T. Metz, J. Collini, H. Hodovanets, T. Drye, P. Zavalij, M.H. Christensen, R.M. Fernandes, S. Lee, P. Abbamonte, J. Lynn, and J. Paglione, "Sixfold enhancement of superconductivity in a tunable electronic nematic system", *arXiv:1903.00986*-accepted, *Nat. Phys.*, October 2019. [3]

S. Ran, I.-L. Liu, Y.S. Eo, __D.J. Campbell__, P. Neves, W.T. Fuhrman, S.R. Saha, C. Eckberg, H. Kim, J. Paglione, D. Graf, J. Singleton, and N.P. Butch, "Extreme Magnetic Field-Boosted Superconductivity" *Nat. Phys.*, 2019. [4]

R.L. Stillwell, X. Wang, L. Wang, __D.J. Campbell__, J. Paglione, S.T. Weir, Y.K. Vohra, and J.R. Jeffries, "Observation of two collapsed phases in $CaRbFe_4As_4$", *Phys. Rev. B* **100** 045152 (2019). [5]

__D.J. Campbell__, C. Eckberg, P.Y. Zavalij, H.-H. Kung, E. Razzoli, M. Michiardi, C. Jozwiak, A. Bostwick, E. Rotenberg, A. Damascelli, and J. Paglione,

"Intrinsic Insulating Ground State in Transition Metal Dichalcogenide $TiSe_2$", *Phys. Rev. Mater.* **3** 053402 (2019). [6]

S. Lee, G.A. de la Pea, S.X.-L. Sun, M. Mitrano, Y. Fang, H. Jang, J.-S. Lee, C. Eckberg, **D.J. Campbell**, J. Collini, J. Paglione, F.M.F. de Groot, and P. Abbamonte, "Discovery of a charge density wave instability in Co-doped $BaNi_2As_2$", *Phys. Rev. Lett.* **121** 147601 (2019). [7]

Z.E. Brubaker, R.L. Stillwell, P. Chow, Y. Xiao, C. Kenney-Benson, R. Ferry, D. Popov, S.B. Donald, P. Söderlind, **D.J. Campbell**, J. Paglione, K. Huang, R. E. Baumbach, R. J. Zieve, and J. R. Jeffries, "Pressure dependent intermediate valence behavior in $YbNiGa_4$ and $YbNiIn_4$", *Phys. Rev. B* **98** 214115 (2018). [8]

H. Hodovanets, C.J. Eckberg, P.Y. Zavalij, H. Kim, W.-C. Lin, M. Zic, **D.J. Campbell**, J.S. Higgins, and J. Paglione, "Single crystal investigation of proposed type-II Weyl semimetal CeAlGe", *Phys. Rev. B* **98** 25132 (2018). [9]

C. Eckberg, L. Wang, H. Hodovanets, H. Kim, **D.J. Campbell**, P. Zavalij, P. Piccoli, and J. Paglione, "Evolution of structure and superconductivity in $Ba(Ni_{1-x}Co_x)_2As_2$", *Phys. Rev. B* **97** 224505 (2018). [10]

***D.J. Campbell**, L. Wang, C. Eckberg, D. Graf, H. Hodovanets, and J. Paglione, "CoAs: The line of 3d demarcation", *Phys. Rev. B* **97** 174410 (2018). [11]

B. Wilfong, X. Zhou, H. Vivanco, **D.J. Campbell**, K. Wang, D. Graf, J. Paglione, and E.E. Rodriguez, "Frustrated magnetism in the tetragonal CoSe analog of FeSe", *Phys. Rev. B* **97** 104408 (2018). [12]

***D.J. Campbell**, C. Eckberg, K. Wang, L. Wang, H. Hodovanets, D. Graf, D. Parker, and J. Paglione, "Quantum oscillations in the anomalous spin density wave state of FeAs", *Phys. Rev. B* **96** 075120 (2017). [13]

C. K. H. Borg, X. Zhou, C. Eckberg, **D.J. Campbell**, S.R. Saha, J. Paglione, and E.E. Rodriguez, "Strong anisotropy in nearly ideal tetrahedral superconducting FeS single crystals", *Phys. Rev. B* **93** 094522 (2016). [14]

Acknowledgments

The first person to thank is my advisor, Johnpierre Paglione, whose support, in terms of funding, advice, and encouragement, made all of this work possible. I came in having never taken a condensed matter class and at most a passing knowledge of what a superconductor was. It says a lot that he was willing to take the time to mentor someone who needed to build up his knowledge from quite a low baseline.

Many people from the Paglione group have also been essential to helping me learn how to be a scientist. Some were directly involved in these projects, including accompanying me on various trips to the High Magnetic Field Laboratory in Tallahassee: former members Chris Eckberg (who gave me my initial training when I joined the group), Kefeng Wang, and Limin Wang (who is responsible for all the density functional theory calculations in this dissertation), current members John Collini, Yun Suk Eo, Halyna Hodovanets, Shanta Saha, and Brandon Wilfong. Of course, everyone else that has passed through or is in the group has either given advice or been a key part of other projects: former members I-Lin Liu, Yasuyuki Nakajima, Renxiong Wang, and Xiangfeng Wang, current members Ian Hayes, Hyunsoo Kim, Wen-Chen Lin, Tristin Metz, Connor Roncaioli, Prathum Saraf, and Mark Zic. Others at UMD also helped a great deal, especially Josh Higgins who was always helpful with cryostat operation and general experimental knowledge.

External collaborators were also essential, most of all Dave Graf from the NHMFL, who dealt with naive or confusing demands over the course of many experiments. There is also David Parker from Oak Ridge National Laboratory, and on

other projects Andrea Damascelli at the University of British Columbia and Sean Kung, Matteo Michiardi, and Elia Razzoli from his group. Something must be said also for Zach Brubaker, Ryan Stillwell, and Jason Jeffries from Lawrence Livermore National Laboratory, who allowed me to work there for a six month sojourn and teach me the basics of diamond anvil cell operation, despite it taking a lot of time away from their own work.

Lastly, I need to thank my family: Dad, Mum, Denis, and Theresa. All of them have experienced the stress of graduate school through me, and are probably just as happy in their own way that I will be finishing as I am myself.

Table of Contents

List of Tables

List of Figures

List of Abbreviations

AC	Alternating current
ADR	Adiabatic demagnetization refrigerator
AFM	Antiferromagnet(-ic, -ism)
AMRO	Angular magnetoresistance oscillations
BZ	Brillouin zone
CVT	Chemical vapor transport
DC	Direct current
DFT	Density functional theory
dHvA	de Haas-van Alphen
EDS	Energy-dispersive x-ray spectroscopy
FFT	Fast Fourier transform
FM	Ferromagnet(-ic, -ism)
LK	Lifshitz-Kosevich
LL	Landau level
MPMS	Quantum Design Magnetic Properties Measurement System
(L)MR	(Linear) magnetoresistance
NHMFL	National High Magnetic Field Laboratory
PM	Paramagnet(-ic, -ism)
PPMS	Quantum Design Physical Properties Measurement System
RRR	Residual resistivity ratio
QC(P)	Quantum critical(-ity, point)
QO	Quantum oscillation
SdH	Shubnikov-de Haas
SDW	Spin density wave
SKEAF	Supercell k-Space Extremal Area Finder
SQUID	Superconducting quantum interference device
UMD	University of Maryland
VSM	Vibrating Sample Magnetometer
XRD	X-ray diffraction

Chapter 1: Introduction

1.1 Foundations

The discovery and application of new materials is fundamental to society, so much so that ancient Western civilization is traditionally divided into epochs named after the primary material of the era: the Stone Age, followed by the Bronze Age, followed by the Iron Age. Skipping ahead a few millenia, the realization of the power of semiconductors, specifically silicon, has led to a technological revolution within the past century that has fundamentally altered the nature of human existence. It is the investigation of new compounds, or of old compounds with new methods, that drives societal advancement.

Basic materials research focuses in depth of the small changes that can have a significant impact on physical properties. This thesis will cover the study of four materials: FeAs, FeP, CoAs, CoP, as well as mixed $Fe_{1-x}Co_xP$ and $Fe_{1-x}Co_xAs$ substitution series. All of these have the same crystal structure, with changes at either the transition metal or pnictogen[1] site.

With this similarities in atomic arrangement and composition come, naturally,

[1]The pnictogens are the elements in Group 15 of the periodic table (the fourth from the right). The ones relevant to this thesis are P, As, Sb, and Bi; N is generally very chemically different in compounds from the others and Mc is a synthetic, extremely radioactive element produced only in very small quantities.

common threads in behavior. The interactions between electrons, and specifically a tendency toward magnetic order, are relevant to describing all of them. For the iron compounds, this means that at low temperatures the electron spins are slightly rotated relative to their closest neighbors, leading to a spiral pattern along a specific direction. The cobalt-based materials do not have a long range magnetic structure, but as will be shown there is clear evidence that in CoAs electrons still have magnetic fluctuations with those those nearby, hinting at a proximity to a phase transition to ordered magnetism. Compared to the others, CoP does not show the same degree of interesting magnetic behavior. But that makes it useful as a nonmagnetic basis for comparison, helping to determine whether the interesting properties in the other compounds come from the emergence of magnetic states, or are related to their structural and elemental makeup.

The interest in magnetic order, from the perspective of this thesis, comes from the states that can emerge as that order is on the verge of disappearing. The first member of what would come to be the iron-based superconductor family was discovered a little over a decade ago [15], and many others have since followed. Structure and composition vary, but common to all is a unit cell of several distinct layers, one of which is made up of bonded Fe and As. Furthermore, most are derived from nonsuperconducting parent compounds with a low temperature magnetic state similar to some of the binaries. When magnetic order is suppressed by applied pressure or chemical doping, an unconventional high temperature superconducting state arises around the quantum critical point (QCP) of the phase diagram where the transition goes to zero temperature [16]. "Unconventional" means that

the electron-electron pairing mechanism that opens the superconducting gap is not the phonon-mediated seen in the vast majority of materials and described by the Bardeen-Cooper-Schrieffer theory. Instead, evidence has accumulated that magnetic interactions are critical to opening a superconducting gap.

Transition temperatures in the iron superconductors can exceed 50 K, while typical transition temperatures for conventional materials are below 20 K. Another family of unconventional superconductors is the heavy fermion materials, so called because electron-electron interactions lead to effective electron masses orders of magnitude higher than the rest mass. The phase diagram looks similar; when magnetic order is suppressed, unconventional superconductivity emerges and increases in temperature, though in this case with transition temperatures below 5 K. The case of the other high temperature superconducting family, the cuprates, first discovered in the 80s, also follows this pattern. The difference is that it is charge order or the pseudogap phase that are often suppressed, though magnetism plays a role in these materials as well [17], though there are indications of magnetic fluctuations or order in the cuprates as well. It seems in all these materials that there is a remnant energy waiting to be applied to correlated electron effects. If it is not taken up by magnetic order, then some other interesting state ought to emerge. This knowledge also motivated the Fe-Co substitution work to be presented. Knowing that the Fe end members are magnetically ordered and the Co ones are not, there must be a point at which the system loses long range order.

The MnP-type compounds offer the chance to isolate the transition metal-pnictogen layer that is crucial to the iron-based superconductors. It has also been

known for decades that many of the binaries take on a similar magnetic ordering to that seen in the parent compounds to the iron superconductors. For that reason researchers quickly jumped on them after the importance of the iron pnictide superconductors began to be understood. In two cases, a similar effect was observed. CrAs and MnP, both helimagnetic at low temperature, became superconductors under pressure when magnetism disappeared [18–21]. While transition temperatures for both were found to be less than 3 K, more work with other MnP-type compounds, especially those with strong magnetic interactions, was clearly of importance.

1.2 The MnP-Type Structure

The structure that the four compounds to be explored in this work take on is an orthorhombic[2], *Pnma* structure, known as the MnP or B31 type. A depiction is in Fig. 1.1, and the full list of materials with this structure is given in Table 1.1 along with lattice parameters and, in the case of long range magnetic order, transition temperatures. The structure is a distortion of the hexagonal NiAs structure in which both the transition metal and pnictogen atom are displaced and the overall symmetry lowered [22]. Several more of the possible transition metal-pnictogen compounds take the original hexagonal structure, and there are some materials (CrAs, CoAs, and from work in the Appendix possibly RhAs) that transition between the two at temperatures of roughly 1000 °C [23].

The basic properties and some crystal growth information for these compounds were well described starting in the 1960s, primarily by the group at the University

[2]Meaning that the unit cell is a rectangular box, with all three axes having a different length.

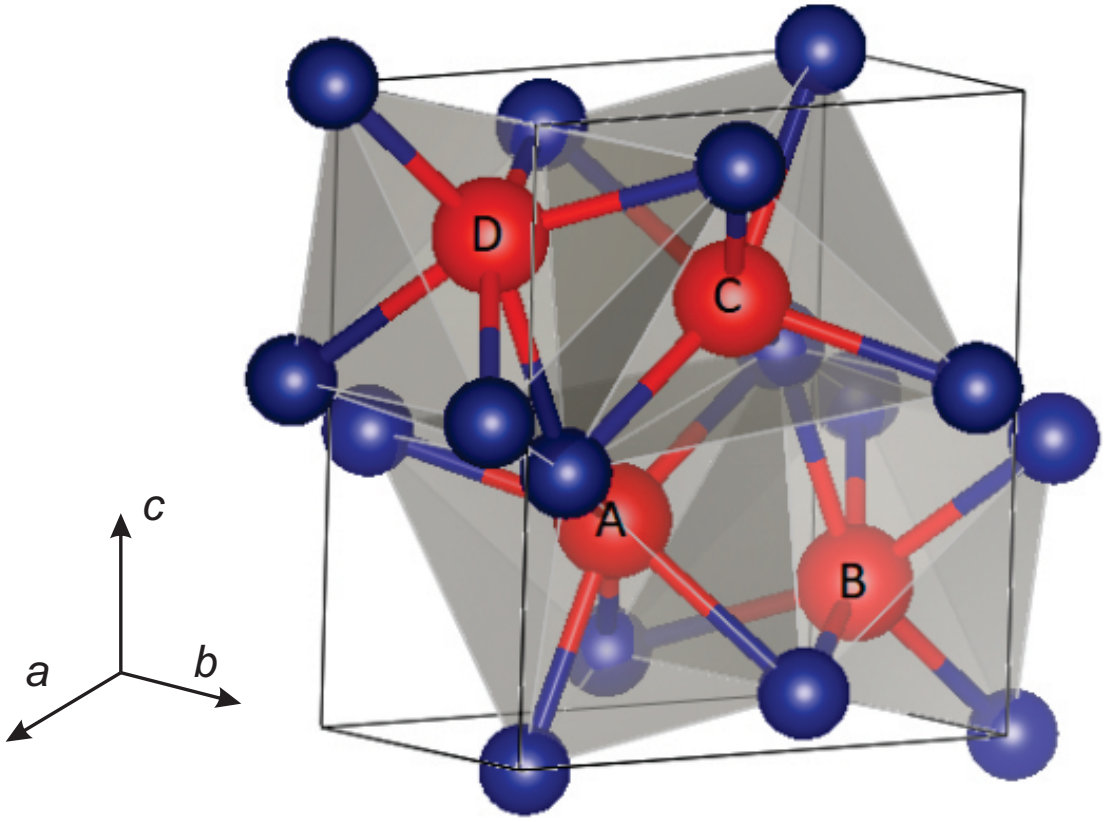

Figure 1.1: Depiction of the MnP (B31) type structure (*Pnma*, space group no. 62), showing octahedral coordination of the pnictogen (blue) atoms around the transition metal (red). There are four formula units per unit cell. Taken from Ref. [32].

of Oslo [24–28]. Further work was done to examine the magnetic ordering present in FeAs, FeP, CrAs, and MnP [29–31]. After a lull, these materials received renewed interest with the discovery of the high-temperature iron pnictide superconductors in 2008 [15] for the reasons outlined earlier in this chapter.

While similarities between the MnP-type binaries and the Fe-based superconductors have been highlighted so far, there are some differences. Arsenic atoms are tetrahedrally coordinated to Fe in the high-T_c pnictides, but form octahedra around the transition metals in the MnP structure. The lower symmetry of the crystal structure also results in different Fe-As bond lengths Additionally, only three of the orthorhombic compounds have been found to superconduct, and none at high temperatures: WP at 0.7 K [33], CrAs at 2.2 K and 1 GPa of applied pressure [18, 34], and MnP at about 1 K and 8 GPa [20]. Despite T_c values more than an order of magnitude lower than the multicomponent Fe-based materials, the results of high pressure measurements are intriguing. Beyond inducing superconductivity, applying pressure to CrAs and MnP also monotonically decreases the onset temperature of magnetic order, which ultimately disappears completely in a manner similar to the quantum critical physics seen in other material families [21]. When this happens for the iron-based, heavy fermion, or cuprate superconductors, it is an indicator that Cooper pairing is driven by magnetic fluctuations or correlated electron physics [35]. This would explain why T_c typically reaches a maximum value just after suppression of SDW order; fluctuations are still strong, but are working to stabilize superconductivity rather than magnetism.

Another reason for interest in MnP-type materials is that the crystal structure

Formula [Ref.]	a (Å)	b (Å)	c (Å)	Magnetic Order?
CrP [36]	5.362	3.113	6.018	No
CrAs* [37]	5.649	3.463	6.212	AFM, 264 K
CoP [This work]	5.08	3.28	5.59	No
CoAs* [This work]	5.28	3.49	5.87	No
FeP [This work]	5.10	3.10	5.79	AFM, 120 K
FeAs [This work]	5.44	3.37	6.02	AFM, 70 K
MnP [20]	5.26	3.17	5.92	FM, 291 K and AFM 50 K
MnAs[a] [38]	5.72	3.676	6.379	No[b]
MoAs [39]	5.97	3.36	6.41	No
RhAs* [This work]	5.65	3.60	6.06	No
RhSb [This work]	5.97	3.87	6.34	No
RuP [36]	5.520	3.168	6.120	No
RuAs [40]	5.717	3.338	6.313	No
RuSb [41]	5.961	3.702	6.580	No
VAs [40]	5.850	3.366	6.289	No
WP [33]	5.722	3.243	6.211	No

Table 1.1: Lattice parameters and information about magnetic ordering for MnP-type compounds. Those marked with an asterisk transition at high temperatures to the NiAs structure (for RhAs this is not known definitively, but suspected-see the Appendix). AFM stands for "antiferromagnetic" and FM for "ferromagnetic".

[a]Only from 40-120 °C, hexagonal NiAs structure at room temperature.
[b]FM in the NiAs structure at room temperature and below.

is nonsymmorphic. A symmorphic structure is one in which all symmetry operations, barring translational ones, leave a single point fixed. In contrast, nonsymmorphic symmetry operations do not leave any part of the unit cell fixed. This leads to further degeneracies in the Brillouin zone (BZ) [32]. These degeneracies, and the protected crossings between different bands that can result from nonsymmorphic symmetry, can produce topological phases. Topology has received significant recent attention in the condensed matter community, because topologically states (of any origin) are more robust to perturbations. For that reason materials with topological properties are one potential route to qubits to be used in quantum computers, as any topological qubits could be much more robust to outside perturbations. Any

potential interplay between topological properties and superconductivity is also of interest.

Work in magnetic fields has led to further signs of topological physics in the B31 group. Linear magnetoresistance near the ordered magnetism-superconductivity crossover in CrAs was linked to a "semi-Dirac" dispersion near the Fermi energy E_F. A typical Dirac k-space dispersion is linear, resulting in massless quasiparticles that are described by different physics than typical electrons or holes with a quadratic dispersion. Linear dispersions are commonly seen in materials with small Fermi surface pockets termed Dirac or Weyl (in the case of additional broken symmetries) semimetals. A semi-Dirac dispersion is linear in one direction but parabolic in the other [19]. The existence of a semi-Dirac point seems to be common to all materials in this class. It was also reported in the same paper that CrP had a semi-Dirac point at the same point in k-space located further from E_F, and density functional theory (DFT) calculations for CoAs done for work related to Ch. 6 have found the same for that material.

1.3 This Work

This chapter has laid out the basic concepts motivating this work. Chapter 2 will cover the theoretical grounding needed to understand the results to be presented. Chapter 3 will go over sample synthesis and the types of experiments subsequently performed on samples. Each of Chapters 4-7 will focus on a specific material: FeAs, FeP, CoAs, and CoP, in that order. Chapter 8 will briefly look at the effect of

chemical substitution with $Fe_{1-x}Co_xP$ and $Fe_{1-x}Co_xAs$. Different growth methods will be compared, as well as basic physical properties that had not been previously reported. The behavior of these compounds in high magnetic fields will be treated in depth, especially quantum oscillatory phenomena in the arsenides and CoP, and the large, anisotropic magnetoresistance of both of the phosphides. While the materials are all related, the work done and discoveries made about each are not all exactly the same. In the Conclusion, the main findings and unifying themes will be recapitulated and ideas for future experiments suggested. The Appendix will round up related work, on the Rh-based pnictides and WP, that was motivated by the main results but not pursued to a sufficient degree to merit a standalone chapter.

Chapter 2: Theoretical Background

The behavior described the main section of this thesis, Chapters 4-8, will cover a broad scope of physics of magnetism and magnetic fields. This chapter will outline those concepts in advance, before more detail is added when discussing specific materials. The first thing to cover is the role of magnetic fluctuations and the type of magnetic order seen in these materials. This will be followed by a discussion of magnetoresistance, a term referring to change of a material's resistance in field. Related to magnetoresistance (and, more broadly, the effects of magnetic fields) is the phenomenon of quantum oscillations, the inverse field-periodic behavior seen in many quantities (such as resistance) that has its origin in the quantization of energy levels by an applied field. The techniques to measure the quantities to be described here will be covered in the next chapter.

2.1 Magnetic Ordering

In a sense, magnetism was the first quantum effect harnessed by humans, with the discovery of ferromagnetic minerals and their use for navigation in the form of compasses guided by the Earth's magnetic field. Of course, it took a few thousand years for the accompanying theoretical explanation of magnetism. That being said,

the gap between the discovery and mathematical formulation of gravity is even larger. Humans are not only experimentalists to take advantage of magnetism; birds, bats, bacteria, and other organisms can sense the Earth's magnetic field internally and use it for orientation.

A thorough treatment of magnetism is found in Ref. [42], and a very condensed version will be given here. Magnetic order is the coherent alignment of spins within a lattice. In paramagnetic or diamagnetic materials, there is no spontaneous order. They can only respond to an external field by either aligning or antialigning with it, respectively. However, in the absence of field spins will be randomly oriented, with interactions between spin sites too weak to generate a consistent structure. In contrast, ferromagnetic, ferrimagnetic, and antiferromagnetic materials are characterized by long range ordering that results from interactions between neighbors [43], though often it takes an external field to be able to measure them[1].

Ferromagnetic materials have a spontaneous magnetization below the Curie temperature T_C, coming from the positive alignment of all the spins [Fig. 2.1(a)]. Ferrimagnetism is similar, except that instead of a single magnetic structure there are two, intertwined with each other. Moments on the two lattices point in opposing directions, but with different magnitudes, and so there is still a nonzero magnetization [Fig. 2.1(b)]. The oldest known magnetic mineral, Fe_3O_4 or magnetite, is actually a ferrimagnet. The distinction between the two can only be seen with probes like neutron scattering that can probe the magnetic structure on each site,

[1]In spin glasses, moments "freeze" into locked positions at low temperatures. However, the alignments are random, hence the term glass, and so they are better described as disordered magnets.

rather than a bulk measurement such as magnetic susceptibility.

Antiferromagnets can in one sense be thought of as a specific case of ferrimagnets. In AFMs, the net magnetization approaches zero below the transition temperature, as the spins combine to cancel each other out [Fig. 2.1(c)]. The transition temperature is referred to as the Néel temperature, T_N. In the simplest picture, spins alternate between being up and down at each neighboring site, though in multiple dimensions a material may have an AFM arrangement in one direction, but a full alignment of moments in another. More complicated structures that still result in zero net magnetization, helimagnets and spin density waves [Fig. 2.1(d) and (e)], will be treated in more depth in the forthcoming section.

Magnetic order and a tendency toward it are critical to describing the behavior the MnP-type pnictides. This should comes as no surprise: only five elements are magnetically ordered at room temperature, and four of them (AFM Cr and FM Fe, Co, and Ni) are in the middle of the $3d$ block[2]. As mentioned in the introduction, the competition between ordered magnetism and superconductivity under pressure in MnP and CrAs has lead to speculation about potential quantum criticality or an unconventional superconducting pairing mechanism [21, 44]. MnP can order magnetically in several different ways depending on temperature, pressure, and applied field. The materials to be described here-CoAs, CoP, FeAs, and FeP-all have some relation to magnetism. The first two are paramagnetic but sits on the border of ferromagnetism, while the latter two have similar antiferromagnetic

[2]The other is Gd, which with $T_C = 292$ K may technically not quite count as "room temperature" magnetism.

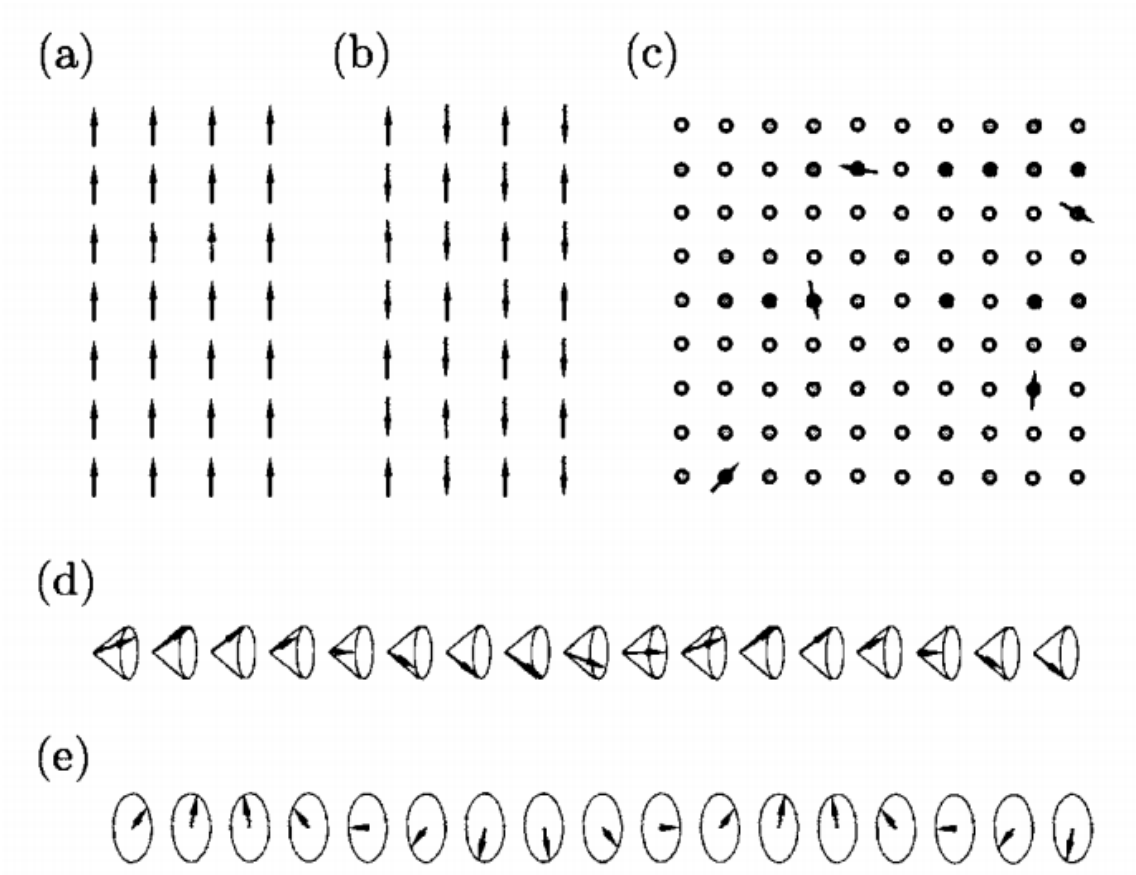

Figure 2.1: Illustrations of different kinds of magnetic structures. (a) Ferromagnetism, where all spins point in the same direction. (b) Antiferromagnetism, where spins point in opposite directions in a specific pattern, resulting in zero net magnetization. (c) A spin glass, where spins lock into place below the transition temperature, but with an overall random orientation. (d) Spiral magnetism, where the moment rotates with some canting into the propagation direction (e) Helical magnetism (or helimagnetism), where the moment rotates in a plane perpendicular to the propagation direction. Note that various arrangements within each of these categories are also possible. Taken from Ref. [42].

orderings to CrAs and MnP.

2.1.1 Antiferromagnetism: Helimagnetism and Spin Density Waves

Four transition metal-pnictogen binaries are antiferromagnetically ordered at low temperatures [29]: CrAs (T_N = 264 K) [18], FeAs (T_N = 70 K) [24], FeP (T_N = 120 K) [31], and MnP (T_N = 50 K) [45]. In the last of these, the story is more complicated, as it actually first enters a ferromagnetic state at 291 K and below about 100 K can have one of five different magnetic orderings, with first or second order phase transitions between them which occur at different combinations of temperature with applied field direction and magnitude. But at base temperature and low field, it takes on a "screw" structure similar to helimagnetic state of CrAs and FeP [29].

Helimagnetism takes its name from the helical shape traced out by the magnetic moments at each as one moves along the propagation direction. The spins at neighboring sites differ in direction by a turn angle. One way of viewing FM or AFM, in fact, is as helimagnets with turn angles of 0° or 180°, respectively [42]. Such a state results from competition between FM and AFM interactions, leading to a final state somewhere between the two. The helimagnetism in the binary pnictides is actually a bit more complicated than this description. It consists of two moments, rather than one, in the *ab* plane, that propagate along the *c*-axis [29]. These moments have different magnitudes, but there is a constant phase difference between them, meaning they have the same turn angle when moving to the next

Formula	T_N (K)	$\mathbf{q}/2\pi$	$\Delta\phi$ (°)	Average moment (μ_B)
CrAs	264	0.353	-126	1.73
MnP	50	0.112	16	1.58
FeP	120	0.2	169	0.42

Table 2.1: Quantities relevant to the double helical magnetic state of several B31 compounds. $\mathbf{q}$ is directed solely along the c-axis in each case. Data primarily from Ref. [29].

site along the c-axis. Of the four transition metal sites in the B31 unit cell, two are associated with each of the two moments. A full description of the magnetic state only requires knowledge of the size of the moments, the propagation wavevector $\mathbf{q}$,[3] and the phase difference between the two moments $\Delta\phi$. $\mathbf{q}$ is the quotient of the crystallographic structural unit cell length and the magnetic structural unit cell length; put differently, $1/q_i$ is the number of unit cells covered in each crystal direction before the magnetic structure begins to repeat. If each component of $1/q_i$ is a whole number, the magnetic structure is termed "commensurate" with the lattice, but incommensurate structures are also common in antiferromagnets. Relevant values for the helimagnetic state of CrAs, MnP, and FeP from Ref. [29] are given in Table 2.1. The phase differences close to $\pm 180°$ in CrAs and FeP mean AFM interactions are dominant, while the value near 0° in MnP indicates strong FM fluctuations, logical given the transition to a FM state at higher fields or temperatures. The moments are also much larger in CrAs and MnP; this can be linked to their higher transition temperatures, perhaps a sign that FeP could have its magnetic state more easily suppressed with pressure.

[3]Where their orientation is important, vector quantities will be in bold lettering throughout this work. Otherwise, they will be written with normal font.

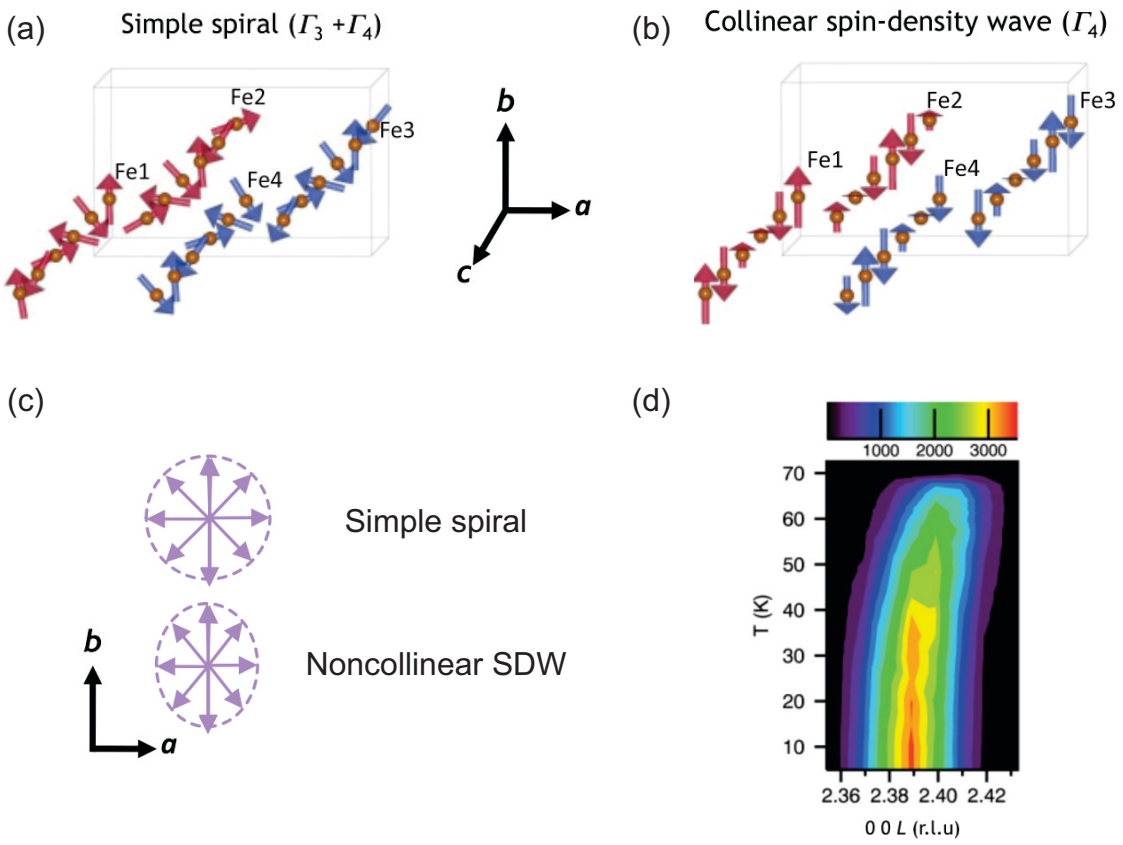

Figure 2.2: (a) A spiral (or helimagnetic) magnetic ordering depicted to fit results for FeAs. Note that there are two separate lines of propagation along the c-axis with a phase difference between them. (b) A collinear spin density wave, in which spins do not rotate but rather change magnitude along [001]. The actual antiferromagnetic state was found to be noncollinear SDW, which corresponds to the state depicted in (b) with the spins rotated to point in between the a- and b-axes. (c) The projection of the simple spiral and noncollinear SDW spins onto the ab plane; the former is circle, the latter an ellipse. (d) Neutron scattering data showing the change in the c-axis component of the ordering vector $\mathbf{q}$ with temperature. The value of about 2.39, not easily written as a fraction, means that the magnetic structure is incommensurate with the lattice structure. All elements of this figure are taken from Ref. [46].

It was initially thought that FeAs took on the same magnetic structure as the other three magnetic B31 materials [24], as it was observed to be antiferromagnetic and had obvious compositional and structural similarities to them. Figure 2.2(a) illustrates a spiral structure on the FeAs lattice [46]. More in-depth neutron scattering work, however, has shown that FeAs is better described by a noncollinear spin density wave (SDW) order [46], similar to that of Fig. 2.2(b) except that moments are tilted in the ab plane. This means that instead of rotation in the ab plane of the two moments, they always point in the same direction but have a differing amplitude at different points along the c-axis. The reason there is a noticeable moment in both the a- and b-axis directions is because the moments point at an angle between the two, resulting in a projection along each principle axis [Fig. 2.2(c)].

2.1.2 Near Ferromagnetism and Magnetic Fluctuations

Many materials experience significant magnetic fluctuations, even if they never reach an ordered magnetic state. They are termed "nearly magnetic". In such a case spins may interact over a finite distance, but there is no coherent structure across the entire sample. Frequently, nearly magnetic materials are closely connected to others that are ordered. A simple example is Pd, which sits under ferromagnetic Ni on the periodic table. As a film or 1D wire, it can display ordered magnetism [47]. In bulk, however, it is paramagnetic but with indications of strong fluctuations. A more exoctic case is the spin-triplet superconductor UTe_2, which has many commonalities to other U-containing ferromagnets, but seems to sit just on the wrong side of the

FM-PM dividing line [48]. In some ways nearly magnetic materials may be more interesting than ordered magnets. After all, it has been established that interesting physics often arises near the suppression of a magnetic transition, as in the case of CrAs and MnP. Studying materials dominated by short range interactions but without an overall structure may skip the need to suppress a strong ordered state.

To appreciate how fine the division between FM and nearly FM materials is, it is useful to look at the Stoner theory of ferromagnetism. It applies to itinerant ferromagnets, where FM arises from partial filling of energy bands (as in the d-electron transition metals), rather than the localized moments coming from the atoms that lead to magnetism in the rare earths. The condition for a Stoner ferromagnet is $\mu_0\mu_B \mathrm{I} g(\mathrm{E}_F) \geq 1$ [42], where μ_0 is the permeability of free space, μ_B a Bohr magneton, I the "Stoner parameter", which represents the Coulomb interaction between itinerant electrons, and $g(\mathrm{E}_F)$ is the density of states at the Fermi energy. This inequality comes from consideration of the energy savings obtained in the process of spin-splitting bands in the absence of field.

In a material with an initially equal number of up and down spins ($n_\uparrow = n_\downarrow$) the energy cost of flipping all spins (from, say, down to up) within a small energy range δE of the Fermi energy E_F is $\frac{1}{2} g(\mathrm{E}_F)(\delta \mathrm{E})^2$. The energy savings come from the change in magnetization $M = \mu_B(n_\uparrow - n_\downarrow)$. The energy of the magnetic field is $\frac{1}{2}\int \mathbf{H}\cdot\mathbf{B}\ \mathrm{dV}$. In a material this is $-\mu_0 \mathrm{I} M^2 = -\mu_0\mu_B^2 \mathrm{I}(n_\uparrow - n_\downarrow)^2$. After flipping the spins, $n_\uparrow = \frac{1}{2}(n + g(\mathrm{E}_F)\delta E)$ and $n_\downarrow = \frac{1}{2}(n - g(\mathrm{E}_F)\delta E)$. Therefore the overall energy change $\Delta E = \frac{1}{2} g(\mathrm{E}_F)[(\delta E)^2(1 - \mu_0\mu_B^2 \mathrm{I} g(\mathrm{E}_F)]$. Spontaneous magnetization is only possible when ΔE is not positive; i.e., when $\mu_0\mu_B^2 \mathrm{I} g(\mathrm{E}_F) \geq 1$. The threshold value can be

reached (or nearly reached) with a large density of states at the Fermi energy and a large Stoner parameter. The definition of the latter has been rather vague so far, and it is an overall complicated quantity. It can be theoretically calculated, however, and essentially represents the strength of the exchange interaction between electrons. Multiplied by E_F, the Stoner criterion essentially says that ferromagnetism occurs when there are a large number of electrons at the Fermi energy strongly interacting with each other, a conclusion that is not too surprising.

Using the Stoner criterion, it is possible to judge how close a material lacking order lies to a FM instability. One way to do this with experimentally measurable quantities is the dimensionless Wilson ratio

$$R_W = \frac{4\pi^2 k_B^2 \chi_0}{3\mu_0 (g_e \mu_B)^2 \gamma} \tag{2.1}$$

Here k_B is the Boltzmann constant, χ_0 the 0 K spin susceptibility and g_e the electron g-factor. Note that calculating R_W involves quantities obtained through specific heat and magnetization measurements, which makes sense since those quantities are most sensitive to the behavior of electrons in the system. R_W can in fact be reformulated as the Stoner factor Z = 1-$\frac{1}{R_W}$. R_W is unity (and Z = 0) for a free electron gas. Larger (smaller) R_W (Z) values mean stronger FM fluctuations: in Pd R_W = 6–8 [49], for $BaCo_2As_2$, thought to be near a magnetic quantum critical point, it is 7–10, depending on field orientation [50].

An Arrott plot can be used to determine whether a material is FM, and how close it may be to the crossover [49]. If a plot of M^2 vs. H/M has a positive y-

intercept, then there exists a spontaneous magnetization in zero field [12]. Such a plot is a simple way of visualizing and assessing the presence of long range order. An example of an Arrott plot, taken from Ref. [51], is given in Fig. 2.3.

2.2 Magnetoresistance

As has just been seen, the interactions between electrons can generate interesting magnetic phenomena. Reversing this in a way, magnetic fields can change the behavior of the electrons in a lattice. Beginning from the simplest considerations, the Lorentz force on a charged particle in an electric and magnetic field is

$$\mathbf{F} = q\Big(\mathbf{E} \ + \ \mathbf{v} \ \times \ \mathbf{B}\Big) \tag{2.2}$$

In the presence of only a magnetic field, a free electron will be accelerated in a direction perpendicular to its velocity and the field. Thus it will execute a circular orbit in the plane normal to $\mathbf{B}$[4]. Unsurprisingly, this changes substantially for an electron in a solid, under the influence of an applied current, the band structure, and interactions with other particles. Any change to the electron's behavior in that case will also change its path through a material. On a large scale, the behavior of electrons will be altered, and any resultant change in transport properties is known

[4]This may the best place to mention that throughout this thesis, the symbol $\mathbf{B}$ will be used for "magnetic field" and the units will be in T. Some authors prefer to use $\mathbf{H}$ (officially "magnetic field strength".) and Oe, with $\mathbf{B}$ designated the "magnetic flux density". The distinction between the two is that $\mathbf{H}$ is the applied external field, while $\mathbf{B}$ is the measured field at a point in space, which may differ from $\mathbf{H}$ due to the magnetization $\mathbf{M}$ of the medium at that location. In reality, the difference is often ignored and generally it is assumed $\mathbf{B} = \mu_0\mathbf{H}$. For example, the magnetic field when taking data at the NHMFL is listed in T, while the instruments at UMD have it in Oe ($\mu_0 \ \times \ 10^5$ Oe = 1 T). A similar argument for this convention is found in Ref. [52].

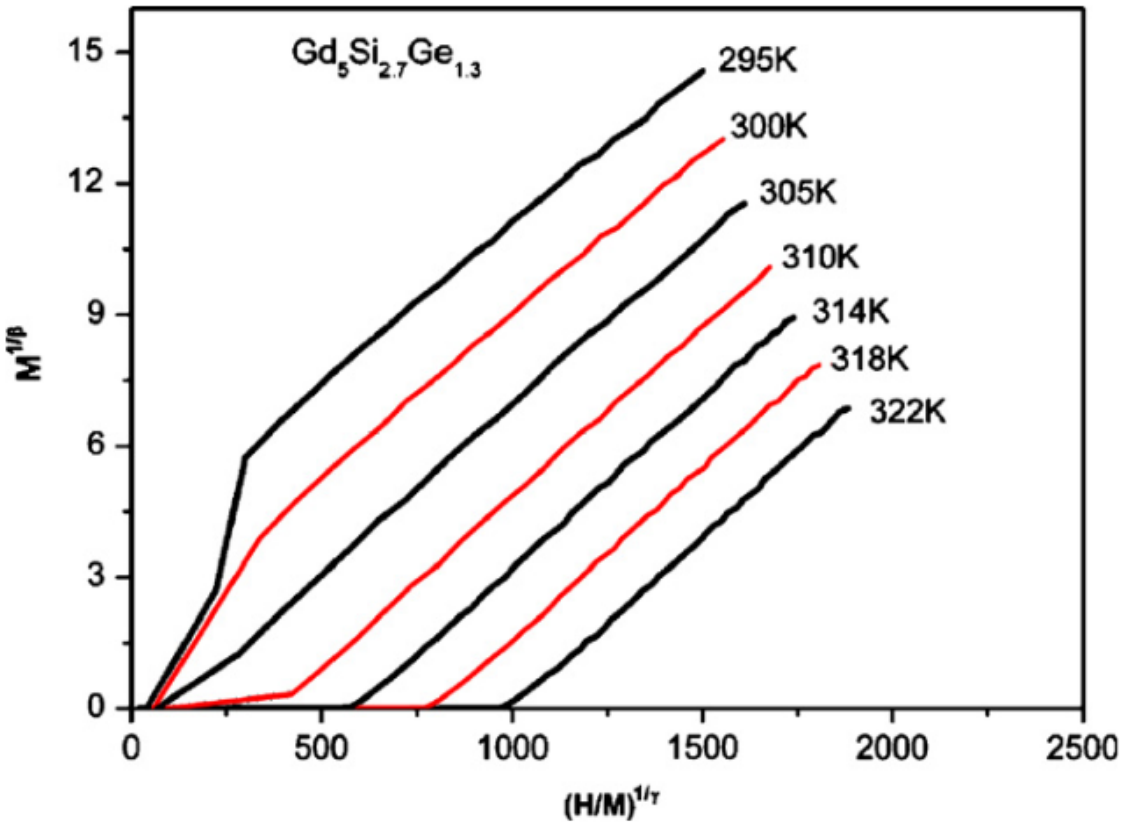

Figure 2.3: An example of the use of an Arrott plot to find a paramagnetic-ferromagnetic transition temperature of $Gd_5Si_{2.7}Ge_{1.3}$. Curves below 305 K have a positive y-intercept when extrapolating from high H/M, indicating remnant zero-field magnetization and thus ferromagnetism. Axes were rescaled by powers of the critical exponents γ and β to obtain linear behavior and make the extrapolation easier. Taken from Ref. [51].

as magnetoresistance (MR). It was found in the 19th Century that the resistance of metals such as copper or iron would change in field. However, the effect is weak in most typical metals, especially in small fields and at room temperature. On the other hand, in other materials and at lower temperatures resistance can be many orders of magnitude larger or smaller in the absence of field.

There is a basic, relatively straightforward expectation for what should happen to a metal's resistance in a magnetic field. Any deviations are that are of interest in what they can elucidate about a material's properties. In some cases, this is because the material itself has an inherent feature that magnetic fields help to reveal. In others, such as those exhibiting quantum oscillations, applied fields change the arrangement of electrons in a system in a way that can only be explained with quantum mechanics. Naturally, stronger magnetic fields amplify these effects, hence the reason that many experiments to be covered were performed at the National High Magnetic Field Laboratory. The phenomena to be explored could increase linearly, quadratically, or even exponentially with increasing field.

2.2.1 The Basics

To get to the simplest approximation of magnetoresistance, one can start with the foundational approximation of transport in a solid: the Drude model. In this picture, electrons in a material move with some drift velocity $\mathbf{v}$ and scatter randomly, on average, once in a time interval τ called the "relaxation time". If an electric field is applied, then consideration of 2.2 shows that they will build up a momentum

m$\mathbf{v} = q\mathbf{E}\tau$. The current density $\mathbf{J} = qn\mathbf{v}$ can then be reexpressed as $\mathbf{J} = \frac{nq^2\tau}{m}\ \mathbf{E}$. It is also known from Ohm's law that $\mathbf{J} = \sigma\mathbf{E}$, where σ is the conductivity. The Drude conductivity is then

$$\sigma_0 \ = \ \frac{nq^2\tau}{m} \tag{2.3}$$

with the "0" subscript denoting the zero field value[5]. The resistivity $\rho = \sigma^{-1}$.

From here, the next step is to see the effect of an applied magnetic on the resistance in the current direction (the longitudinal resistance). It will turn out that in such a model the prediction is that the resistance in the direction of applied current should be independent of magnetic field, but the derivation is still informative. Consider an electron with charge -e moving through a material with $\mathbf{E}$ and $\mathbf{B}$ applied. Due to interactions, it has an effective mass m^* that is not necessarily the electron rest mass m_e. Taking Drude physics into account, now the motion can be described by

$$m^*\Big(\frac{\mathrm{d}\mathbf{v}}{\mathrm{dt}} + \frac{\mathbf{v}}{t}\Big) = -e\Big(\mathbf{E} + \mathbf{v}\ \times\ \mathbf{B}\Big) \tag{2.4}$$

Due to the presence of a cross product, electron motion along the direction of applied field will be unaffected by $\mathbf{B}$[6]. The issue is now to determine the current

[5]Similarly, ρ_0 in this section refers to the resistivity when B = 0 T.

[6]When field and current are parallel, there should be no magnetoresistance since $\mathbf{v}$ and $\mathbf{B}$ are parallel, and in practice MR with parallel field and current is small for most samples (including those to be covered here), to the point when it could be attributed to slight misalignment of the sample, electrical contacts, and/or field. Current jetting or the chiral anomaly in topological semimetals can result in nonzero longitudinal magnetoresistance. For data shown throughout this work, field was perpendicular to current.

density **J** in the plane normal to the field. Taking $\mathbf{B} = \mathrm{B}\hat{z}$ and $\mathbf{E} = \mathrm{E}\hat{x}$, the task is to solve for $\mathbf{J} \cdot \hat{x}$ and $\mathbf{J} \cdot \hat{y}$ in steady state ($\frac{\mathrm{d}\mathbf{v}}{\mathrm{dt}} = 0$). Two separate equations emerge from this:

$$v_x = -\frac{e\tau}{m^*}(E_x + v_y B) \tag{2.5}$$

$$v_y = \frac{e\tau}{m^*} v_x B \tag{2.6}$$

J must satisfy two separate relations: $\mathbf{J} = \text{-}ne\mathbf{v}$ and $\mathbf{J} = \sigma_{ij}\mathbf{E}$. At this point it is important to emphasize that the conductivity σ_{ij} is a tensor, describing direction of the current, j, produced by an electric field in the i direction. This was skipped over in the Drude approximation since **J** and **E** were always parallel, but in this example there will be two components, σ_{xx} and σ_{xy}, are relevant. Making the appropriate substitutions and rearrangements (solving first for v_x, then v_y) leads to two somewhat unwieldy equations

$$J_x = \frac{\frac{ne^2\tau}{m^*}}{1 + \left(\frac{e\tau}{m^*}B\right)^2} E_x \tag{2.7}$$

$$J_y = -\frac{ne^2\tau}{m^*} \frac{\frac{ne\tau}{m^*}}{1 + \left(\frac{e\tau}{m^*}B\right)^2} E_x \tag{2.8}$$

It has already been seen that $ne^2\tau/m^* = \sigma_0$. The quantity eB/m^* has units of inverse time and will be called the cyclotron frequency, ω_c, and is the angular speed of the circular orbit the electron makes perpendicular to the field. The conductivities

are the prefactors on the right hand side of the above equations and become

$$\sigma_{xx} = \frac{\sigma_0}{1 + (\omega_c \tau)^2} \tag{2.9}$$

$$\sigma_{xy} = \frac{\sigma_0 \omega_c \tau}{1 + (\omega_c \tau)^2} \tag{2.10}$$

The magnetic field in $\hat{z}$ has led to a change in the conductivity in $\hat{x}$ and $\hat{y}$. This derivation can be repeated with $\mathbf{E} = \mathrm{E}\hat{y}$ to get the full in-plane conductivity tensor

$$\boldsymbol{\sigma} = \begin{pmatrix} \sigma_{xx} & -\sigma_{xy} \\ \sigma_{xy} & \sigma_{xx} \end{pmatrix} = \frac{\sigma_0}{1 + (\omega_c \tau)^2} \begin{pmatrix} 1 & \omega_c \tau \\ -\omega_c \tau & 1 \end{pmatrix} \tag{2.11}$$

But the interest here is in the change in ρ. In the Drude model $\rho_0 = \sigma_0^{-1}$, but because here $\boldsymbol{\sigma}$ has become a 2×2 tensor, $\rho_{xx} \neq 1/\sigma_{xx}$ (and the same is true of other components). After matrix inversion, the resistivity tensor becomes

$$\boldsymbol{\rho} = \frac{1}{\sigma_0} \begin{pmatrix} 1 & -\omega_c \tau \\ \omega_c \tau & 1 \end{pmatrix} \tag{2.12}$$

and so $\rho_{xx} = \rho_0$, and $\rho_{xy} = -\rho_0 \omega_c \tau = -\frac{B}{ne}$. ρ_{xy} is called the Hall resistivity and will be covered later. More important for now is that ρ_{xx} is unchanged. In other words, there is no magnetoresistivity, despite the change in conductivity in field.

The reason for the lack of change is that this initial derivation was too simplistic. A more realistic picture explains the origin of magnetoresistance by doing

away with the assumption that all carriers have the same n, τ, and m^*. In a real metal, multiple bands can contribute to transport, and each can be described independently with their own $\sigma_{xx,i}$ and $\sigma_{xy,i}$. The total $\mathbf{J}$ will be the sum of each $\mathbf{J}_i$. Unless each individual current density coincidentally points in the same direction, $\mid \mathbf{J}_{total} \mid \quad \leq \quad \mid \Sigma \, \mathbf{J}_i \mid$. The current density has to go down, so by Ohm's law the resistivity must go up.

It is useful to illustrate this with a slightly more complex example than the first, with a single hole and electron band involved in transport. It is also simpler to write the conductivity as comprising an in phase (magnetoresistive) and out of phase (Hall) component [52]:

$$\sigma_{total} = \frac{\sigma_{0,e}}{1 - i\omega_c\tau} + \frac{\sigma_{0,h}}{1 + i\omega_c\tau} \tag{2.13}$$

Where $\sigma_{0,i}$ is the zero field Drude conductivity for each band, the electron band denoted by the "e" subscript and the hole band by "h". The difference in sign of the imaginary component of the denominators is due to the difference in carrier sign. Substituting 2.3 for each band gives

$$\sigma_{total} = e\Big[\frac{n_e\mu_e}{1 - i\mu_e B} + \frac{n_h\mu_h}{1 + i\mu_h B}\Big] \tag{2.14}$$

where $\mu_i = \frac{\sigma_{0,i}}{n_i e}$ is the mobility of the electron or hole band (which to first approximation is field independent). The longitudinal resistivity ρ_{xx} is the inverse of the real part of this equation. Skipping to the desired result the formula for the longitudinal magnetoresistance with one hole and one electron band is [53]

$$\rho_{xx} = \frac{1}{e}\frac{(n_h\mu_h + n_e\mu_e) + (n_h\mu_e + n_e\mu_h)\mu_h\mu_e B^2}{(n_h\mu_h + n_e\mu_e)^2 + (n_h - n_e)^2(\mu_h\mu_e B)^2} \tag{2.15}$$

There is now a clear field dependence of the longitudinal resistance. But note that in the case of only one carrier type ($\mu = 0$ for the electrons or holes) resistivity will be independent of field again. It is insightful to look at other limiting cases. In low field, as long as the carrier concentrations of the two bands are at all comparable, the second term in the numerator will be larger than the second term in the denominator, and a B^2 dependence results. At high field the second terms in both the numerator and denominator are large and the field dependence cancels out. Generically, then, the magnetoresistance of a metal should have an initial quadratic field dependence, and then saturate. While it might seem simple, this is actually a good description of the MR in a number of real materials [52].

2.2.2 Large Magnetoresistance

The MR of a metal is often small, especially above cryogenic temperatures. An empirical way of judging if a significant MR effect should be seen is by calculating $\omega_c\tau$. This quantity describes how much of its cyclotron orbit a carrier completes before being scattered. As a rule of thumb, a value greater than one is generally required for significant MR. The term can be rewritten as $\omega_c\tau = \frac{B\sigma_0}{ne}$, a definition from which it is clear that not just high field, but good conductivity (low resistivity) and low carrier concentration can also make MR more noticeable. The last of these is why many semimetals or semiconductors have a large MR, in addition to the

electron-hole compensation effect to be discussed shortly. Many metals, such as copper, also show negligible MR at room temperature but a much larger increase of resistivity in field at low temperatures when their conductivity is much higher.

There are more exotic sources of large MR, and such a property can be useful for applications. The 2007 Nobel Prize in Physics was awarded for the discovery of giant magnetoresistance in ferromagnetic-nonmagnetic layered materials [54]. In those materials, the orientation of the spins in ferromagnetic layers can be controlled by an external field. Parallel alignment of adjacent layers will have a much lower resistance than an antiparallel configuration, and so it a significant change in resistance will be seen when spins are flipped. Giant MR materials have found application as magnetic field sensors in hard disk drives and magnetic random access memory, among other areas. A variety of other mechanisms can cause an increase in MR and go by different names, though there is some inconsistency in which terms refer to specific physical phenomena, and which are more a general comment on MR size. Beyond "giant" [54], there are also "colossal" [55], "extreme" [56], "extraordinary" [57], "titanic" [58], and "huge" [59] magnetoresistive effects. This thesis will use the word "large" to refer to the MR of FeP and CoP, as it is generic enough to not imply a specific mechanism at the outset.

Equation (2.15) was examined in limiting cases of magnetic field in the previous section, but what was not explored was its dependence on the relative carrier concentrations. Looking again, it is clear that a small $n_h - n_e$ will result in a large MR in high field when the B^2-dependent terms dominate. This state of nearly equal numbers of electron and hole carriers is referred to as "compensation", and occurs

frequently in semimetals, which are prone to combining multiband conduction from pockets with low carrier concentrations. In the earliest days this was seen in the pnictogens (As, Sb, and Bi) [52]. More recently it has emerged in the study of topological semimetals such as WTe_2 [53] and metal-pnictogen compounds (forming in other structures than B31) like NbP, LaSb, and $TaAs_2$ [56, 60, 61].

But while it has recently been seen in many topological semimetals, compensation-driven large MR is not on its own exotic, as it has been seen to come neatly out of a limiting case of the the two-band model and the increase of MR for materials with a lower carrier concentration. In a way, the reliability of the model in an extreme limit is remarkable, and shows that it is actually a useful description, rather than too basic of an approximation. The reason it appears in topological semimetals is because, as semimetals, they are likely to have very similar, and small, electron and hole densities. Other probes of transport in field, such as Hall effect measurements and examination of the field dependence of large MR, can help verify potential topological properties [62], to see nothing of direct imaging of band structure as is possible with angle-resolved photoemission spectroscopy.

At the end of the previous section it was stated that in the two band model, MR should saturate at high fields. This is common, but there it is also common for MR not to saturate, or to only do so at certain angles. This is true in the case even of seemingly simple conductors like Sn or Pb, as shown in Fig. 2.4, which features data from Ref. [63]. At two angles 30° apart, the magnetoresistance differs by an order of magnitude or two, and the higher magnetoresistance orientation does not saturate. This difference comes from whether carriers make open or closed cyclotron

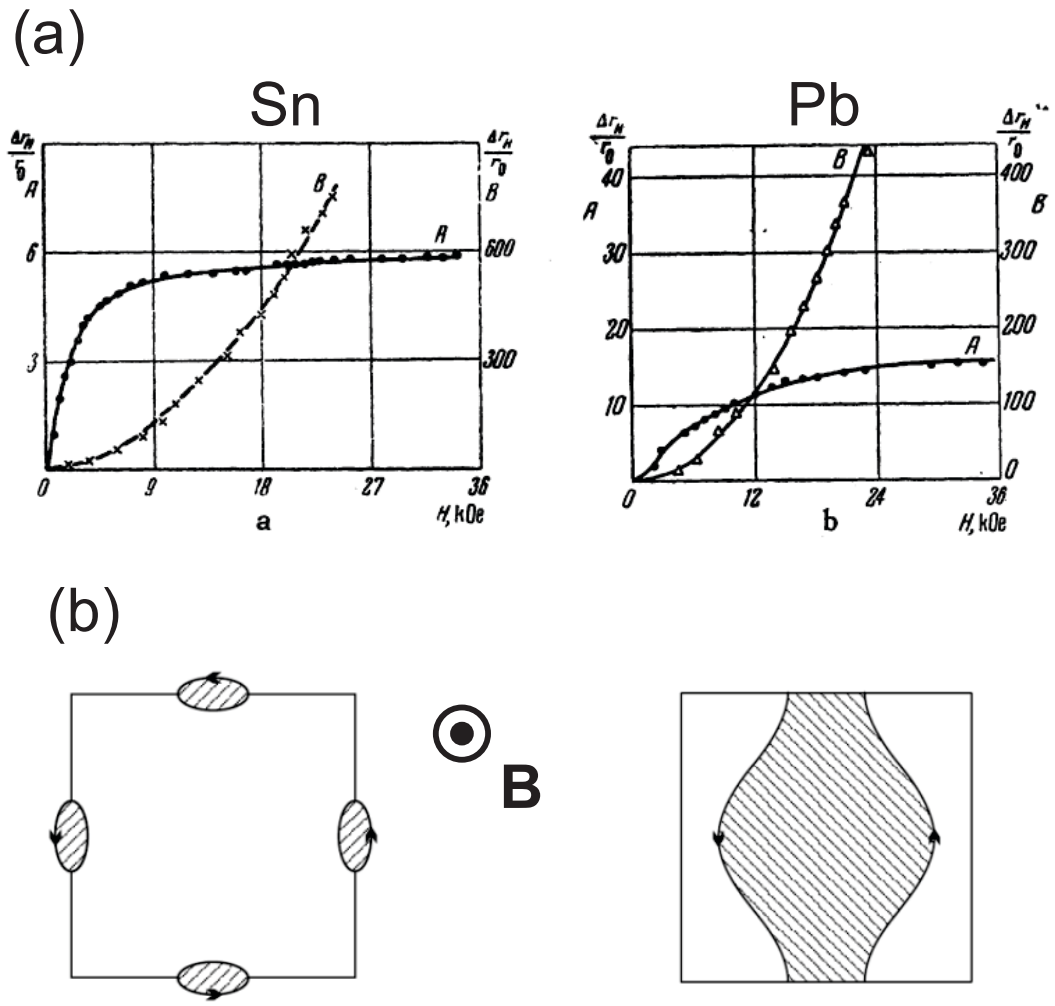

Figure 2.4: (a) The magnetoresistance of (left) Sn and (right) Pb at two different angles corresponding to the maximum and minimum of high field magnetoresistance. In each plot the left vertical axis corresponds to orientation "A" and the right one to "B", and the MR differs by orders of magnitude with orientation. This is because the MR saturates for closed Fermi surface orbits, but does not for open ones. (b) (left) Closed and (right) open electron orbits around the Fermi surface for a magnetic field out of the plane. The closed orbit results in the electron retracing the same path, while in the open orbit the velocity never makes a full loop. (a) is from Ref. [63], (b) from Ref. [64].

orbits perpendicular to the magnetic field [52].

A (moderately) more precise definition of "high field" is the condition that $\omega_c\tau >> 1$. It is at this point that the scattering time is much longer than timescale set by field-induced motion. As a result, magnetoresistive effectives are determined more by Fermi surface structure than by scattering. It was noted at the outset that an electron in a magnetic field traverses a closed circuit perpendicular to that field in both real and momentum space. As B increases, the real space radius of the cyclotron orbit will correspondingly get smaller. If the field is strong enough, then electron motion will be almost entirely circular, and will not move along the direction of the applied electric field **E** unless it scatters off of an impurity. A strong enough field results in an orbit radius shorter than the mean distance between impurities quantified by τ. At that point, higher fields (and smaller orbital radii) have a negligible effect on scattering, since the electron can complete its orbit without running into a scattering center that could redirect it along the low-high voltage path. The resistance will be independent of field above this threshold, and the resistance will be higher than at zero field but saturate; this was already shown mathematically with the two band model 2.15.

That is the cased for a closed orbit, where the electron's velocity, like its position, can fully rotate and come back to the same direction [Fig. 2.4(a)]. However, the magnetoresistance will not saturate for an open orbit [Fig. 2.4(b)]. As an electron moves in real space, it must also obey the trajectories allowed by the band structure in reciprocal space at the Fermi energy. If the 2D Fermi surface projection does

not form a closed loop, the electron will move without interruption in the same direction. Its velocity will then remain pointed in mostly the same direction and increase with field. Thus MR will not saturate but rather will remain quadratic in the high field limit. Because of this, the field dependence at different angles gives information about the shape of Fermi surface, and whether it is open or closed in the plane perpendicular to the applied field. Even in cases when the field dependence does saturate, the threshold field is related to $\omega_c\tau$ and thus the effective mass or scattering time in the corresponding plane. Angular dependence of MR can give useful information about the Fermi surface, as exemplified by Fig. 2.4.

2.2.3 Linear Magnetoresistance

Equation 2.15 gives a good idea of field dependence of the resistance in many metals, but significant deviations from these expectations indicate unusual scattering processes. Of particular interest has been the observation of linear magnetoresistance (LMR). Nonsaturating linear MR is especially sought after for its possible use in magnetic sensors [65], for which a simple field dependence is optimal. The appearance of this phenomenon in heavily-investigated materials such as graphene [66], topological insulators, the topological semimetals, and, originally, simple elemental metals like Na, Al, and K [67–69] has led to it being the subject of much theoretical consideration.

One difficulty with LMR is that, like large MR, there are a variety of potential mechanisms of both classical and quantum origin [70]. Even simple disorder is one

known cause of linear MR in single crystals and polycrstals. Inhomogeneities or disorder cause fluctuations in carrier mobility and density that can redirect the current through a section of the sample [71, 72]. This can be explained by considering the interplay between disorder and "guiding-center motion" [73]. In this scenario, carriers are described as having an overall average a drift velocity, while at the same time making orbits in the plane perpendicular to the field, analogous to cycloid motion. A disorder potential with a correlation length much larger than the cyclotron radius will confine carrier motion to the plane normal to the field. This leads to LMR, as the effect on the conductivity is similar to the Hall effect, which is linear in field. This is the reason large, linear MR can emerge in graphene when the sample size exceeds the domain size [66], and in 3D materials like Cd_3As_2 [74].

Another potential driver of LMR is proximity to a quantum critical point. Typically, a phase transition is dominated by thermal fluctuations around the transition temperature. However, when the transition is suppressed to 0 K by some other parameter (magnetic field, chemical doping, applied pressure), there are no thermal fluctuations and instead quantum fluctuations dominate [75]. As a result there is no internal energy scale for the material to reference, and the correlation length and time of the order parameter both diverge. Thus observable quantities should be scale-invariant, and this can result in a linear dependence of the resistivity on both temperature and field, an effect that has been seen in the iron pnictides [76] and cuprates [77]. This is in fact one motivation behind high magnetic field research, as in both cases MR could be astonishingly linear up to 100 T, a strong indicator of QC physics. The observation of quasilinear MR in CrAs near an AFM-SC crossover

has been seen as hinting at a potential QCP for this very reason [19].

Fermi surfaces under specific conditions can give rise to LMR as well. If the conduction is dominated by a pocket with a linear dispersion, the resulting field dependence can also be linear [78]. This is because the effective mass for a linear dispersion is zero, resulting in a very large $\omega_c\tau$. This theory has often be used to explain the observation of large, nonsaturating LMR in topological semimetals, which have small pockets with a linear (termed "Dirac" or "Weyl") dispersion. But this effect is not confined only to materials with a single pocket, and applies equally well to Fermi surfaces that have other larger pockets that follow the semiclassical description above. As long as the smaller pocket dominates conduction, and field is high enough, linear MR is achievable. The requirement on magnetic field involves a discussion of Landau level quantization that moves the description from semiclassical to quantum. For that reason it will be saved for Ch. 5 on FeP, which shows angle-dependent linear MR, since a full discussion of Landau level quantization will not be discussed until covering quantum oscillations.

2.2.4 The Hall Effect

The Hall effect was briefly touched on in the first derivation of magnetoresistance, where it was noted that in the most basic consideration of MR a voltage perpendicular to both field and current will arise[7]. The corresponding Hall resistivity $\rho_{xy} = -\frac{B}{ne}$ for electron carriers, with an opposite sign for hole carriers. The

[7]This is known as the "Hall voltage" after its discoverer, and all quantities associated with the transverse voltage arising from a magnetic field are generally called "Hall (term)".

process to arrive at that result can be restated in a way that focuses on the Hall effect and perhaps makes it more intuitive.

In a magnetic field, carriers that normally move linearly between the two current leads will be deflected by the Lorentz force 2.2. Again it is simplest to define $\hat{x}$ as the current direction, $\hat{y}$ as the direction between the two voltage leads, and $\hat{z}$ as the direction of applied field. In steady state, $\mathbf{F} = 0$. Breaking the force equation into perpendicular components and noting that in general $E_{ij} = V_{ij}/x_{ij}$, in the $\hat{y}$ direction $0 = \frac{V_y}{w} - v_x B_z$, or $V_y = \frac{v_x B_z}{w}$, where w is the sample width. From the Drude model $I_x = q \cdot ntw \cdot v_x$, with t the sample thickness. Substituting for v_x and dividing the voltage by the current gives a resistance equal to $\frac{1}{qnt}B$. So, in a single band model the transverse (Hall) voltage has a linear dependence on magnetic field, with a positive or negative slope depending on if the carriers are holes ($q = e$) or electrons ($q = -e$). Defining a "Hall coefficient" $R_H = -\frac{1}{ne}$ results in the equation $\rho_{xy} = R_H B$, where $\rho_{xy} = R_{xy} t$ is the Hall resistivity. Note that, somewhat confusingly, despite the employed symbol the Hall coefficient is not a resistance. Because multiple bands often participate in conduction, R_H can be a more useful quantity than n (which implicity assumes a single band), and here will be given in units of cm^3/C. In the case of a simple, single band material, measurements of the Hall coefficient provide immediate information about the sign and density of the carrier, because electrons and holes are deflected in the same direction by a magnetic field since both their velocities and charges have opposite signs. The sign of the transverse voltage difference will then also depend on the carrier sign.

Of course, as with magnetoresistance, materials rarely behave at the limit of

simplicity, and frequently have multiple carriers of various types and concentrations. The same two band model used for MR (2.14) can also be applied to the Hall effect. The only change is the reciprocal of the imaginary part of (2.14), rather than the real part, is used [52, 79]:

$$\rho_{xy} = \frac{B}{e} \frac{(n_h \mu_h^2 - n_e \mu_e^2) + (n_h - n_e)(\mu_h \mu_e B)^2}{(n_h \mu_h + n_e \mu_e)^2 + (n_h - n_e)^2 (\mu_h \mu_e B)^2} \tag{2.16}$$

Again it is instructive to look at extreme cases. When one type of carrier dominates, the mobility of the less dominant carrier is effectively zero. The second terms in the numerator and denominator can be neglected and ρ_{xy} retains its simple linear field dependence. But when carrier concentrations are comparable, $n_h - n_e$ is very small, and the second term in the denominator cannot be neglected. Therefore the Hall resistance will have a significant field dependence, and can even change sign with field [79]. In a middling case, a higher field will lead to a gradually less linear dependence. Fitting a nonlinear Hall resistance and an abnormal MR can give information about the concentrations and mobilities of electron and hole carriers. There are four variables (the two μ and n values) to solve for with just two equations, but usually reasonable assumptions can be made to get qualitatively informative answers.

2.3 Quantum Oscillations

Magnetoresistance can shed light on the interactions experienced by carriers as they move through a solid. But it is also possible for a magnetic field to lead to a new

ordered phenomenon of these carriers. A notable example of this is the oscillatory behavior that arises in a variety of quantities and found to be periodic in inverse field. These "quantum oscillations" have been observed since the 1930s, initially in semiconductors thanks to their large, compensated MR [80]. Subsequent theoretical explanation showed how oscillations could be analyzed to give information about the Fermi surface geometry, carrier concentration, effective mass, and other quantities, in a subfield referred to as "Fermiology".

2.3.1 Origin

The Hamiltonian of a plane wave traveling through a solid is

$$E\psi = \left[\frac{\hat{p}_x^2}{(2m_1^*)^{\frac{1}{2}}}\ \hat{x} + \frac{\hat{p}_y^2}{(2m_2^*)^{\frac{1}{2}}}\ \hat{y} + \frac{\hat{p}_z^2}{(2m_3^*)^{\frac{1}{2}}}\ \hat{z}\right]^2 \psi \tag{2.17}$$

where E is the energy, ψ the electron wave function, $\hat{p}_i$ the momentum operator in each direction, and m_i the effective masses in each direction. To deal with a magnetic field $\mathbf{B} = B\hat{z}$ requires introducing a magnetic vector potential $\mathbf{A}$ for which $\mathbf{B} = \nabla \times \mathbf{A}$. This gives some freedom in defining $\mathbf{A}$, and a convenient choice is $\mathbf{A} = (0, Bx, 0)$, called "Landau gauge". The momentum operator p then becomes $p + e\mathbf{A}$. As long as the conjugate position operator does not appear in 2.17, the momentum operator p_i can be rewritten as $\hbar k_i$. Additionally, there are no cross terms when squaring each term in the brackets. Making all of these changes, (2.17) becomes

$$E\psi = \Big[\frac{p_x^2}{2m_1^*} + \frac{(\hbar k_y + eBx)^2}{2m_2^*} + \frac{\hbar^2 k_z^2}{2m_3^*}\Big]\psi \tag{2.18}$$

Introducing a constant energy shift $E' = E - (\hbar^2 k_z^2/2m_3)$ and redefining $x_0 = -(\hbar k_y/eB)$ simplifies the equation to

$$E'\psi = \Big[\frac{p_x^2}{2m_1^*} + \frac{(eB)^2}{2m_2^*}(x - x_0)^2\Big]\psi \tag{2.19}$$

which has the same form as the one-dimensional harmonic oscillator with frequency $\omega = eB/(m_1 m_2)^{\frac{1}{2}}$ and energies $E' = (l + \frac{1}{2})\hbar\omega$. This results in a total energy $E = \frac{(\hbar k)^2}{2m_3} + (l + \frac{1}{2})\hbar\omega$. It can be shown with more effort that ω for this geometry is the same is the same as the cyclotron frequency $\omega_c = \frac{eB}{m^*}$.

The implication of this result is that the energy of electron motion in the plane perpendicular to the field is quantized, just like the energy levels of the quantum harmonic oscillator. In this case they are known as "Landau Levels" (LLs). The in-plane momentum-space areas of these orbits are similarly quantized. One way of picturing them is as tubes that extend infinitely in the k_z direction but with cross sections whose radii are determined by the Fermi surface shape and strength of the magnetic field. The cross sections will expand with field but be cut off when the intersect with the edge of Fermi surface, since carriers cannot have energies greater than the Fermi energy. Figure 2.5, from Ref. [81], illustrates this in the case of a circular Fermi surface, but it also applies to more complex geometries. The separation in energy between two LLs is $\Delta E = \hbar\omega = \frac{\hbar eB}{m^*}$. The effective mass can be replaced with its original definition in the context of band structure

$m^* = \frac{\hbar^2}{2\pi}\frac{\partial A}{\partial E}$. If the separation of the energies is much smaller than the energies themselves (which, since the latter are on the order of E_F, is almost always true) then $\frac{\partial A}{\partial E} \approx \frac{\Delta A}{\Delta E}$. Substituting in for ΔE and rearranging terms gives the separation in k-space between two Landau tubes:

$$\Delta A = \frac{2\pi e B}{\hbar} \tag{2.20}$$

As noted, the area of these tubes in the plane perpendicular to the field is determined by the field strength; increasing field increases the area. The interesting part comes when the area surpasses the largest cross sectional area of a Fermi pocket, A_{ext}. In Fig. 2.5, that is when the radius of the tube becomes equal to the radius of the circle. At that point the density of states of this band must go to zero, as the carrier energy cannot exceed E_F (ignoring for now the slight softening of this limit from the Fermi-Dirac distribution). Thus a LL will be depleted every time the field changes by $B_F = \frac{\hbar}{2\pi e}A_{ext}$. B_F is the frequency of quantum oscillations, which will evidently be periodic in $1/B$.

The reason this behavior is oscillatory is the depletion of carriers from a LL in increasing field as it passes through the Fermi level. LLs are theoretically infinitely narrow, but in practice broadened by temperature, impurities, etc. With increasing field, the DOS increases as the band edge, peaks as it passes through E_F, then decreases and goes to zero as the second half of the band passes through, before increasing again after a period $1/B_F$ when it hits the edge of the next LL. The density of states at E_F, $g(E_F)$ will then show oscillatory behavior periodic in inverse

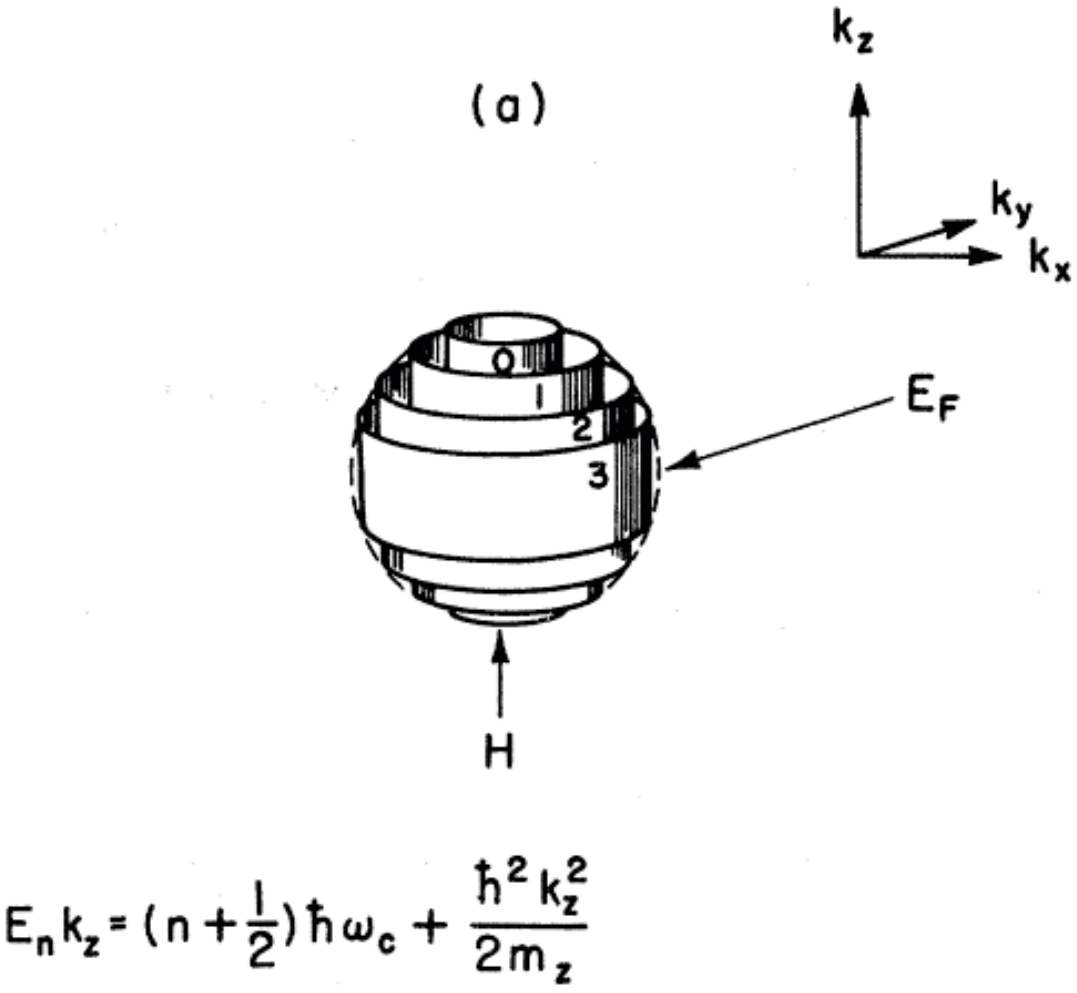

Figure 2.5: The quantization of energy levels into "Landau tubes" with different n values by a magnetic field along the z-axis. The size (and thus both in-plane area and quantum oscillation frequency) are bounded by where they touch the spherical Fermi surface. Taken from Ref. [81]

field. A final thing to note is that QOs imply a closed Fermi surface at a particular orientation; if it were open, then there could not be a cyclotron frequency as the electron would never complete a circuit.

2.3.2 Detection and Analysis

QOs come from a change in the density of states at the Fermi level, so they can be detected in any physical property that depends on $g(\mathrm{E}_F)$. The two most commonly presented, and not coincidentally probably the two most straightforward to measure, are oscillations in electrical resistance and magnetic susceptibility. In this case they are referred to as Shubnikov-de Haas (SdH) or de Haas-van Alphen (dHvA) oscillations, respectively. However, oscillations can also be seen in thermal conductivity, sound velocity, and even in sample length. This thesis will only examine SdH and dHvA oscillations. In fact, it will focus primarily on oscillations of the magnetic torque. The reason for this is again simply one of practicality: the cantilevers used for torque measurements are in general more sensitive than the equivalent resistance measurement, and have a simpler background to subtract.

2.3.3 Utility

The general procedure to extract quantum oscillation frequencies from magnetic torque was this: a polynomial (typically a third order one was sufficient) was subtracted from the raw signal. The difference between the two is ideally a purely oscillatory component centered around zero. Those data were interpolated so as to

be evenly spaced in inverse field. A fast Fourier transform (FFT) was then performed on them to find the oscillation amplitude of different frequencies. When comparing amplitudes for data at different angles or temperatures, the same field range was used for fitting and interpolating (with the same number of points), since changing either would affect the resulting amplitude. In some cases in other work, the original signal itself has been fit globally through a general description of the oscillation amplitude called the Lifshitz-Kosevich (LK) formula. Analysis of the angular, temperature, and field dependence of oscillations can give an abundance of information about a material.

As noted, the QO frequency (in units of magnetic field) is set by the extremal area of an orbit around a Fermi surface pocket. As a result, it can be directly equated to a cross sectional k-space pocket size. Many materials will show multiple oscillation frequencies. This can result from either different extremal paths around the same pocket, or from multiple pockets located at different points of the Brillouin zone. A simple way of picturing the former is to imagine a cylinder with its axis along $\hat{z}$ and a radius that changes with height. If field is applied along the cylinder axis, carriers will have different $x-y$ plane path lengths depending on their location. These can be referred to as "neck" and "belly" orbits and this line of thinking can readily be extended to more complex shapes.

By changing the angle at which field is applied to the sample, one can then map out the extremal area of a pocket and partially reconstruct the full shape. These can be compared to calculations from density functional theory (DFT) using the Supercell k-Space Extremal Area Finder (SKEAF) program [82]. But even without

theoretical calculations, a general idea of the Fermiology can often be obtained. If a Fermi surface pocket is circular, the frequency will not change with angle. In contrast, a cylindrical pocket will have a frequency that goes as $1/\cos\,\theta$, where θ is the angle between the applied field and the z-axis of the cylinder. Often, seeing that a pocket's angular dependence approximates this, and thus is relatively two dimensional, can be useful information. Note that in this case the frequency will diverge when field is applied perpendicular to the cylinder axis and cyclotron orbit is open, the same condition leading to nonsaturating magnetoresistance. Having a circular pocket (or something close to it) also makes it possible to estimate the carrier concentration of that pocket. If k_F is constant in all directions then $A_{ext} = \pi k_F^2$ and the carrier concentration $n = \left(\frac{k_F}{3\pi^2}\right)^{\frac{3}{2}}$. Substituting these into into the equation for the oscillation frequency gives

$$n = \frac{1}{3\pi^2}\left(\frac{2eF}{\hbar}\right)^{\frac{3}{2}} \tag{2.21}$$

The oscillation amplitude will decrease with increasing temperature, as the Fermi-Dirac distribution blurs the E_F cutoff and the LLs broaden. Very roughly, oscillations will be visible when $\hbar\omega_c > k_B T$. Tracking the decrease in amplitude with temperature gives an estimate of effective mass through one of the terms in the LK formula, here to be called the LK factor

$$R_T = \frac{\alpha m^* T/(Bm_e)}{\sinh(\alpha m^* T/(Bm_e))} \tag{2.22}$$

where m_e is the electron rest mass and $\alpha = 2\pi^2 c k_B/e\hbar \approx 14.69$ T/K with

c the speed of light and k_B the Boltzmann constant [80]. This effective mass is an average of the effective mass for every direction in the orbital plane. Larger masses will decay more quickly with temperature, while smaller ones survive to high temperatures, in the most extreme cases to perhaps 100 K or more, but for the materials here about 10-20 K. With the effective masses it is possible to calculate the Sommerfeld coefficient γ, which can also be obtained from heat capacity measurements. In the case of multiple frequencies, their contributions can be added linearly. Comparison of γ values obtained through QOs and measurements of specific heat can give insight into whether all carriers have been observed in QOs analysis.

The LK formula also includes what is called the Dingle factor,

$$R_D = \exp[-\alpha m^* T_D/(Bm_e)] \tag{2.23}$$

where T_D is the Dingle temperature [80]. This accounts for the increase in oscillation amplitude with field, which is exponential in 1/B. This is why high magnetic fields can be so useful in observing QOs. T_D is proportional to the scattering rate Γ as

$$T_D = \frac{\hbar}{2\pi k_B}\Gamma \tag{2.24}$$

Γ is also the inverse of the scattering time τ. From this quantities it is then possible to extract the mean free path

$$\ell = \frac{\hbar k_F}{m^*}\frac{1}{\Gamma} \tag{2.25}$$

by assuming the cross section is circular. If that assumption does not hold, then similar to m^* this only approximates the average ℓ throughout the plane. In this work, the location of peaks of the "decaying envelope" of oscillatory behavior were used to determine T_D. This can only be done if m^* is known. It also requires that a single frequency dominates the spectrum, as otherwise the combination of T_D complicates the exponential decay.

There is more knowledge to be gained from QOs. For example, the number of harmonics of a fundamental frequency give an idea of sample quality, as they are in essence the number of times a carrier can orbit a pocket before being scattered. Frequencies that are the sums or differences of fundamentals also paint a more intricate picture of the Fermi surface, where carriers may be able to move between parts of the Fermi surface and trace out partial orbits of multiple pockets. Frequencies substantially larger than the first Brillouin zone can indicate "magnetic breakdown", where the energy introduced by the field is so large that carriers are able to jump into the next BZ. Splitting of oscillation frequencies can also be used to obtain the g-factor of each pocket. However, the concepts covered in the previous few paragraphs are enough to understand the QO analysis that will be presented in Chs. 4, 6, and 7. Landau quantization is a powerful phenomenon, and the resulting Fermiology can give deep insight into the electronic structure of metals.

Chapter 3: Experimental Methods

There are many steps to get to the point of obtaining useful data when studying a material. First of all, the compound of interest needs to be produced, hopefully reproducibly and with high quality. Next, the proper experimental technique must be found, and the sample prepared appropriately. Finally, the collected data need to be analyzed, so that a logical (and, ideally, correct) conclusion can be reached. This section will cover sample growth and measurement techniques.

3.1 Single Crystal Growth

The first step to measuring a material is to make it. This does not simply mean getting the correct composition and lattice structure, but also getting the sample in an appropriate shape to facilitate measurements. Typically, when doing a basic characterization of a material's properties, the ideal is a single crystal. Single crystals maintain a single crystallographic alignment over their entire volume, which for the work in this thesis could be up to a few millimeters in each direction [Fig. 3.1]. Single crystals are preferable over powders or polycrystals (which are essentially single crystals too small for individual measurement) for many reasons. The ideal single crystal will have a uniform composition and a consistent orientation meaning

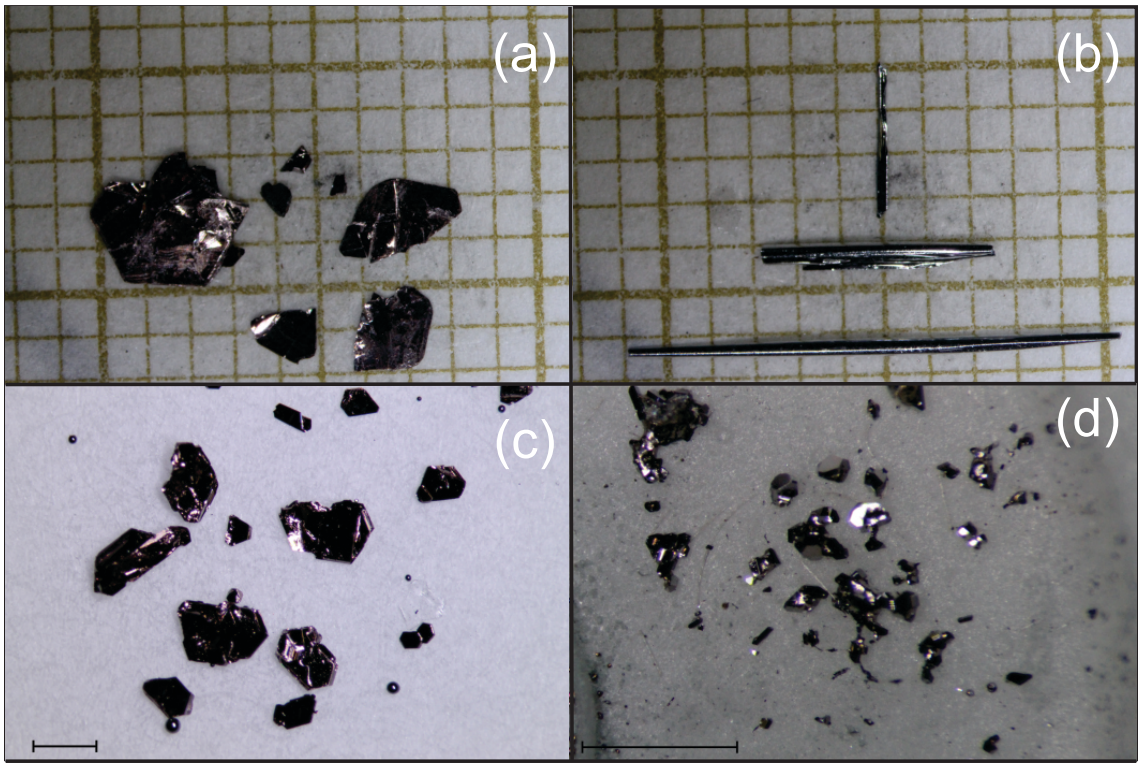

Figure 3.1: Single crystals grown by various techniques. (a) Cu_xTiSe_2 grown by chemical vapor transport with I_2 as the transport agent. (b) Elemental Te grown by chemical vapor transport without a transport agent. (c) $TiSe_2$ grown in a high pressure Ar environment. (d) $Fe_{0.6}Co_{0.4}As$ grown out of Bi flux. The grid in (a) and (b) is made up of 1×1 mm^2 squares, the scale bars in (c) and (d) are 1 mm long.

that there are no grain boundaries that might lead to an extrinsic response in a measurement. In essence, when measuring a single crystal one can be more confident that any behavior is coming from the sample itself. Observations can then be linked to other properties such as sample alignment, which is much more random in a powder or polycrystal. Another consideration is sample purity; there are many phases that can be quenched with small amounts of disorder. In fact, it will be seen that in the case of FeP and FeAs that differences in disorder density between different single crystals have a substantial impact on measured properties, with important features sometimes disappearing for inferior samples. For that reason, much of the effort involved in the work to be presented was spent on sample synthesis, and every measurement to be discussed, outside of powder x-ray diffraction, was conducted on single crystals.

Obtaining a powder of the right composition for the materials to be discussed was often as simple as mixing the raw elements in proportions corresponding to the final ratios and heating them at high temperatures (say, 700-800 °C) for a few days. Growing single crystals can be much more challenging and there are a variety of techniques that might need to be employed for a crystal, with different advantages and disadvantages. This thesis will cover crystal growth extensively, and beyond refinements to previously known techniques will also include synthesis methods not tried before.

3.1.1 Liquid Solvent Flux

Solvent flux relies on the use of additional quantities of a material with a lower melting point than the desired compound [83]. The idea is that the components of the desired material will melt more easily in the liquid flux. This principle can be simply illustrated with table salt (NaCl) and water (H_2O). The melting point of NaCl is 801 °C. However, at room temperature salt can be dissolved in water. This is the principle behind flux growth, where relatively low melting point materials (often elements like Sn, Ga, Pb, or Sb) can be used to dissolve materials with a much higher melting point. The flux may or may not be a component of the desired compound.

For many combinations of two or three elements, phase diagrams are available showing what phases can be formed from different elemental ratios, and the temperature at which the combinations melt [84]. Two examples are given of As-Fe and As-Bi phase diagrams [Fig. 3.2], which were consulted before attempting to grow FeAs from Bi flux. In the phase diagrams, the white region represents solid phases and the purple region liquid ones (though in some cases purple denotes a width of formation, and thus an imprecise or inconsistent stoichiometry). Vertical lines represent concentrations corresponding to stable compounds below their melting temperature, which are connected via horizontal lines. It is possible to determine at what temperature a specific phase will form or melt based on elemental ratios. For example, looking at Fig. 3.2(a) it can be seen that a 45:55 mixture of As:Fe will begin to form both $FeAs_2$ and FeAs at 824 °C, and melt at about 1010 °C.

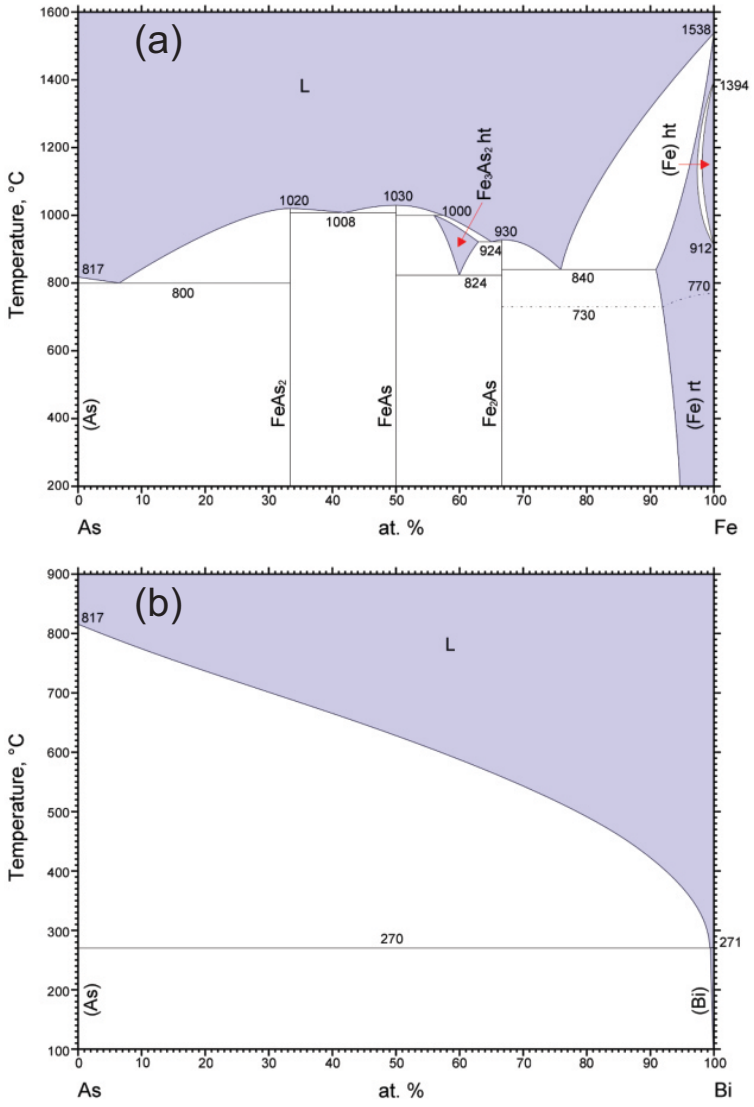

Figure 3.2: (a) The complex As-Fe binary phase diagram. If the two elements are mixed in an equal ratio, the combination will melt congruently at 1030 °C. However, upon cooling not just FeAs, but also Fe_2As and $FeAs_2$, will be formed. Heating the two but staying below 824 °C, it is possible to form FeAs via a solid state reaction without any alternate phases In contrast, As and Bi do not form any compounds together (b), and the melting point decreases monotonically with increasing Bi concentration. Phase diagrams come from [84] by way of https://matdata.asminternational.org/apd/index.aspx.

Even a 1:1 ratio of the two elements will form some material with a 1:2 and 2:1 concentration if heated hot enough. In contrast, As and Bi do not form any compounds together [Fig 3.2(b)]. Their phase diagram is much simpler and depicts only the melting point of the mutual combination, which increases as more As is added. Phase diagrams can be consulted to get a sense of the proper reactant:flux ratio and temperature profile, based on how much the combined elements need to heated to ensure that they all melt, and at what temperature they can be cooled to have solid crystals and liquid flux. However, when combining a large number of elements for which complete phase diagrams are not available, there is often still some educated guessing involved.

Flux growth entails combining the reactants and flux in a crucible (alumina, Al_2O_3, is sufficiently nonreactive for the elements dealt with here, and many others), then sealing the combination in a quartz tube in an inert gas environment with pressure low enough so that as it increases with temperature the quartz will not burst. The combination is put into a furnace which is programmed to reach a temperature high enough so that all components melt based on consultation with phase diagrams. This upper limit is the melting temperature of quartz, a little above 1200 °C. From the peak temperature, the growth is slowly cooled; as temperature decreases, less material can be dissolved in the flux, so gradually more of it will solidify out. Ideally, the cooling step is slow enough and over a large enough temperature range that large crystals, using all of the reactant material, form. There are multiple ways to separate crystals from flux. One option is, while the ampule is still above the melting point of the flux, to very quickly take it out of the furnace and spin it

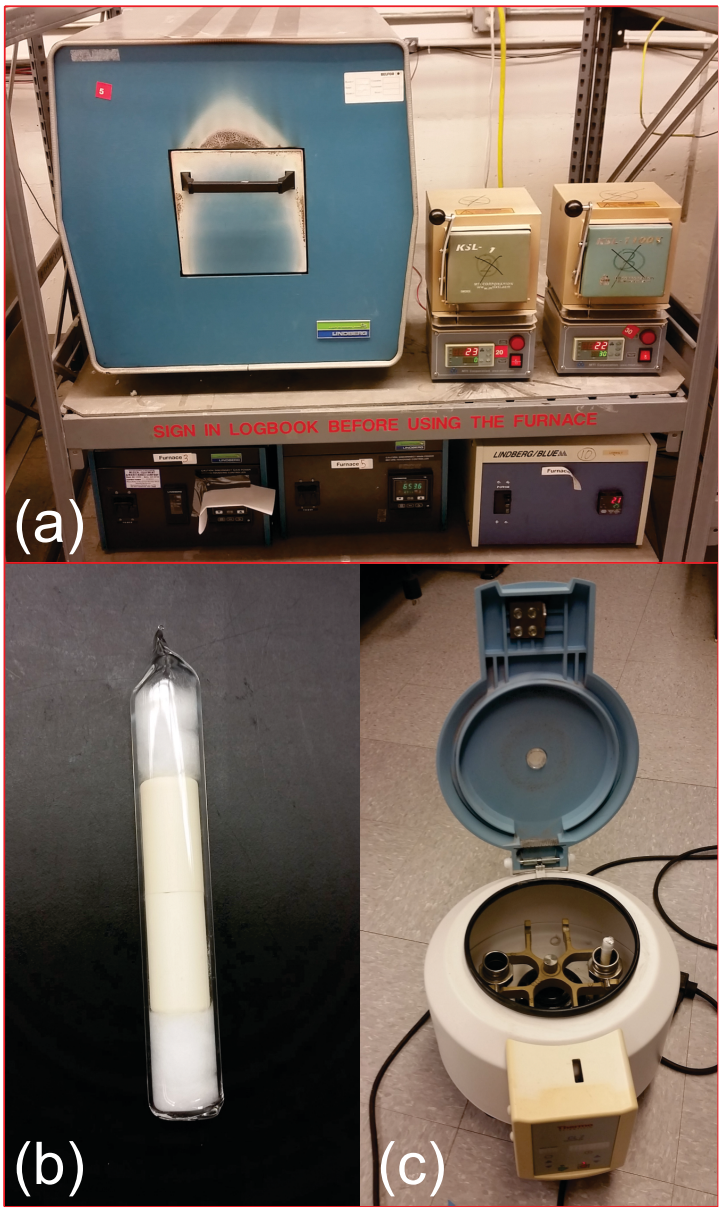

Figure 3.3: (a) Examples of box furnaces (one large, two small) used for flux growth. (b) A sealed quartz ampule containing two alumina crucibles. The bottom crucible contains all the reactants, the top crucible has quartz wool to separate liquid from solid during centrifugation. Quartz wool above and below the crucibles prevents them from hitting the ends of the ampule too hard and potentially breaking it. (c) A centrifuge used to separate liquid flux from solid crystals. Counterweight is provided by coins in the bucket opposite the sealed ampule.

in a centrifuge, thereby separating the crystals and liquid. This is what was done for flux growths in this work. During this process the centrifuge was kept on for only about five seconds until reaching a maximum angular speed of 2000 rev/min. Another option is to cool the combination down to room temperature, and separate the solid crystals and now solidified flux either mechanically or through the use of chemical etchants that preferentially attack the flux.

3.1.2 Chemical Vapor Transport

In contrast to the flux method, which is based in solid-liquid equilibrium, in chemical vapor transport (CVT) material is converted to the gas phase [85]. The reactants are again sealed in a quartz ampule, but this time without a crucible and at a pressure as close to vacuum as possible. The aim is to avoid any unwanted gases in the ampule, and to make it easier for the reactants to boil. Beyond the elements that will make up the final crystal, a "transport agent" may also be included. This is a material with a high vapor pressure and/or low boiling point that makes it easier for the reactants to form gaseous compounds. A typical choice is one of the halogens, either on its own or as part of a compound. Of these the most common is iodine, since it less harmful than bromine or chlorine (which is often included as HCl or $TeCl_4$) and is solid at room temperature. However, there are many other possibilities. Chalcogen-containing materials, for example, can often self-transport [86,87], and even water vapor or O_2 are options in some cases. For elements with high melting points, it is even possible to use their oxides and enable solid-gas reaction

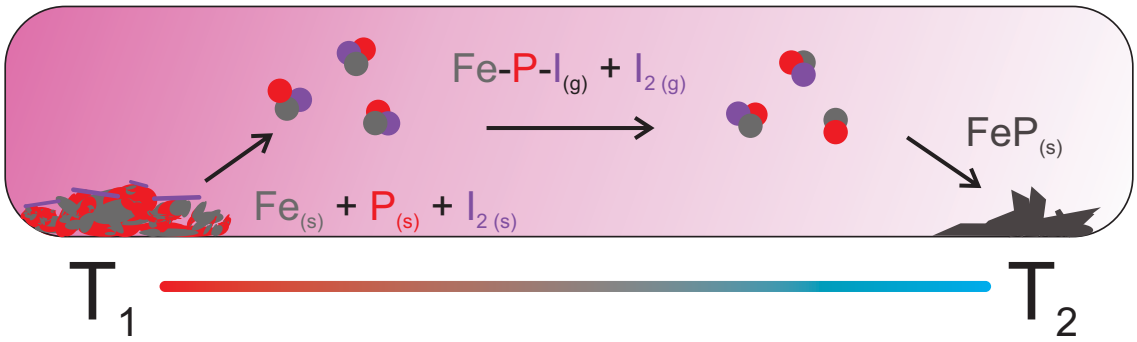

Figure 3.4: A diagram depicting the formation of FeP single crystals through CVT. The raw elements, including the transport agent I_2, are mixed together and sealed at vacuum at one end of a tube. The formation of gas from the solid reactants is endothermic, and so more favorable at higher temperatures. Applying a temperature gradient ($T_1 > T_2$) results in the consumption of solids at the hot end, and formation of single crystals of FeP from the gas phase at the cold end.

by an oxidation-reduction reaction [88]. In fact, CVT was first recognized in nature rather than the lab, as the mechanism by which hematite (Fe_2O_3) crystallized upon interaction with HCl gas during the eruption of volcanos [85].

CVT takes advantage of the fact that a change in temperature will change a chemical reaction rate. The CVT ampule is placed in a temperature gradient, with the reactants at one end of the tube. They will then form a gas (reacting with the transport agent, if there is one) which will fill up the entire volume of the ampule. At the other end of the tube, the gas condenses and forms single crystals of the desired compound. The position of the reactants at the hot or cold end depends on whether the initial solid to gas reaction is endo- or exothermic. The majority of such reactions are endothermic and consume heat, and thus have a higher rate at higher temperature. In that case, the reactants are placed at the hottest point in the tube and crystals form at the cold end, where condensation into a solid phase is more thermodynamically favored. For exothermic reactions, it is the opposite.

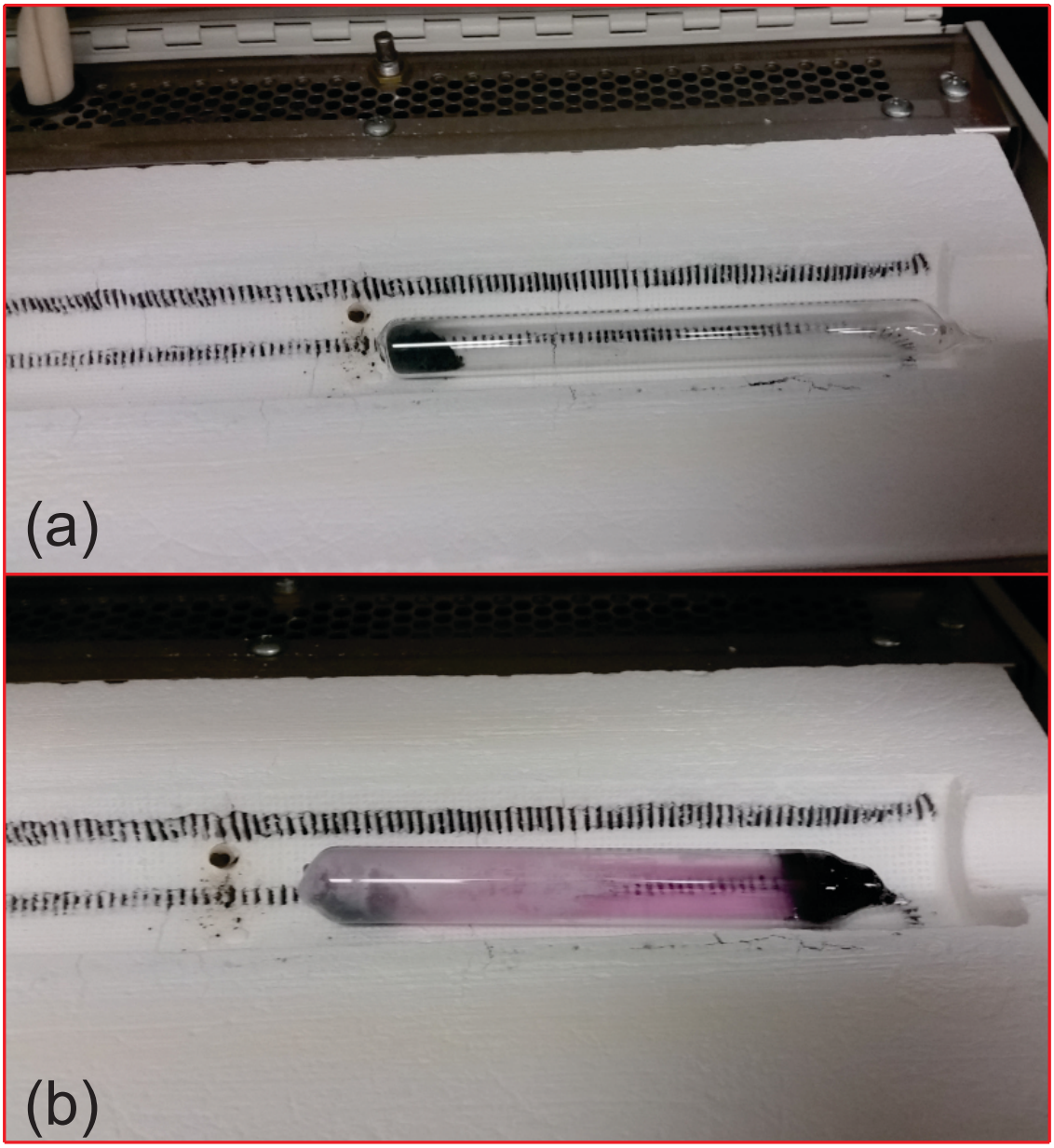

Figure 3.5: Photographs of two different CVT growths of WP using WO_3, P, and I_2 as starting material. (a) An ampule before heating, with the reactants at the end closer to the center of the single zone tube furnace, which is the hottest point. (b) An ampule after the growth process, with the furnace still slightly above room temperature. The pink color indicates the presence of iodine vapor, and most (though in this case not all) of the material has moved to the colder end, which is noticeably darker than it was initially.

There are many potential variables in CVT. Crystals will often be formed only through the use of certain transport agents. The temperature and gradient are also crucial. The intermediate gas phase frequently will not have the same stoichiometry as the final desired product, so an incorrect choice can easily change the stoichiometry of the crystals or form undesired phases. Work with FeSe in a two-zone furnace has demonstrated the sensitivity of crystal quality to small changes in temperature gradients based on ampule position, length, and even the angle the furnace is tilted at [89].

Vapor transport growths described in this work were done in single zone horizontal tube furnaces. There was a heater and thermocouple in the middle of the furnace. As a result there was a natural hot-cold gradient from the middle to either end of the furnace over a distance of 15 cm. The middle temperature could be set with the furnace temperature controller, but the gradient could vary somewhat with temperature; at the high ($>$ 800 °C) temperatures used here, the temperature difference between the middle and end of the furnace was about 200 °C. The temperature difference could be adjusted by varying the length of the ampules, and the temperature at specific locations in the furnace could be fond with a handheld thermocouple rod placed into the furnace that gave immediate readings.

3.1.3 Growth Details

Having introduced the techniques, the specifics for the growth of each system to be explored will now be given. FeAs and CoAs samples were grown by both flux

and CVT in very similar conditions. For the case of flux growth, Bi in a 20:1 ratio with prereacted FeAs or CoAs powder was put into an alumina crucible and sealed in a quartz tube in partial Ar atmosphere. The growth was heated at 50 °C/h to 900 °C and remained there for two hours. The furnace was then cooled at a rate of 5 °C/h to 500 °C, at which point the ampule was spun in a centrifuge to separate crystals from flux. For CVT, powders were loaded with polycrystalline I_2 into an evacuated quartz tube, which was placed in a temperature gradient such that the end initially containing the reactants was at 830-950 °C and the cold end at 600-750 °C. Generally, it seemed that CoAs grew better at temperatures on the lower end of this range, while the Fe-based compounds formed larger and more quickly at higher temperatures. In both cases CVT led to large, polyhedral crystals, while those grown with flux had more regular shapes: needlelike in the case of the arsenides and more three dimensional for CoAs. The needlelike samples grew mostly along the b-axis, which is to be expected since it is the shortest principal axis.

It was found that high quality FeP samples could only grow through CVT, possibly because of the lighter mass and lower boiling point of P (281 °C) compared to the sublimation point of As (615 °C). Several different fluxes were tried, the only partially successful one was Sb. However, samples were small and showed magnetoresistance similar to that of Sb, indicating residual flux in the crystals even after polishing. Later attempts to grow CoP were done only with the CVT for this reason. The best quality FeP samples were found to grow from CVT using elemental Fe and P with I_2. Attempts made with prereacted FeP powder led to samples with a higher low temperature resistivity, a sign of increased impurity scattering, though

in the case of CoP the two sets of starting conditions gave similar results.

Interestingly, energy-dispersive x-ray spectroscopy (EDS) measurements on both kinds of samples, from which elemental ratios can be extracted, very consistently showed a 55:45 Fe:P concentration in the high quality crystals grown from the elements, but a ratio very close to 1:1 in powder-grown crystals. It may be the case that P vacancies (or Fe self-doping) contribute to enhanced crystal quality, and may also possibly influence the band structure of Fermi energy position to increase the density of states at E_F. CoP samples grown also showed about 10% excess Co (or deficient P) when grown from either the elements or powders, and the choice of reactants did not seem to have a significant impact on crystal quality. No attempts were made to synthesize FeAs or CoAs directly from their elemental components, due to the hazards associated with vapor transport of elemental arsenic.

In the case of mixed $Fe_{1-x}Co_xP$ and $Fe_{1-x}Co_xAs$, flux growth was initially attempted for the arsenides. However, samples produced in that way were too small and so CVT was used instead. The temperature was varied between that of the iron and cobalt compounds based on the x value. Often, single crystals were found at both ends of the ampule upon opening. Those at the cold end (which had fully transported) typically had compositions similar to nominal x value from EDS, while those still at the hot end were often Co deficient.

3.2 Measurements at the University of Maryland

Using facilities at the University of Maryland, it was possible to measure chemical composition and structure, electrical resistance, heat capacity, or magnetic susceptibility at ambient pressure.

3.2.1 Structural and Compositional Characterization

With different tools, it was possible to assess that samples had the correct structural as well as elemental composition. Powder x-ray diffraction (XRD) measurements were made with a benchtop Rigaku Miniflex 600 diffractometer. The theory and implementation of x-ray diffraction are well-described elsewhere, such as Ch. 6 of Ref. [43]. Succinctly, as the angle of both the sample and detector are changed, peaks in diffracted intensity will appear when the Bragg condition $2d\sin\theta = m\lambda$ is satisfied. Here d is the distance between two diffraction planes, θ is the angle from the horizontal at which x-rays meet the sample, m is a natural number, and λ the x-ray radiation wavelength. Cu K_α ($\lambda = 1.5406$ Å) radiation was used in the Rigaku Miniflex system. Every compound will have a unique XRD pattern, with the peak positions determined by the crystal structure and lattice constants, and the intensities determined by the space group and elemental composition. With knowledge of a material's structure and composition it is possible to predict the x-ray pattern, and vice versa. Single crystal samples were oriented through a combination of single crystal x-ray diffraction at UMD with the Miniflex system and Laue photography at the NIST Center for Neutron Research.

Energy-dispersive energy spectroscopy makes it possible to measure the elemental composition of sample using x-rays emitted after interaction with an electron beam. These measurements were performed over a 15 keV energy range with a Hitachi S-3400 variable pressure scanning electron microscope located at the FabLab on the UMD campus. High energy electrons from the beam will excite core electrons in the sample. Higher level electrons will drop down to fill the created holes, emitting an x-ray in the process. A detector reads the energy of these x-rays, which can be compared to known values corresponding to specific transitions for specific elements. The intensity of emitted x-rays at different energies can be used to determine the ratio of elements in the sample. EDS results are completely independent of crystal structure. This is potentially a problem when multiple phases could be present, as it can be hard to determine by elemental ratios alone if the sample is composed exclusively of one compound, or multiple with their own individual weights. However, it is beneficial if there are potential vacancies or excesses of an element within the material, or when carrying out substitution studies, as in the case of $Fe_{1-x}Co_x$(P,As).

3.2.2 Electrical Transport

Electrical resistance was measured at UMD in a Quantum Design 9 T, 14 T, or 14 T DynaCool Physical Properties Measurement System (PPMS). The wiring configuration for transport measurements is shown in Fig. 3.6. Gold or silver wires were attached to the surface of samples using EPO-TEK H20E silver epoxy or DuPont

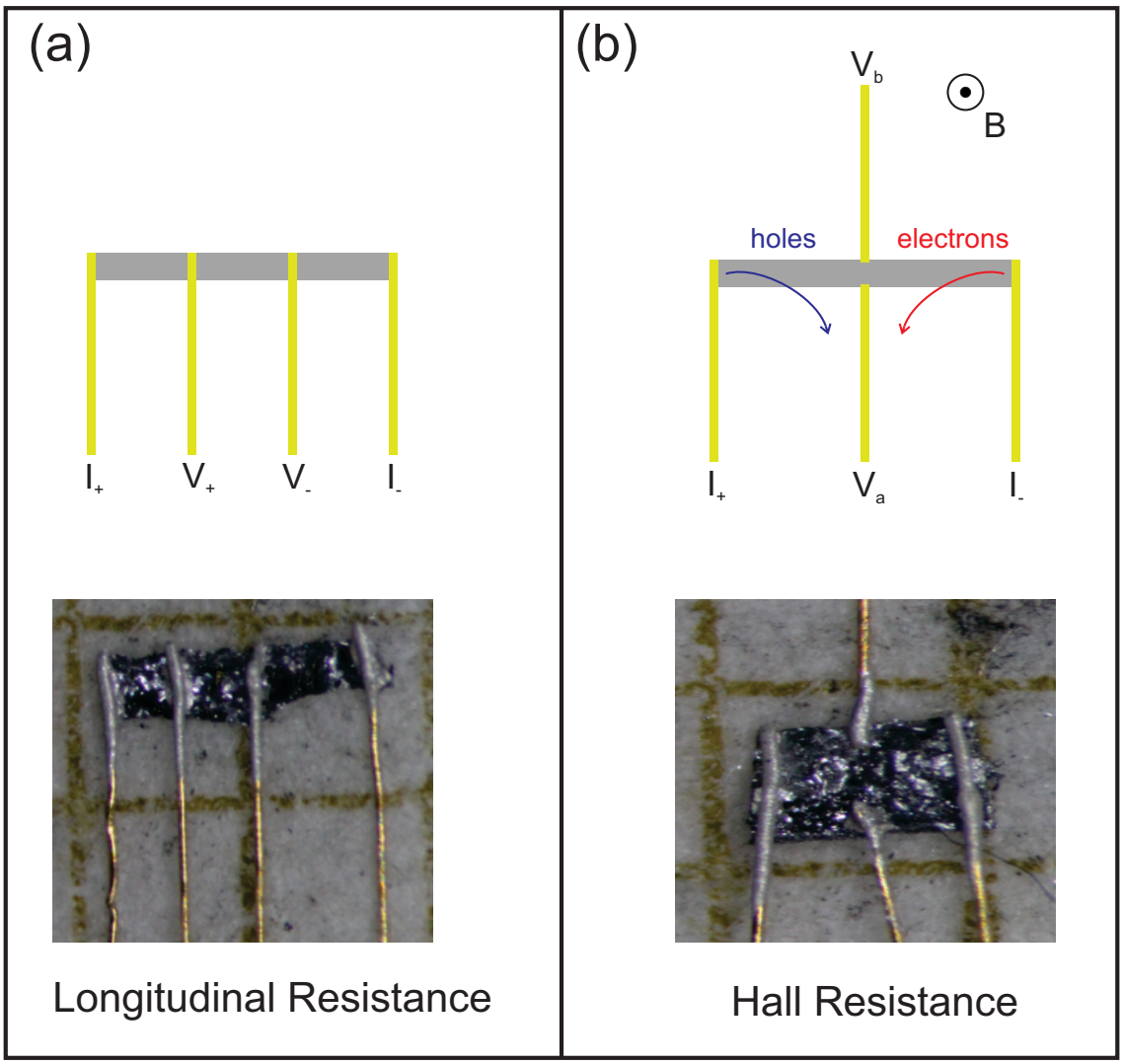

Figure 3.6: Gold wires attached with silver paste to the surface of Bi_2Se_3 single crystals, configured to measure (a) longitudinal and (b) Hall resistance. Arrows in (b) show how positively charged (hole) and negatively charged (electron) carriers will be deflected in the presence of a magnetic field directed out of the page from their straight paths along the applied current direction, leading to a transverse voltage difference. V_a - V_b will be positive for hole carriers and negative for electron carriers. If both are present, then the individual carrier concentrations and mobilities determine the sign.

4929N silver paste thinned with 2-butoxyethyl acetate, and contact resistances were generally around 1-3 Ω. Samples were then placed onto a puck designed for use in the PPMS, and the wires were soldered to pads that provided electrical connections to send in current and measure voltage. Voltage was converted to resistance using Ohm's law, $R = V/I$. Specific pucks were also used that allowed one dimensional rotation in magnetic field in the PPMS. Both the longitudinal and Hall resistance were measured. The difference in setup between the two is in the arrangement of the voltage wires [Fig. 3.6]. For a standard resistance measurement, the four wires are arranged parallel across a sample. The outer two serve as a source and sink of current, and the voltage difference across the middle two is measured. The longitudinal resistivity ρ_{xx} can be obtained from a combination of the resistance and geometric factors: $\rho_{xx} = R_{xx}\frac{w \times t}{l}$, where w, t, and l are the sample width, thickness, and length (separation between voltage leads). The resistivity is an inherent property of a material and thus is of greater relevance than the resistance, which depends a sample's shape. Ideally, samples used for longitudinal resistance measurements are long, thin, and narrow, which will maximize the measured resistance and ensure that current is directed primarily along a single direction between the two current leads, and does not have any perpendicular component that distorts the resistance-resistivity conversion.

The Hall effect was covered theoretically in the previous chapter. The Hall voltage is the potential difference arising along the $\hat{y}$ direction for current in the $\hat{x}$ direction and magnetic field in the $\hat{z}$ direction[1]. When a current is applied to a

[1]Planar Hall measurements, where field is not perpendicular to the current-voltage plane, are

sample, electrons and holes move in opposite directions with opposite charge. In the presence of a magnetic field, carrier paths will curve as they acquire a $\hat{y}$-axis component dictated by the Lorentz force. For the two carrier types, their opposite charges and velocities cancel and both carrier types are accelerated in the same perpendicular direction. As a result there will be a buildup of either positive or negative charge at one of the voltage leads, which are now on opposite ends of the sample perpendicular to the current leads [Fig. 3.6(b)].

The complexities of interpreting this signal were covered in the previous chapter. Experimentally, one issue is that for a metal R_{xy} can often be much smaller than R_{xx}. For that reason it is important to align the two voltage leads with as little lateral offset as possible, to avoid picking up any longitudinal resistive component. This can be challenging, so often the Hall response must be antisymmetrized for positive and negative fields. Since the longitudinal magnetoresistance is symmetric in field, doing this will ideally cancel out a longitudinal component, leaving just the Hall resistance. In cases with very small R_{xy}/R_{xx}, even this may not result in a clean signal.

To convert resistance to longitudinal or Hall resistivity, dimensions were measured using pictures of the samples taken through a microscope and software to convert microscope magnification to length. The photographs in Fig. 3.6 show some of the uncertainty inherent to single crystal transport measurements. While samples pictured are relatively nicely shaped, their thickness and width are not constant across their length. The need to measure the distance between voltage leads also

of interest in some topological systems, but will not be covered here.

leads to some error. The leads used in these studies were either 50 μm or 25 μm, while the separation could often be on the order of hundreds of μm. Beyond that, the silver paste itself spreads out upon making contact to the sample surface. It is difficult to know exactly where the best contact is being made, so for consistency distance was measured from the middle of each voltage contact in calculating the geometric factor. For this reason, resistivity values shown here should be understood to have an inherent uncertainty of perhaps 5%. For that reason, the increase or decrease of resistance, scaled to its room temperature or low temperature value, is often a more reliable measure of quantities such as impurity scattering. The residual resistivity ratio (RRR) is $\rho(300\text{ K})/\rho_{base}$ (typically 1.8 K here), and is commonly used as a marker of sample quality, with higher RRRs corresponding to lower impurity scattering at low temperature for (presumably) the same room temperature resistivity.

3.2.3 Heat Capacity

The heat capacity $C_p = \left(\frac{dQ}{dT}\right)_p$ was measured by the relaxation method either in the 14 T or 14 T DynaCool PPMS systems. Samples were affixed with Apiezon low temperature N grease to a thermally isolated stage, and the chamber was set to high vacuum ($<$ 10 mTorr, and as low as 1×10^{-4} Torr at low temperature). During a measurement, a known quantity of constant heat is applied for a specified length of time, and the cooling of the entire setup measured for the same amount of time afterward. The temperature of the platform obeys a differential equation:

$C_{\text{total}}\frac{dT}{dt} = -K_w(T - T_b) + P(t)$. C_{total} is the total heat capacity of the sample and platform, K_w the thermal conductance of the wires connected to the platform, and $P(t)$ the power applied to the stage—is constant during heating, zero at all other times [90]. The solution of this equation is an exponential function with a characteristic time $\tau = C_{\text{total}}/K_w$. K_w is known, so the total heat capacity can be solved for with a model incorporating the data from the heating and cooling periods. This fitting is done by the PPMS software itself. Since it is only possible to obtain the total heat capacity, before measuring the sample addenda measurements must be made. That means that a heat capacity measurement must be made in the same temperature range with just the stage and the grease before measuring the sample. For measurements in field, addenda measurements at each field are necessary. The addenda heat capacity can then be subtracted from the total to get C_p for the sample alone. When thermal contact is not as good, another term can be added to the differential equation to account for thermal conductance between the platform and sample. The PPMS software automatically fits both equations, and the value for the heat capacity comes from the fit with a smaller deviation.

Heat capacity was converted to specific heat by measuring sample mass and using the compound's molar mass. At low temperatures ($T << \theta_D$), the Debye model predicts that the specific heat will obey the relation

$$C_p = \gamma T + \beta T^3 \tag{3.1}$$

in the absence of contributions from magnetism, superconductivity, or other

ordered phases. It is convenient then to divide by temperature and plot C_p/T vs. T^2, which should be linear, with γ the y-intercept and β the slope. $\gamma = \frac{\pi^2 k_B^2 N_A}{3\mathrm{E}_F}$ is the Sommerfeld coefficient. Here N_A is the Avogadro number. The Fermi energy can also be expressed as $\frac{\hbar k_F^2}{m^*}$, meaning that there is a linear relation between γ and the effective mass. The Sommerfeld coefficient is also a general indicator of a larger density of states at the Fermi energy-metals will have larger γ values than insulators. Very large values, on the order of 100 mJ/mol K or more, are seen in the heavy fermions and signify significant electron-electron correlations that lead to large effective carrier masses. β can be used to calculate the Debye temperature $\theta_D = \left(\frac{12\pi^4 k_B N_A n_{f.u.}}{5\beta}\right)^{\frac{1}{3}}$, with $n_{f.u.}$ the number of atoms in the formula unit.

3.2.4 Magnetic Susceptibility

Measurements of the magnetic susceptibility χ can reveal magnetic properties of materials. In such measurements, a magnetic field is applied and the sample's response measured. In such a way the magnetization $\mathbf{M} = \mathbf{B}/\mu_0$ - $\mathbf{H}$ can be measured. Magnetic susceptibility was measured in two ways: using a superconducting quantum interference device (SQUID) or a vibrating sample magnetometer. The SQUID MPMS was either an MPMS-XL or MPMS3, both of which had a maximum field of 7 T. The MPMS3 also had a VSM option, as did the PPMS DynaCool with a maximum field of 14 T. Susceptibility was converted to magnetization by measuring sample mass and using the known chemical formula.

The DC SQUID option of the MPMS works by moving the sample through

superconducting coils, which are wound so as to be sensitive only to disturbances of the magnetic field within them [91]. These coils are inductive coupled to a SQUID, a superconducting loop featuring two Josephson junctions on opposite sides. Magnetic flux Φ through the SQUID changes the phase difference of the two Josephson junctions, causing the voltage to oscillate. In that way, the SQUID is very sensitive to small magnetic fields, and the resolution of the newer MPMS system was $< 10^{-8}$ emu [91]. A VSM places the sample in a magnetic field and oscillates it vertically, and uses a pickup coil to convert the change in Φ in the middle of the oscillation minimum and maximum to a voltage. For the PPMS and MPMS3 systems, the sample is oscillated by 1-3 mm at a rate of 40 Hz [90]. The induced voltage $V = \frac{d\Phi}{dt} = \frac{d\Phi}{dz}\frac{dz}{dt}$. This in turn is equal to $2\pi f \cdot mC \cdot A\sin(2\pi f t)$, where C is a known coupling constant, m the sample's magnetic moment, A the oscillation amplitude (a length), and f the oscillation frequency. Therefore, in knowing the voltage one can extract the magnetic moment. The system is able to resolve signals below 10^{-6} emu. While the sensitivity is not as great as that of a SQUID, one advantage is that there is no field limit on the VSM systems, and so they could be used up to 14 T. In contrast, the maximum field of the SQUID is 7 T.

3.3 High Magnetic Field

While temperature is almost certainly the most commonly tuned parameter in basic materials research, magnetic fields offer the chance to cover a much larger scale. The typical temperature range of the experiments in this thesis is about 1-300 K.

In contrast, magnetic fields can be reliably controlled from 10^{-3} to 35 T, spanning four orders of magnitude. In Ch. 2 it was seen that by interacting directly with the magnetic moments of particles, magnetic fields can alter interactions and induce new phenomena, a relevant example being the destruction of the superconducting state at a "critical" field. Magnetic fields can also reveal fundamental properties, as in the case of quantum oscillations and the related concept of Fermiology. For this reason studying the behavior of materials in a magnetic field is another crucial element in understanding them.

The United States' National High Magnetic Field Laboratory (NHMFL) is capable of reaching the highest nondestructive magnetic fields on the planet[2]. There are several different user facilities: the High B/T Facility in Gainesville, Florida, the Pulsed Field Facility at Los Alamos National Laboratory in New Mexico, and the DC Field Facility in Tallahassee, Florida. This thesis will focus on work done at the last of these, over several weeklong allocations of magnet time that were granted through different experimental proposals. The DC Field Facility has magnets which, as the name suggests, provide a constant, steady magnetic field; Fig. 3.7(a) shows what one of the magnet cells looks like. This is in contrast to the Pulsed Field Facility, where the magnets have higher maximum fields but reach them for far less than a second. The High B/T Facility has weaker magnets, but specializes in very low temperature measurements. High temperature superconductors such as the cuprates have critical fields exceeding the 100 T that the Pulsed Field Facility can reach nondestructively.

[2]It vies for records related to high magnetic fields, under various conditions, with facilities in China and Europe.

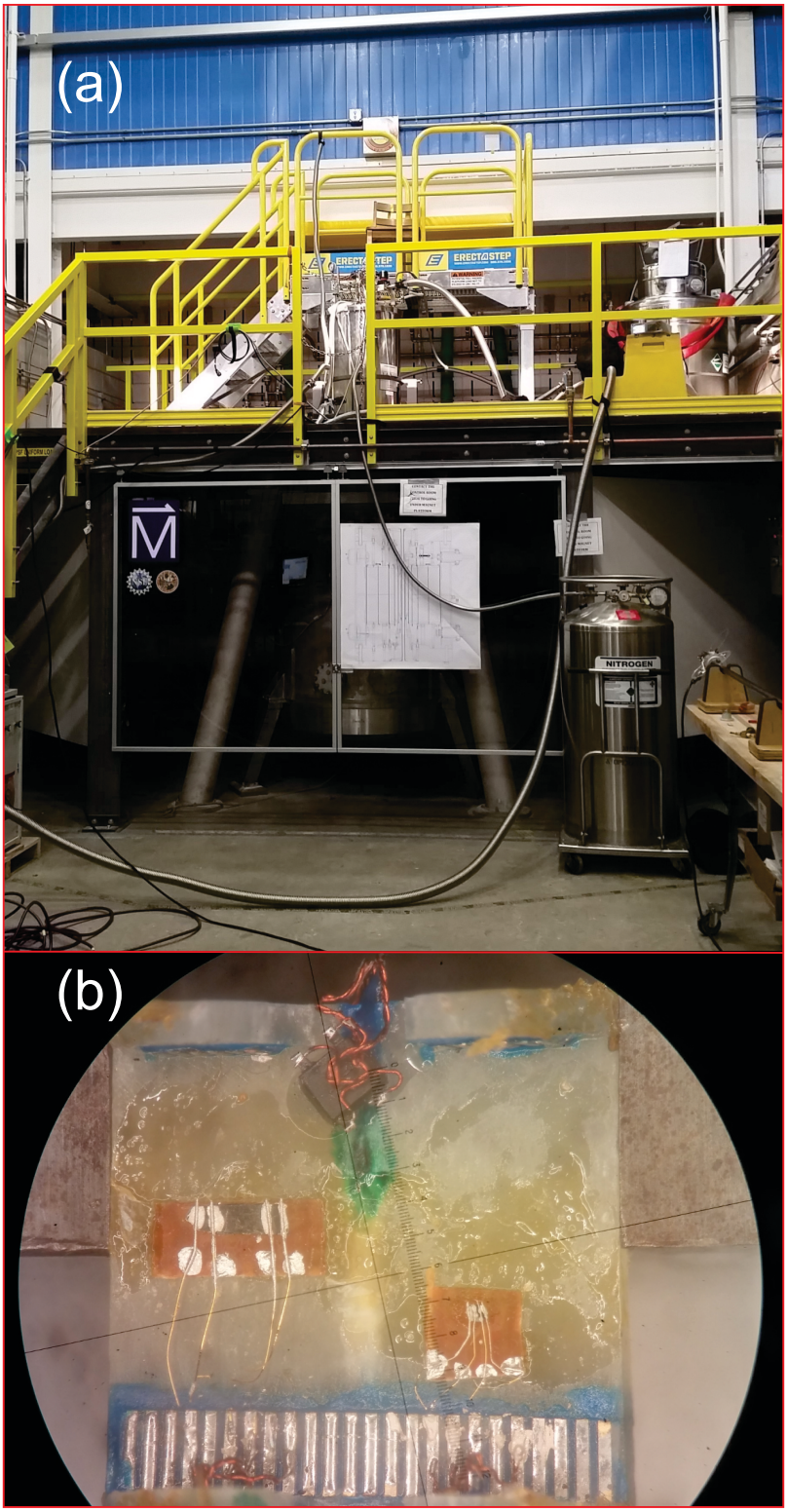

Figure 3.7: (a) Cell 6 of the NHMFL. The top of the cryostat is on the platform, the 41.5 T magnet itself is underneath, behind the darkened panel. (b) (left) YPtBi and (right) CoAs electrical transport samples on a sample platform for measurement on a rotating probe at the NHMFL. Photograph in (b) courtesy of D. Graf, NHMFL.

There are more exotic materials can see superconductivity strengthened in magnetic field, such as the recently discovered spin-polarized superconductor UTe_2 [4], where increasing field eliminates a first superconducting state before another emerges at still higher fields. High magnetic fields can lift the shroud of superconductivity or other field-antagonistic phases that obscure inherent sample properties. In FeP, the magnetic field response increases the resistance by a factor of over 100. It even causes the resistivity to increase with cooling at low temperature, i.e. to exhibit nonmetallic behavior. All of these effects are enhanced, or perhaps only noticeable, at high magnetic fields, hence the reason facilities dedicated to such work exist.

The resistive magnets have maximal fields on the order of 30-35 T, though very recently a new magnet has been opened to users with a 41.5 T maximal field. Also available is a "hybrid" magnet in which a 33.5 T resistive magnet is surrounded by an 11.5 T superconducting magnet, resulting in a 45 T total field. For comparison, the highest field available to most nonspecialized facilities is about 20 T, due to impracticalities associated with both the electricity and cooling water a resistive magnet consumes. The highest field for instruments at the University of Maryland used for this thesis was 14 T.

The longitudinal electrical resistance and magnetic torque of samples were measured in several different DC magnets at the Tallahassee facility, with maximum fields of 30.5-35.1 T. Base temperature using a ^{3}He refrigeration system varied from about 350-450 mK during different measurement periods. There were minimal differences in operation of each magnet. A 16 or 32 pin connector platform attached to the end of a probe made allowed for multiple samples to be measured at once.

The platform could also be rotated through a single axis. Field was generally swept at 2 T/min, and measurements were typically done in constant temperature and angle with variable field. This is the typical approach as changing temperature in steady field would be costly in terms of both electricity and time, and at low temperatures the thermometers are not well calibrated in field. Occasionally, field was held constant while the sample platform was rotated.

3.3.1 Electrical Transport

Transport measurements at the NHMFL were for the most part very similar to those done at in the PPMS systems. Contacts were made on the samples by attaching Au wires with Ag paste or epoxy, and the samples were mounted with GE varnish to platforms made of sapphire, G-10 (fiberglass), or some other insulating material, as seen in Fig. 3.7(b). These could then be positioned on the probe platform itself with the desired orientation.

3.3.2 Magnetic Torque

It is also possible to measure magnetic torque in DC fields using piezoresistive cantilever magnetometers [92, 93]. This is a very sensitive probe of the torque $\tau = \mathbf{m} \times \mathbf{B}$. The sample is attached to two small legs, the cantilevers, extending out from a silicon chip [Fig. 3.8]. A layer of the chip is heavily doped with boron to make it conductive. Interaction between the sample moment and magnetic field will result in a torque, which will cause the sample to move and the cantilevers to

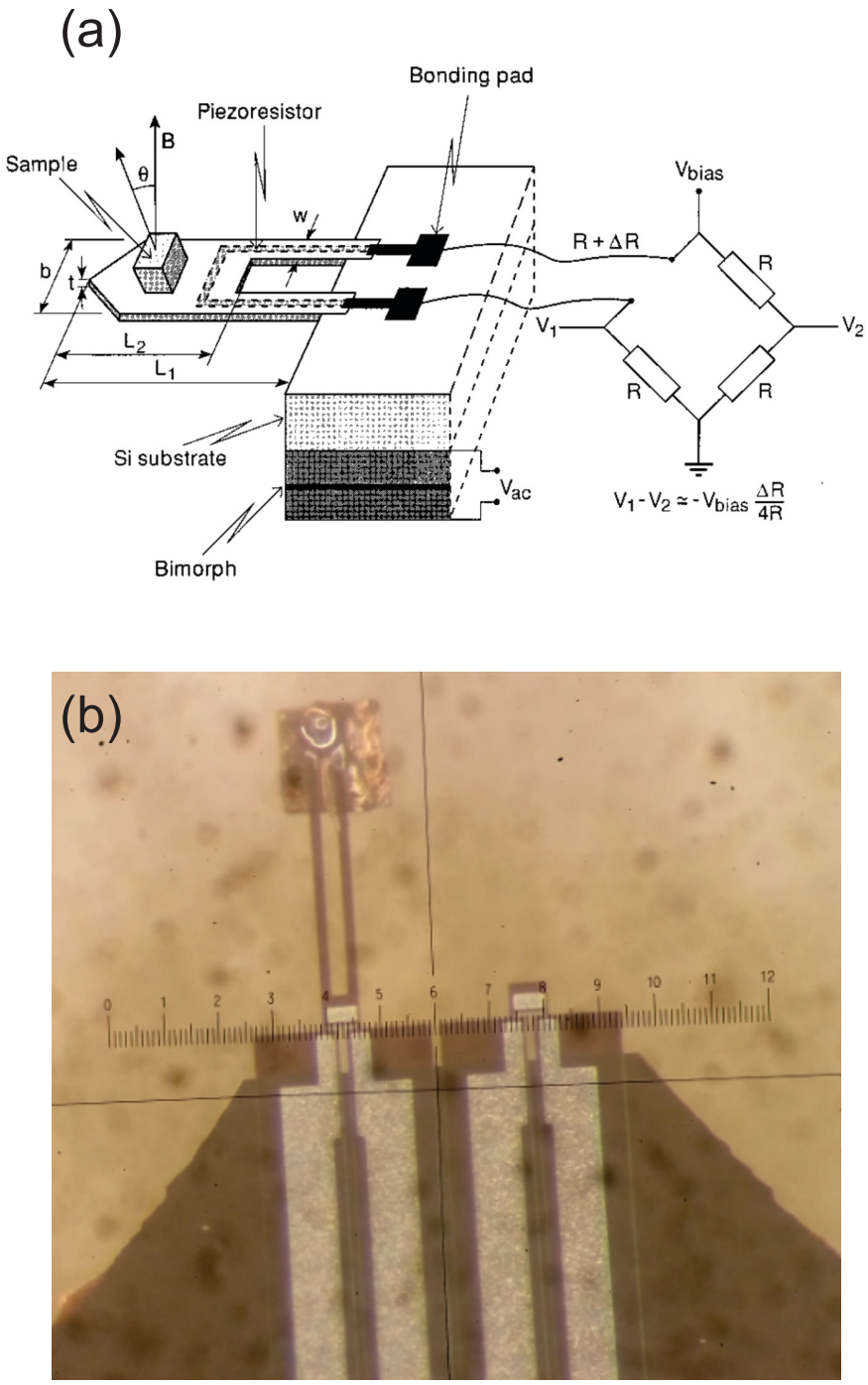

Figure 3.8: (a) Diagram of a piezoresistive torque cantilever, taken from Ref. [93]. A sample is mounted on a stage, which will bend due to the torque experienced in field. The change in resistance of the Si:B due to the piezoresistive effect can be obtained with a Wheatstone bridge. (b) An FeAs crystal mounted on a cantilever for measurement at the NHMFL DC Field Facility. Sample size is approximately 75 $\times$ 100 μm^2. Photograph courtesy of D. Graf, NHMFL.

bend. This bending leads to a change in the length and strain of the Si:B, and thus resistance through the piezoresistive effect. That resistance change can be measured with a Wheatstone bridge through the two leads coming off of each leg (four total). Measuring this change in resistance is a proxy measurement of magnetic torque with arbitrary units (Ohms or Volts). In theory, this can be converted to N·m with knowledge of sample mass, and calibration of the chip. However, this was not done since only the relative change in the torque was relevant for quantum oscillations measurements[3].

The doping level of the Si chip means that small strains can generate a large voltage, making this an extremely sensitive technique, with sensitivities on the order of 10^{-12}-10^{-14} N·m readily achievable [92]. Indeed, torque is in many cases preferable to resistance for the detection of magnetic transitions or quantum oscillations; the signal is often cleaner and the background simpler to subtract. In FeAs and CoAs, for example, quantum oscillations were seen in torque at fields as low as 5 T, but not at all in resistance even above 30 T. Torque samples are much smaller than those required for resistance measurements, with dimensions on the order of 100 μm or less. Crystals that are too large can bend the cantilever, either with a large mass or with too strong of a field response. This can lead to a nonlinear resistive response and corrupt the measurement. There are some drawbacks to the torque method, such as the difficulty of converting to non-arbitrary units. Additionally, the torque signal is typically very small when field is aligned along crystal axes and the cross

[3]While the torque is perpendicular to the magnetic field, for the purposes of quantum oscillation measurements only the field direction is relevant, because the formation of Landau levels is determined by the direction of the B, not τ.

product disappears. Still, the torque method was very useful due to its extreme sensitivity and ability to measure samples too small to fit four wires onto.

Chapter 4: Crystal Quality and Quantum Oscillations in FeAs

4.1 Introduction

The first material to cover, and in fact the first material studied chronologically, is FeAs. It is, after all, the most direct link to the iron-based high-temperature superconductors, which as mentioned include tetrahedrally-coordinated Fe-As layers. The interest lay in what happens in a simple binary, with octahedral coordination. The spin density wave transition at $T_N = 70$ K has been well established [24, 30, 94–96]. However, unlike the iron pnictides, CrAs, or MnP, FeAs does not superconduct with either chemical substitution [25, 26, 97] or pressure [94]. Evidently, there is something in the the electronic structure and/or magnetic interactions of FeAs to set it apart.

FeAs orders in a noncollinear spin density wave (SDW) state consisting of unequal moments along the a- and b-axes with propagation along the c-axis [96, 98]. There are some differences from the helimagnetic state that is mostly unchanged in MnP, CrAs, or FeP. Both spin amplitude and direction are modulated, and there is possible canting into the propagation direction. Despite a good deal of work on the properties of FeAs there still exists uncertainty about many aspects of its electronic structure and what drives its magnetic order. Theoretical work predicted

the paramagnetic and AFM Fermi surfaces to differ substantially, with the AFM Fermi surface consisting of a single electron pocket at the Γ point surrounded by four identical hole pockets [99]. However, the AFM state associated with this Fermi surface is a more conventional arrangement of alternating up or down spins, rather than the experimentally observed SDW [98–100]. If the magnetic ordering does not match experiment, than it is hard to take predictions for its properties as fact. Hall effect measurements have shown the coexistence of both hole and electron carriers over a wide temperature range, but disagree over the dominant low temperature carrier [40, 95, 101], which may be directionally dependent.

The following chapter will present a method to grow binary FeAs crystals using Bi flux, which produces samples with a larger residual resistivity ratio than has been previously reported [24, 94–96, 98, 101, 102], which generally indicates better crystal quality. These crystals show quantum oscillations in magnetic torque measurements at high fields, which can be analyzed to give a more complete picture of the electronic structure of FeAs below T_N, allowing for comparison to previous theoretical and experimental results.

4.2 Experimental Details

In previous studies, FeAs single crystals were made via CVT with I_2 [24, 94–96, 98, 101] or from Sn flux [102]. In an effort to improve sample quality, attempts with other fluxes such as Sb, In, and Sn were made. Ultimately Bi was found to work, in part because it conveniently does not form compounds with either Fe or As, and any

residual flux stayed on the surface of crystals and could be polished away, rather than embedding itself within the samples as was the case with Sn. At low temperatures, the resistivity is much smaller in Bi flux crystals, and accordingly the RRR much higher. RRRs consistently exceeded 70 with a maximum of 120, compared to 20–40 with other growth methods [95, 101]. Given that RRR (and correspondingly, the residual resistivity value) is often accepted as a measure of crystal quality, it seems that Bi flux growth results in the highest quality FeAs single crystals yet produced.

The crystal morphology of Bi flux samples is distinct from the polyhedral or platelike samples resulting from with CVT or Sn flux. Crystals grown in Bi flux are needlelike (Fig. 4.1, inset), with typical dimensions of $0.03 \times 0.03 \times 0.8$ mm^3. Powder x-ray diffraction measurements give the lattice parameters $a = 5.44$ Å, $b = 3.37$ Å, and $c = 6.02$ Å, in line with previous results[1] [24, 95, 96]. The long direction of the crystal was always the b-axis, as verified by Laue photography and single crystal XRD and inferred from the initial increase in resistivity with decreasing temperature that is unique to measurement along [010] [95, 101]. The b-axis was also almost always the longest growth direction for crystals of the other MnP-type compounds explored in this work. For the sample used in oscillations measurements, the orientation of the a-axis was similarly confirmed with XRD and Laue, making the c-axis the remaining perpendicular direction. Composition was confirmed by EDS as almost exactly 1:1 for samples from different growths. There was no sign of Bi contamination in EDS, XRD, or transport measurements. One drawback of the

[1]Note, however, that axis conventions for this space group have changed over time. In this thesis the convention is always $b < a < c$.

Bi flux growth method is that the small, thin samples are ill-suited for Hall effect or single crystal susceptibility measurements, as they are too light and narrow.

4.3 Transport Results

The temperature-dependent resistivity for single crystal FeAs is shown in Fig. 4.1. The 300 K resistivity value for Bi flux crystals is about 300 $\mu\Omega$ cm, similar to what has been seen previously [95, 101]. The initial increase in ρ as temperature decreases, with a maximum near 150 K, signifies that the measurement is conducted with $\mathbf{I} \parallel b$-axis. A kink at 70 K marks the SDW onset at the same temperature as in other transport, susceptibility, and heat capacity measurements [24, 30, 94, 95]. The inset to Fig. 4.1(a) shows the resistivity plateauing below 20 K at about 2.5 $\mu\Omega$ cm.

With increasing field, magnetoresistance in FeAs evolves from the B^2 dependence expected at low fields to a more linear relation [Fig. 4.1(b)]. This linearity continues without saturation up to 31.5 T. Such a crossover has previously been reported to occur at about 6 T for measurements at 10 K [101]. In Bi flux samples it occurs at roughly 10 T below 1 K with $\mathbf{B} \perp \mathbf{I}$. The other measurements only went to 15 T, but MR was slightly larger over that field range. The data in Fig. 4.1(b) may show the onset of oscillatory behavior just below 30 T, but there were not enough data for possible analysis and no sign of oscillations appeared at other angles, where MR was also smaller.

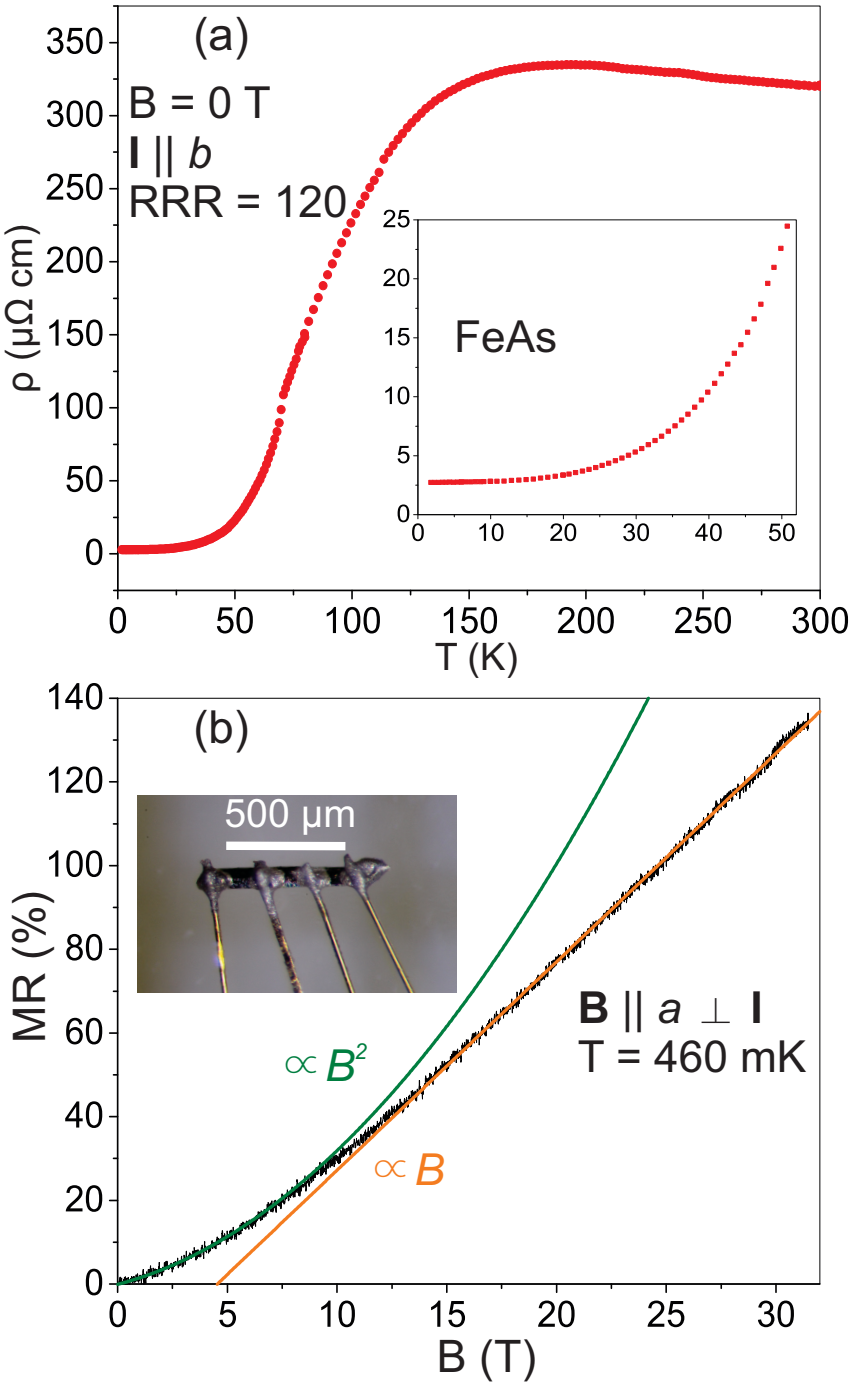

Figure 4.1: (a) Resistivity vs. temperature for an FeAs crystal grown from Bi flux. The high RRR and low residual resistivity (inset) indicate very good crystal quality. (b) Magnetoresistance as a percentage of 0 T resistivity for FeAs up to 31.5 T. Fits of low and high field data to quadratic and linear functions, respectively, show a transition in field dependence of MR around 10 T. Inset: an FeAs crystal wired for longitudinal resistance measurements, showing the needlelike geometry particular to Bi flux growth.

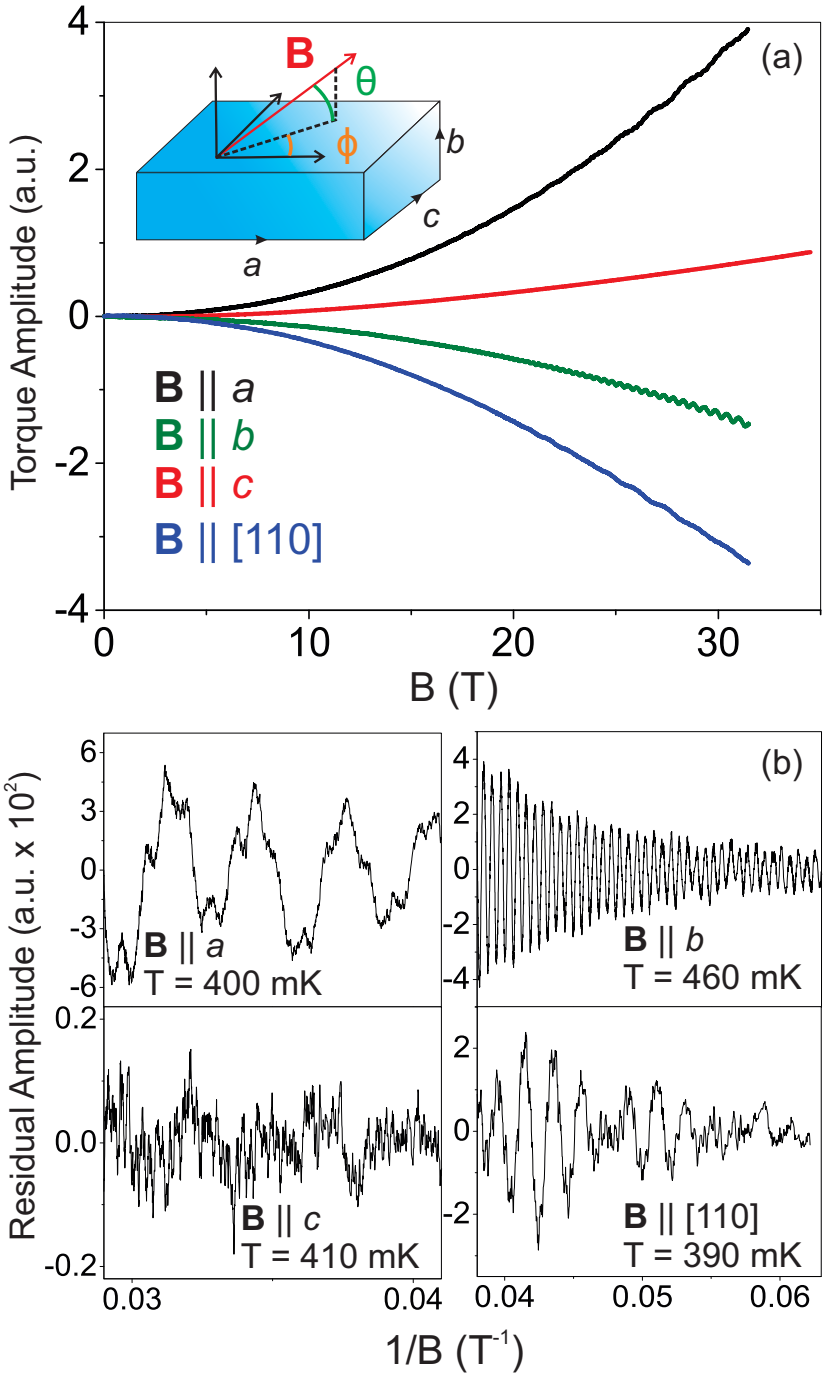

Figure 4.2: (a) Raw torque cantilever data for FeAs for several field orientations. Inset: a schematic showing how field angle was changed in the two measurements on the same sample. Measurements to 31.5 T went from $\mathbf{B} \parallel a$-axis to $\mathbf{B} \parallel b$-axis ($\phi = 0°$, sweeping θ). Those to 35 T went from $\mathbf{B} \parallel a$-axis to $\mathbf{B} \parallel c$-axis ($\theta = 0°$, sweeping ϕ). (b) The residual oscillatory signal of the raw data. Amplitudes are arbitrary but consistent relative to those in (a), and have been enhanced by a factor of 100.

4.4 Quantum Oscillations

As explained in Ch. 3, quantum oscillations arise from the formation of quantized Landau levels in a material in the presence of a magnetic field. Changing the field strength causes these bands to pass through the chemical potential, and the resulting change in occupancy produces an oscillatory signal that can be detected in a wide variety of density of states-dependent quantities [80, 103, 104]. QOs were seen in the magnetic torque measurements of an FeAs single crystal at the NHMFL. Torque data show multiple frequencies across different angles of applied field, as evident in Fig. 4.2(a) which shows the raw torque signal at several field orientations. Oscillatory behavior was clear in the torque signal as low as 10 T at some angles.

Two sets of measurements were made on the same crystal with 31.5 T and 35 T magnet systems as it was rotated in two different planes relative to magnetic field, as illustrated in the schematic in Fig. 4.2(a). Data to 31 T were taken at 24 angles with $\phi = 0°$ and changing θ. In this configuration $\theta = 0°$ signifies $\mathbf{B} \parallel a$-axis and $\theta = 90°$ is $\mathbf{B} \parallel b$-axis. Up to 35 T, 16 measurements were made with θ kept at $0°$ while ϕ was changed, corresponding to $\mathbf{B} \parallel a$-axis at $\phi = 0°$ and $\mathbf{B} \parallel c$-axis at $\phi = 90°$.

To extract the oscillatory component a 3rd order polynomial was subtracted from the raw data; Fig. 4.2(b) shows examples of the presence of different frequencies at different angles, and changes in the amplitude of the residual torque signal. Fast Fourier transforms (FFT) were then performed on the residual data to obtain a frequency spectrum [Figs. 4.3(a) and 4.3(b)].

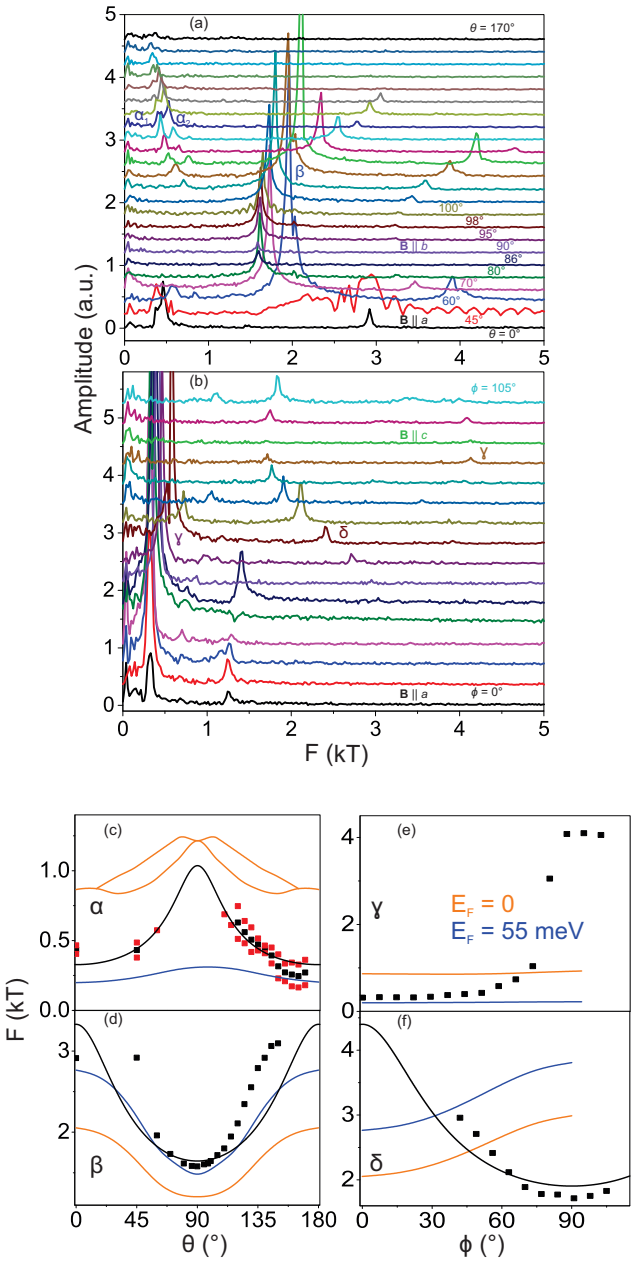

Figure 4.3: FFTs at base temperature (350–550 mK) of oscillatory signals for all angles, offset for clarity. In (a) field goes from parallel to a-axis to parallel to b-axis, in 5° increments at higher angles. In (b) field moves between the a- and c-axes in 7° increments over the entire range. (c)-(f) show observed peaks for each oscillation band as a function of angle as well as theoretically generated frequencies based on AFM Fermi surface calculation of Parker and Mazin [99] (orange line) and the same calculation with E_F raised by 55 meV in work by Limin Wang (blue). Note that that AFM state is not the same as the experimentally observed one. For α, β, and γ fits to an ellipsoidal Fermi surface are also given (black lines). For (c), where peak splitting occurred the average (black) of the α_1 and α_2 frequency peaks (red) was used for the fit.

4.4.1 Angular Dependence

By plotting FFT data for all angles of the two runs as in Figs. 4.3(a) and (b), it is clear that although frequency values change substantially with angle, they can be grouped to one of five extremal Fermi surface orbits. Harmonics of these five frequencies also appear at integer multiples, indicating low scattering as carriers move in their orbits. In the θ scan [Fig. 4.3(a), $\mathbf{B}$ in the ac plane] two low frequencies (denoted α_1 and α_2) around 500 T, and one higher frequency peak near 1500 T (β), were observed. The proximity of the two α_i peaks indicates that they arise from the same Fermi surface pocket, with two slightly displaced extremal orbits. The α_1–α_2 frequency difference was roughly 150 T, independent of temperature or angle.

For the measurement varying ϕ [Fig. 4.3(b), $\mathbf{B}$ in the ab plane] there are two peaks: one with a frequency of about 300 T for angles closer to 0° (γ) and a higher frequency peak with F $\approx$ 2000 T (δ). However, the γ peak diverged to much higher frequencies exceeding δ near $\mathbf{B} \parallel c$-axis with a substantially reduced amplitude. As Fig. 4.3(b) shows, the amplitude decreased substantially as this change occurred. The observation of two main orbits (one of which shows some frequency splitting) in both the a–b and the a–c planes should stem from two distinct Fermi surface pockets. This fits with the theoretical prediction of one unique electron and hole pocket each in the magnetic state [99] as well as experimental evidence suggesting multiple carriers in this regime [40, 95, 101].

4.4.2 Fermi Surface Shape

For an ellipsoidal Fermi surface, the frequency should vary with angle as $F = \frac{F_0}{\sqrt{cos^2\psi + \frac{1}{\epsilon}sin^2\psi}}$, where F_0 is the maximum frequency, ψ the angle and ϵ the eccentricity of the cross sectional ellipse in the plane of rotation [105]. Figs. 3(c), (d), and (f) show fits of peak frequency to this equation for α, β, and δ. At angles with split α_1 and α_2 frequencies, their average value was used for the fit. Divergence from fits makes it clear that the pockets are not perfectly ellipsoidal, however the qualitative agreement shows that α, β, and δ correspond to orbits around three dimensional parts of the Fermi surface with a generally ellipsoidal shape. In contrast, γ shows a slight increase in frequency at lower angles, until roughly $\phi = 70°$ when frequency increases by an order of magnitude before plateauing. This behavior is closer to that of cylindrical or two dimensional pockets, although γ does not fit well to the inverse cosine dependence expected from a perfect cylinder.

Fig. 4.4 shows two theoretical Fermi surfaces for antiferromagnetic FeAs obtained with density functional theory (DFT). Calculations were done for the "AF2" state, calculated by Parker and Mazin to be most favorable at low temperatures [99], in which Fe atoms align antiferromagnetically with both nearest and next-nearest neighbors. This same arrangement was favored in the calculations of Frawley et al. [98], whereas Griffin and Spaldin [100] differed in having a ferromagnetic arrangement of next-nearest neighbors. However, neither of these orderings matches the experimental SDW structure [46]. The top surface in Fig. 4 uses the original AF2 Fermi level, while the bottom one is from the same calculation but with the

Fermi level raised by 55 meV. In both cases, calculations were done by Limin Wang, a postdoc in the Paglione group at UMD. The shift changes the size of the pockets but not their shapes or locations, establishing the robustness of this Fermi surface geometry and therefore also of the expected angular dependence of oscillation frequencies. In either case there is an electron pocket at the central Γ point and four identical hole pockets at $(k_a, k_b, k_c) = (\pm 0.25, \pm 0.3, 0)$. Note that all pockets shown are contained within the first Brillouin zone and would have closed orbits. The non-saturating magnetoresistance may come either from an open orbit not theoretically predicted, or a closed path that saturates at a field larger than 31 T, perhaps due to a low residual resistivity.

Theoretical quantum oscillation frequencies were generated, again by Limin Wang, from the DFT calculations using the Supercell K-space Extremal Area Finder (SKEAF) program [82] are plotted together with the experimental data in Figs. 4.3(c-f). Two bands, one electron-like and one hole-like, were expected for each plane of field rotation, a 1:1 correspondence to what was obtained in measurements. Based on expected frequencies and angular dependence α and γ correspond to hole pocket oscillations, with β and δ belonging to the electron band. As noted, raising the Fermi level does not change the angular dependence, but the accompanying change in pocket size gives closer agreement to the observed oscillation frequencies in most cases. For α and β expected angular dependence matches well to data, and in fact the splitting seen in the hole band is also present in the unshifted Fermi surface calculation in the range $\theta = 30°$–$90°$. This reinforces the roughly ellipsoidal pockets inferred from experimental angular dependence. For γ the divergence at

higher angles does not happen in the theory, and the expected frequency increase is much smaller. For δ a variation of frequency with angle is seen, however the locations of the maximum and minimum oscillation frequencies are reversed. This indicates that the electron pocket area is larger in the k_b–k_c plane than in the k_a–k_b plane, the opposite of the band structure prediction. Overall the DFT Fermi surface appears to give an accurate description of electron and hole pocket shape for field rotated between the a- and b-axes ($\phi = 0°$, changing θ), but not the a- and c-axes ($\theta = 0°$, changing ϕ). k_c corresponds to the propagation direction of the SDW, while the moments lie in the k_a–k_b plane. The fact that this is also the field direction with the strongest divergence from calculation points to a connection between disagreement of DFT and experiment over both magnetic ordering (as was already known) and band structure (as shown here). Oscillations data do, however, support the two carrier picture put forth by other groups [40, 95, 101].

The roughly ellipsoidal Fermi surface makes it acceptable to calculate carrier concentration from frequency values, a process which assumes a circular cross section. Applying (2.21) gives ranges of $2.2 \times 10^{19} - 1.5 \times 10^{21}$ cm^{-3} for the hole pocket and $3.5 - 9.6 \times 10^{20}$ cm^{-3} for the electron pocket, based on maximum and minimum observed frequencies. These are comparable to the values $n_h = 8 \times 10^{18}$ cm^{-3} and $n_e = 1 \times 10^{21}$ cm^{-3} found by Khim et al. [101] through a fit of MR data. The hole pocket has a much more dramatic angular dependence, and for a small range of angles near $\mathbf{B} \parallel c$-axis even exceeds the electron value. Assuming comparable scattering rates, this anisotropy could account for the sign change in R_H at low temperature seen by Segawa and Ando [95] but not Khim et al. [101]

4.4.3 Temperature Dependence

To calculate effective mass via the LK factor (2.22), temperature dependence was taken at three field orientations: $\theta = \phi = 0°$ ($\mathbf{B} \parallel a$-axis), $\phi = 0°$, $\theta = 98°$ (near $\mathbf{B} \parallel c$-axis) and $\phi = 0°$, $\theta = 135°$ ($\mathbf{B} \parallel [110]$). Oscillatory signals for these orientations are shown in Fig. 5.3(b). The second angle gives an idea of the effective mass along the c-axis, but θ was not set to exactly 90° since the torque signal was much reduced directly along the principal axis. Fig. 4.5 gives an example of the clear suppression of FFT amplitude of α_1, α_2, and β with temperature for $\mathbf{B} \parallel [110]$.

Temperature dependent amplitudes for three different field orientations are shown in Fig. 4.5(b-d). Table 4.1 gives the extracted effective masses. With $\mathbf{B} \parallel a$-axis [Fig. 4.5(b)], only the γ hole pocket (F = 315 T) is seen. As with oscillation frequencies, experimental effective masses can be compared to those generated with DFT for the original or 55 meV shifted Fermi level [82]. A fit to (2.22) at this angle gives an effective mass of $3.1m_e$, larger than the theoretical predictions of $1.78m_e$ ($E_F = 0$ eV) and $1.138m_e$ ($E_F = 55$ meV) for the hole pocket in the same orientation. For $\theta = 98°$ [Fig 4.5(c)] only β, at 1.61 kT, appears. Given the absence of any other frequencies, amplitude can be directly extracted from the oscillatory data, and the effective mass is $m^* = 1.2m_e$. For $\theta = 90°$ the predicted electron band masses are $0.668m_e$ and $0.812m_e$ (0 eV) or 0.6322 and $0.940m_e$ (55 meV). At 135° [Fig. 5(d)], β (now at 2.77 kT) survives only up to 1.8 K. Due to the presence of the lower α frequencies in the residual signal, amplitude is taken from the FFT. The LK fit gives $m^* = 3.2m_e$, nearly a factor of three larger than its value at $\theta = 98°$. This again

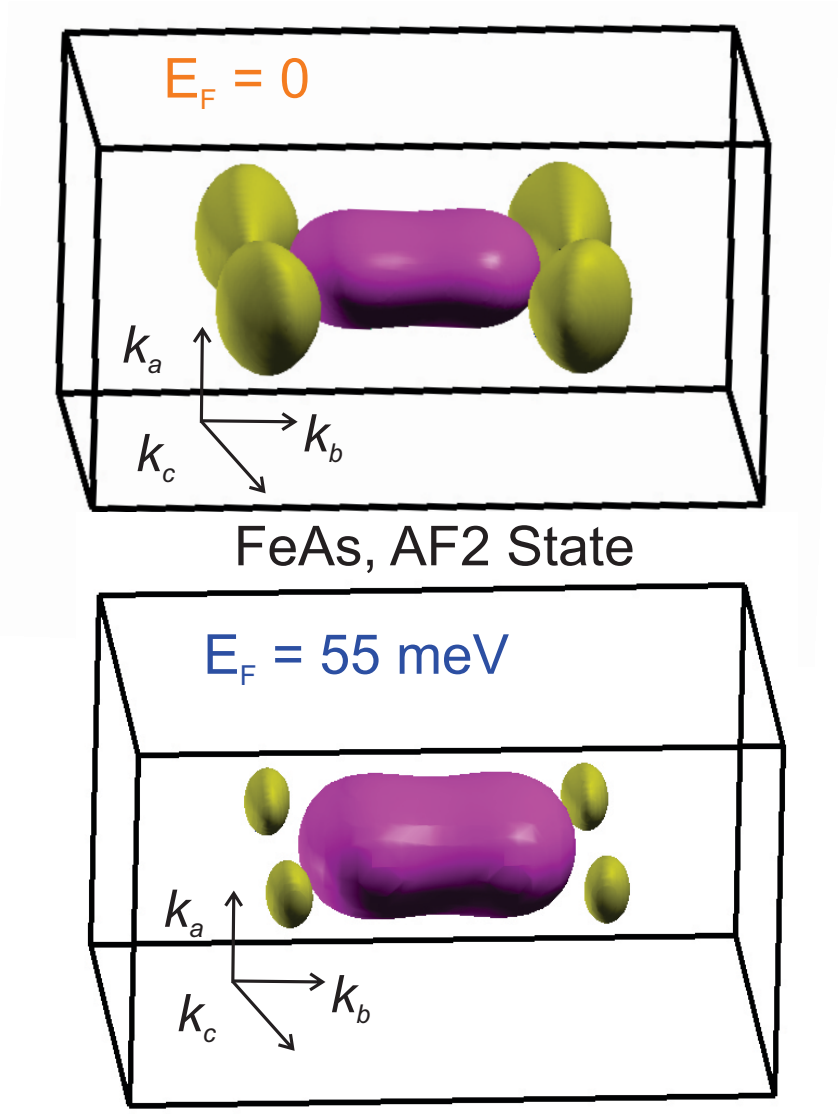

Figure 4.4: DFT calculated Fermi surfaces of FeAs in the predicted "AF2" magnetic state [99], consisting of an electron pocket (pink) at the Γ point and four identical, symmetrically oriented hole pockets (yellow). The bottom has had the Fermi energy raised by 55 meV, which changes the size of the pockets but not their location or general shape.

exceeds predictions of $1.124m_e$ (0 eV) or $1.252m_e$ (55 meV).

At $\theta = 135°$, α_1 and α_2 are found at 412 and 536 T. Using the average value of the amplitude of the two peaks the effective mass comes out to $m_{\alpha,\ ave} = 3.8m_e$. The individual peaks have similar values, further supporting the idea that they arise from the same band. This number is similar to the value of $3.1m_e$ obtained for the same pocket for $\mathbf{B} \parallel a$-axis. The 0 eV Fermi level prediction is for two peaks with masses $1.561m_e$ and $2.023m_e$, while that for 55 meV is one peak of $1.301m_e$. As with all other measured angles, the experimental effective masses are larger than those predicted.

From heat capacity measurements, the Sommerfeld coefficient of the specific heat is 6.65 $\frac{\text{mJ}}{\text{mol K}^2}$ [30]. This can also be calculated from oscillations data using the relation[2]

$$\gamma_{SH} = \frac{\pi k_B^2 N_A}{3E_F} \tag{4.1}$$

The inverse lattice parameters give the in-plane Brillouin zone area (πk_F^2) for each field orientation to calculate E_F. The contribution from each band is then proportional to m^*. The sum of the contributions of each pocket (keeping in mind that there are four hole bands) is $\gamma_{SH} = 7.7$, 16, and 0.29 $\frac{\text{mJ}}{\text{mol K}^2}$ for field along [100], [110], and [001], respectively. The smaller γ_{SH} along [001] indicates that not all the orbits for that orientation may have been observed. However, the average of these three values is 8.0 $\frac{\text{mJ}}{\text{mol K}^2}$, close to the previously reported value. Therefore it seems

[2]The Sommerfeld coefficient is has the subscript "SH" in this chapter, standing for "specific heat", to distinguish it from the γ oscillation band. In all other parts of this thesis it is simply γ.

unlikely that there is a significant missing contribution to the density of states at E_F that would solve the theory-experiment discrepancy. Instead, the enhanced effective masses make it probable that there are electron correlations in FeAs unaccounted for by DFT. It has recently been proposed that spin-orbit coupling may have significant influence on the FeAs band structure in the magnetic state [98]. Although this correction is not normally included in calculations for Fe-based compounds, it (or other effects) may account for some of the observed disagreement.

4.4.4 Dingle Temperature and Scattering

The Dingle factor in the oscillation amplitude is given by (2.23), and the Dingle temperature is proportional to the scattering rate Γ (2.24). By approximating a circular Fermi surface again, it is then possible to extract the mean free path (2.25). Since the Fermi surfaces seem to be ellipsoidal, the mean free path values extracted from T_D allow for a reasonable comparison but are not meant to be exact. T_D was calculated based on fits of peaks in the decaying "envelope" of the residual signal as a function of inverse field [Fig. 4.5(e-g)] and are listed in Table 4.1 along with estimates of ℓ. For α_{ave} the average frequency of α_1 and α_2 (474 T) was used. It is only possible to solve for T_D if the effective mass is known, limiting the analysis to only the three angles for which temperature dependent measurements were made. Additionally, since calculation of T_D relies on a clear exponential decay of amplitude it is typically necessary to have one dominant peak at a specific angle to extract a Dingle temperature. For that reason it is not possible to calculate T_D for each

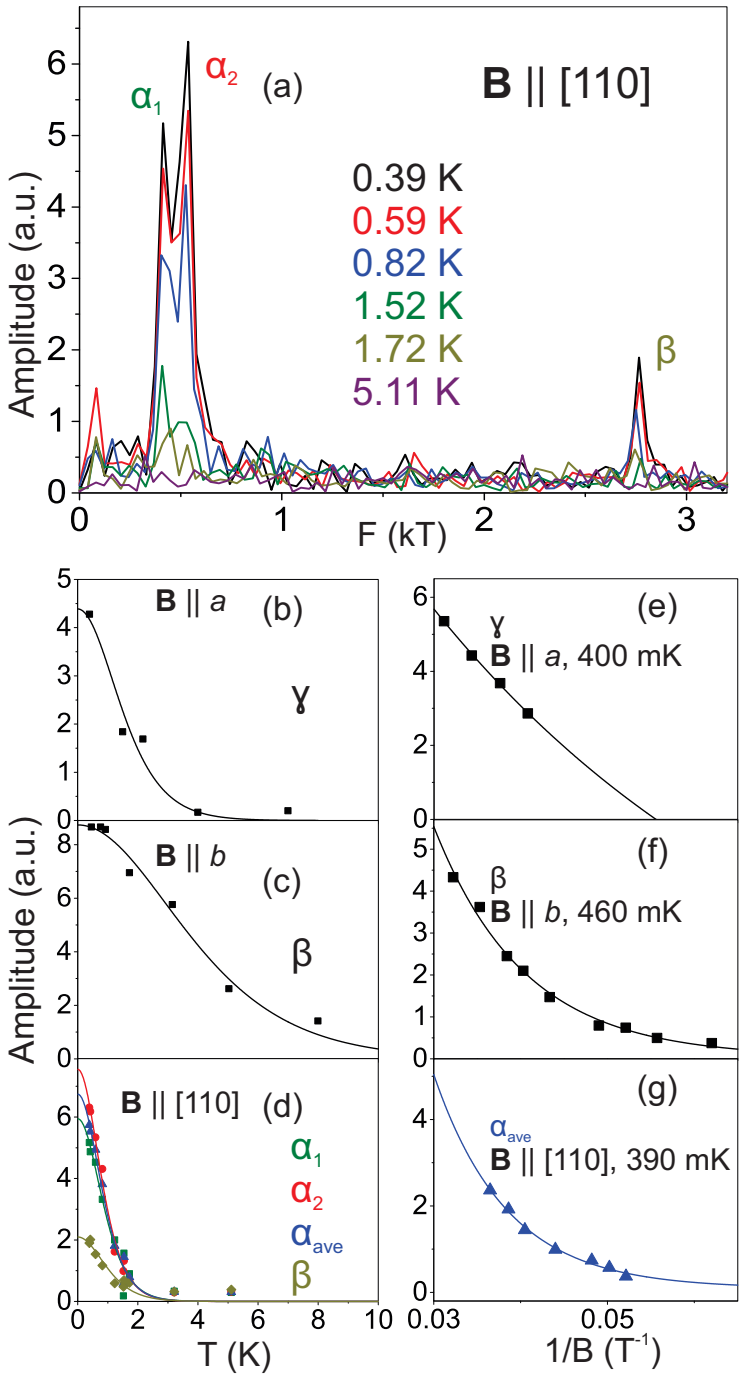

Figure 4.5: (a) FFTs at multiple temperatures for **B** ∥ [110], showing the decrease in amplitude with temperature of the α (500 T) and β (2800 T) peaks. (b-d) Fits to the LK factor at different field angles. Plots of peak amplitudes vs. inverse field at base temperature were fit to a decaying exponential to extract the Dingle temperature (e-g). Base temperature varied slightly between measurements. Due to its small amplitude relative to α_1 and α_2, it was not possible to extract T_D for β at **B** ∥ [110].

peak at each angle. This is not an issue for $\mathbf{B} \parallel c$-axis, where only β appears and $T_D = 5.5$ K. However, due to their very similar frequencies it is hard to separate α_1 and α_2, and so the best that can be done is to give $T_D = 2.2$ K as the average value for the α oscillation at $\theta = 135°$. The β oscillation is only a small modulation of the signal for this orientation [Fig. 4.2(c)]. Again there is anisotropy in the hole pocket, as T_D goes from 2.2 K to 5.1 K as field moves from [110] to the a-axis. A change in scattering with orientation is not surprising given the previously noted differences in both the longitudinal and Hall resistance for measurements along different crystal axes [95].

The Dingle temperatures of FeAs are similar to those seen in $BaFe_2As_2$. In that material T_D can be calculated for two out of three observed bands, and for both is in the range 3—4 K [106]. In another 122 material, KFe_2As_2, T_D is between 0.1—0.2 K for five different pockets [107]. For the K compound, RRR values up to 2000 are possible [108], while for $BaFe_2As_2$ RRR less than 10 is typical [109], though it can be raised to nearly 40 with annealing [110]. FeAs seems to resemble $BaFe_2As_2$ much more than an exceptionally "clean" material like KFe_2As_2.

4.5 FeAs: Conclusions

Bi flux growth results in higher quality FeAs crystals than previous attempts with Sn flux or I_2 CVT. This improvement makes it possible to observe quantum oscillations in magnetic torque at high fields. Measurements in two different planes reveal five unique peaks, corresponding to one electron and one hole band in each

Orbit	Type	**B** ∥ [hkl]	F (T)	m^*/m_e	T_D (K)
α_1	h	[110]	412	3.6	—
α_2	h	[110]	536	3.9	—
α_{ave}	h	[110]	—	3.8	2.2
γ	h	[100]	316	3.1	5.1
β	e	[110]	2765	3.2	—
β	e	[001]	1615	1.2	5.5

Table 4.1: Parameters extracted from fits of FeAs quantum oscillation amplitude to the LK and Dingle factors at several field orientations.

direction (with the hole band split for field in the *ac* plane). These peaks can be indexed using a DFT-calculated Fermi surface for antiferromagnetic FeAs [99]. Three peaks near 500 T (split peaks α_1 and α_2 and γ) stem from extremal orbits around the predicted four identical hole pockets, and two others (β and δ, one in each plane) near 2 kT come from the electron pocket at the Γ point. The γ oscillation band has a two dimensional shape and cannot be easily assigned a simple geometry. The other three observed oscillations show a three dimensional, qualitatively ellipsoidal angular dependence, as expected from calculations, with slight disagreement in pocket size. Comparison of the specific heat coefficient γ_{SH} seems to indicate that there is not a significant missing contribution.

The observation of two distinct frequencies overall validates the multiband notion of transport in the low temperature SDW state indicated by previous experiment [40,95,101]. There is good agreement with the calculated Fermi surface when field is swept in the *ac* plane, but disagreement for *ab* plane rotation. Most notable is a significant increase in the cross sectional area of the hole pocket near the k_a–k_c plane, where it becomes larger than the electron pocket. Extracted effective masses

for both hole and electron pockets are larger than predicted by calculations, indicating that the degree of electron correlations is greater than theoretical expectations. It was already known DFT results did not match the magnetic state of FeAs. This study makes it clear that the band structure is on the right track, but still awaits a full theoretical description.

Chapter 5: A Magnetoresistance Study of FeP

5.1 Introduction

A bit surprisingly, given its composition, FeP may actually have more in common with MnP and CrAs than FeAs. Its magnetic structure is better described as helimagnetic [29], rather than a spin density wave. The two moments rotate in plane while propagating along the c-axis, rather than changing their amplitude but pointing in the same direction, as in FeAs [46]. The 120 K Néel temperature is also a bit higher than 70 K in FeAs, where for CrAs it is about 260 K in CrAs and the initial PM-FM transition in MnP is at about 290 K [21]. Crystal growth and transport properties also differ between the two materials. FeP cannot be grown from flux, and has a much higher RRR and MR than FeAs. The change in the pnictogen atom clearly makes a big difference. It may be that the volatility of phosphorus generates vacancies that change the Fermi level or contibute to magnetism, as can be the case in transition metal dichalcogenides with deficiencies on the chalcogen site [6]. Or the change in spin orbit coupling, since the mass of P is less than half of that of As, can be the driver.

This chapter will present transport measurements of FeP single crystals at ^{3}He temperatures in magnetic fields up to 35 T. The focus of the high field measurements

in this case is not on quantum oscillations, as a thorough study of that has already been done [111]. Instead the interesting result is the very large, nonsaturating magnetoresistance in all directions, which can be enhanced several hundred times over its zero field value. This is similar to the behavior seen in sibling compound CrP as well as the 1:1 rare earth-pnictide binaries [56,112,113], which form in a different (cubic) structure. It can be attributed to a nearly compensated Fermi surface and the change in carrier mobility with temperature. Most interestingly, MR is linear when field is applied along the *c*-axis, which also when it has its minimum high field value and Shubnikov-de Haas oscillations vanish. While such behavior is similar to the quasilinear MR seen in CrAs near the 0 K helimagnetic-superconducting phase diagram boundary [19], in FeP this comes at ambient pressure. The likely explanation for LMR is quantum Abrikosov MR, in which conduction arises from a single Fermi surface pocket [78]. The observation in LMR in a magnetic, good metal stands as a contrast to the XMR seen in CrP and the rare earth-pnictide binaries. Temperature dependence shows that there is a "turn on" temperature to the MR that can be attributed to high sample mobility. Angle sweeps at fixed field indicate the complex nature of the Fermi surface as noted in previous quantum oscillations work [111].

5.2 Methods and Characterization

CVT growth of FeP single crystals with I_2 is well-established [31,85,111,114, 115]. The procedure was unchanged from other materials, with a hot zone temper-

ature of 850 °C. Single crystals of FeP were found at the cold end of the furnace after 10-14 days, but on occasion some would also be found at the hot end, indicating that the reaction did not strictly follow the thermodynamics determined by the temperature gradient.

Powder x-ray diffraction (XRD) measurements of the resultant crystals showed single phase FeP with lattice parameters of $a = 5.10$ Å, $b = 3.10$ Å, and $c = 5.79$ Å, in line with previous reports [27, 111]. Of note is that FeP has the shortest b-axis of all the 1:1 transition metal pnictides, with only CoP having shorter a- and c-axes. Energy dispersive x-ray spectroscopy of single crystals consistently showed a composition of 55% Fe, 45% P, slightly off stoichiometry. Attempts at CVT growth were also made using prereacted FeP powder. However, samples grown from powder had lower residual resistivity values, suggestive of lower crystal quality. Interestingly, EDS measurements on these crystals showed 50:50 Fe:P ratio. Phosphorus vacancies, or iron self-doping enhance the conducting properties of this material, perhaps by changing impurity concentration, carrier density, or the position of the Fermi level. Such behavior has been seen in both $TiSe_2$ and Bi_2Se_3, where changes in Se vacancy level significantly impact carrier concentration (obtained from Hall measurements) and temperature-dependent resistivity [6, 116]. DFT predictions have shown that the Fermi surface in MnP-type compounds can be restructured with small changes in electron count [32]. A slight increase in this number may result in a significant increase in carrier density or Fermi pocket size.

Attempts to grow single crystals were also made using Bi, Sn, Pb, and Sb as fluxes. Only Sb produced crystals, but they were small and showed traces of

residual flux in transport measurements. Growth temperature and the purity of starting material also had a significant effect on both residual resistivity and the magnitude of MR. The crystals grown with CVT were large and often polyhedral, but nevertheless showed a clear preference for growing along the b-axis, the shortest principle axis.

The zero-field transport behavior of FeP looks qualitatively like to that of FeAs [Fig. 5.1], with similar values of ρ(300 K) and a plateau in resistivity below 20-30 K. One difference is that FeP never has an increase in ρ with the initial cooling from room temperature. The most obvious transport feature is a 120 K kink marking the onset of helimagnetism [Fig. 5.1, inset]. Residual resistivity is very small, as low as 0.2 $\mu\Omega$ cm in some samples. The residual resistivity ratio (RRR), defined as ρ(300 K)/ρ(1.8 K), can be over 1500, indicative of very good crystal quality. This is similar to the highest values attained for MnP [117] and higher than the 400-500 seen in the Cr-based B31 materials [18, 112]. This is again a difference from FeAs, where even the best quality Bi flux samples had RRRs that were about an order of magnitude lower.

5.3 Magnetoresistance

5.3.1 Field Dependence

Field sweeps were made at various angles and temperatures for multiple samples at the NHMFL. The first, called S1 [Fig.5.2(a)], was aligned with two different [101] reflections perpendicular to current. However, angles as listed in figures have

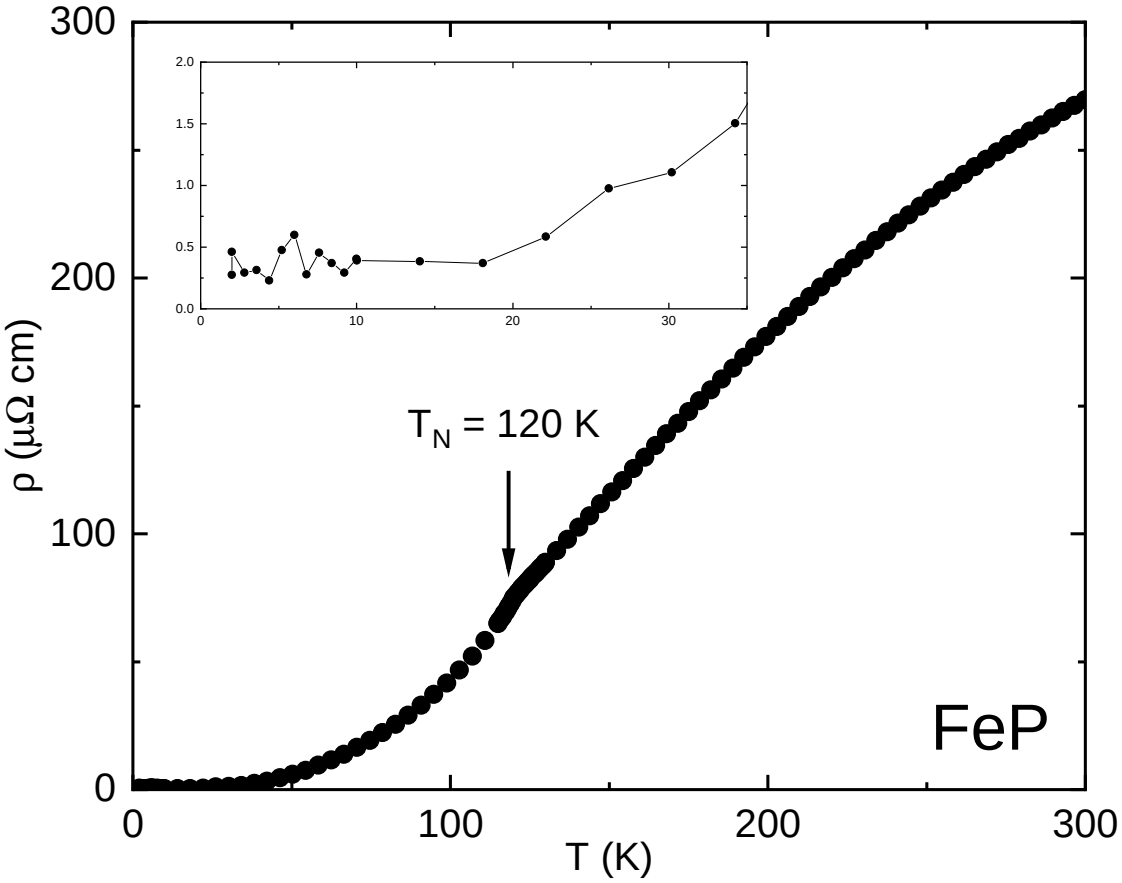

Figure 5.1: Resistivity (at 0 T) as a function of temperature for an FeP crystal with a RRR of approximately 1000. It is generally similar to that of FeAs, with a feature at 120 K denoting the Néel temperature. The inset is of low temperature data, showing the plateau below about 30 K. The variation in the lowest temperature data is due to the resistance being close to the noise floor of the PPMS.

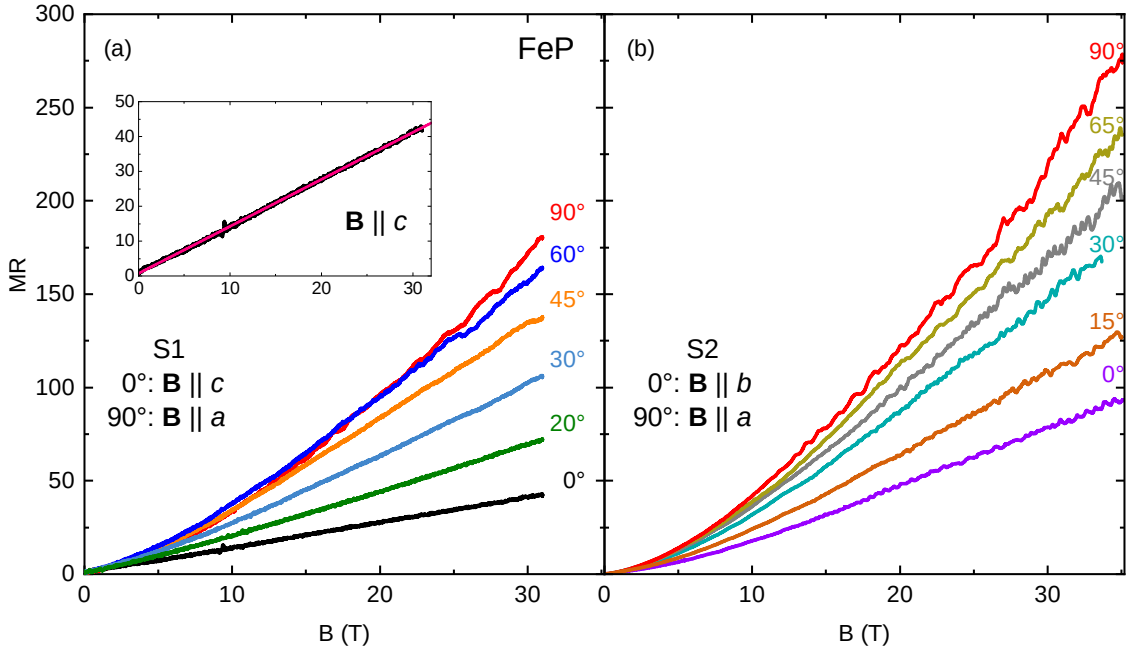

Figure 5.2: High DC field transverse magnetoresistance at several angles for FeP crystals S1 (a) and S2 (b), which had different orientations. The temperature was about 400 ± 50 mK for all measurements, but the variation should not have an impact on the data in this region. The inset to (a) is a closeup of the $\mathbf{B} \parallel c$-axis data, with a linear fit (pink) over the entire data range. Note that MR for the common $\mathbf{B} \parallel a$-axis orientation is larger for S2, which can be linked to its higher RRR value. S1 was actually oriented along two different [101] crystal directions, but data were shifted by a constant angle here for simplicity.

been shifted so that 0° corresponds to $\mathbf{B} \parallel c$-axis and 90° was $\mathbf{B} \parallel a$-axis for simplicity. For the second, S2 [Fig. 5.2(b)], the same angles were $\mathbf{B} \parallel b$-axis and $\mathbf{B} \parallel a$-axis, respectively. In both cases field was always applied perpendicular to current. The RRR was about 1300 for S1 and 1400 for S2. Measurements on a third sample (not shown) found the expected suppression of magnetoresistance accompanying a decreasing Lorentz force as field was rotated into the same direction as the current.

Both S1 and S2 show nonsaturating magnetoresistance at all angles, and often quantum oscillations. The Shubnikov-de Haas oscillations do not show all the known oscillation bands [111], particularly those at high frequency, but this can be explained by the decreased resolution of electrical transport compared to the magnetic measurements in the reference. For both crystals, the maximum MR is when $\mathbf{B} \parallel [100]$. The larger MR of S2 can be connected to its higher RRR, as the two are often highly correlated in large MR metals [58, 118]. Most angles show similar behavior, with an initial quadratic dependence that becomes more linear at high applied field, like what was seen in FeAs [Fig. 4.1(b)].

The curve for $\mathbf{B} \parallel c$-axis stands out for several reasons. Foremost of all, it is strikingly linear from very low fields, with a sublinear deviation only barely noticeable below 0.5 T. This orientation also results in the lowest MR of any of the angles measured in either rotation plane, though the increase is still about 40 times by 31 T. Furthermore, in the vicinity of this angle there are no quantum oscillations. This could be attributed to the presence only a single small Fermi surface pocket, and condensation of all carriers into the lowest Landau level at very low fields [78], a notion that will be expanded upon in the Discussion.

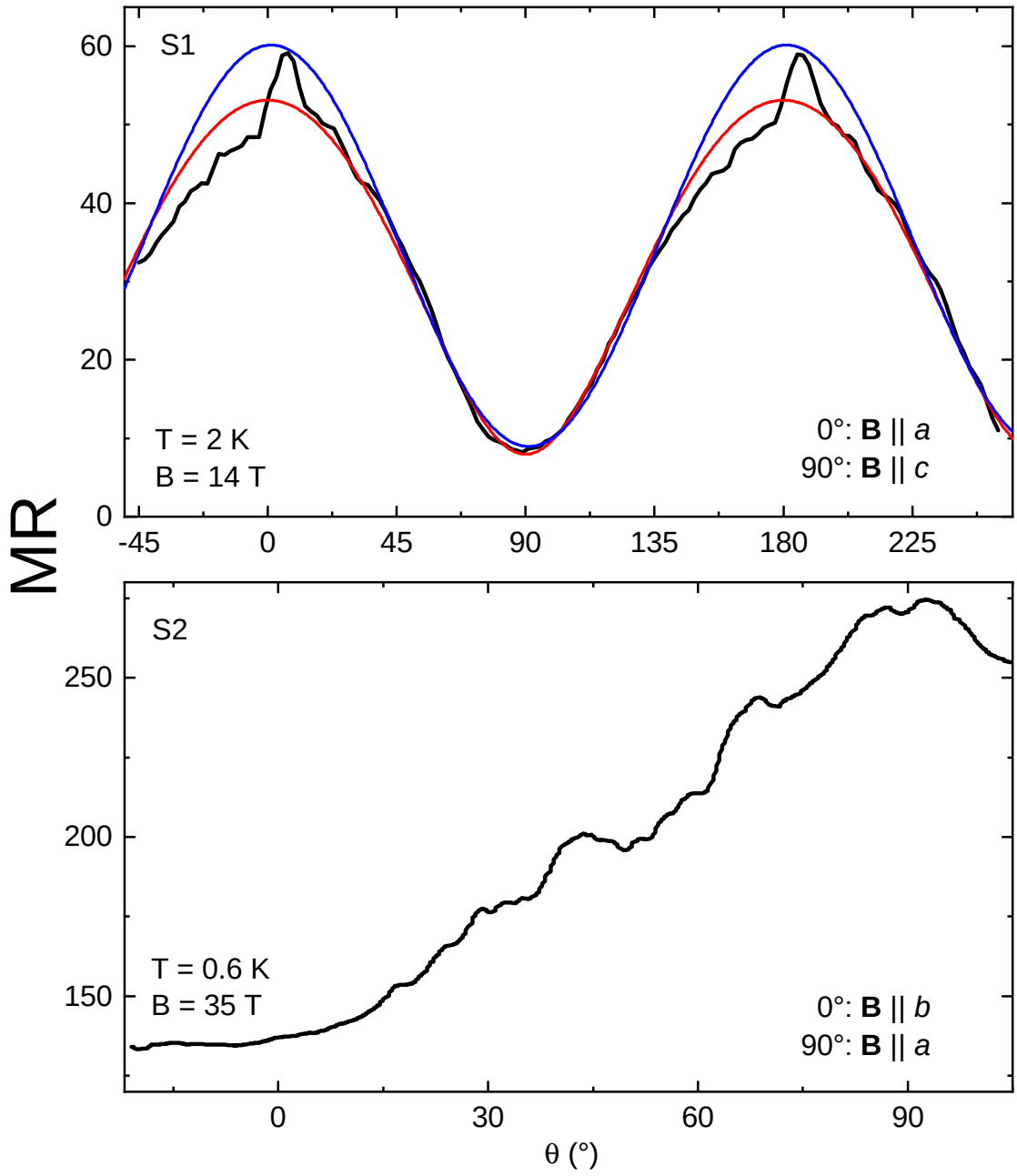

Figure 5.3: Angle-dependent magnetoresistance for FeP samples (a) S1 and (b) S2 from Fig. 5.2 at 14 T and 35 T, respectively. Angular magnetoresistance oscillations are clearer in the higher field, lower temperature data. Data in figure have two fits, the blue line is a fit to a simple 2D Fermi Surface, MR $\propto \cos\theta$. The red line is two an anistropic 3D Fermi surface, MR $\propto (cos^2\theta + \gamma^{-2}sin^2\theta)^{\frac{1}{2}}$, where γ is the ratio of effective masses. The peak just off of the a-axis was excluded from fitting.

5.3.2 Angular Dependence

Resistance was also measured at constant field and temperature while rotating the crystals in 14 T and 35 T fields [Fig. 5.3]. There are many detailed features in the angle dependence even between the principal axes, which are especially obvious with higher field and lower temperature. Such features are known as angular magnetoresistance oscillations, and are clear indicators of an anisotropic Fermi surface structure. MnP, which also has a large MR, has shown a similarly complex structure when rotated in field [119]. It is difficult, however, to extract anything more quantitative from these oscillations. Most notable, however, is that the maximum in MR comes about 5° off of the a-axis at 14 T. This could perhaps be attributed to a slight error in the rotator, but there is an obvious underlying sinusoidal dependence centered on crystal axes that is different from the asymmetric MR peak.

This periodicity can be fit to two different models to determine the dimensionality of the Fermi surface. The two dimensional model [blue line in Fig. 5.3(a)] is simply a cosine. The three dimensional model [red line in Fig. 5.3(a)] accounts for the anisotropy of the effective mass in the planes perpendicular to the field at the peak and valley of MR, denoted γ, and has the overall form $(\cos^2\theta + \gamma^{-2}\sin^2\theta)^{\frac{1}{2}}$. The peak located about 5° away from 0° and 180° was excluded from the fitting. It can be seen that neither model is an especially good fit to the real curve, even ignoring the peak. This indicates that neither the simplest, two dimensional model, nor a three dimensional, slightly more elaborate ellipsoidal picture, account for the angular dependence. Like with FeAs, there is perhaps a generally ellipsoidal form

to the pockets, but nevertheless their shapes are more complicated than that.

5.3.3 Temperature Dependence

Field sweeps at various temperatures and temperature sweeps in constant field were made for specific angles up to 14 T at UMD. The temperature sweeps show a similar behavior to that seen in CrP and several extreme MR rare-earth pnictide binaries, with a "turn on" temperature, T*, below which magnetoresistance increases significantly [58, 112]. Figure 5.4 shows the data for the angle with maximum MR, about 75° in Fig. 5.3(a), near $\mathbf{B} \parallel a$. At and above 5 T, this actually leads to an increasing resistance with decreasing temperature. Judging by the minimum of the 14 T temperature sweep, T* $\approx$ 35 K. This temperature is in the same 30-50 K range seen in the previously mentioned materials. However, one feature unique to FeP is that resistance does not saturate below T* at high enough fields. In fact, for B = 14 T the increase in resistivity below 25 T, after subtraction of the zero field temperature dependence, fits well to a straight line with a slope of about 0.5 $\frac{\mu\Omega\ \mathrm{cm}}{\mathrm{K}}$. The zero field resistivity was also practically temperature independent below 30 K. A power law fit of the form $\rho = \mathrm{A} + \mathrm{BT}^n$ gives a good fit when $n = 3.6$ for data between 2 K and 60 K. This is similar to the the value of the value $n = 3$ found for CrAs [120], indicating that that neither electron-phonon ($n = 5$) or electron-electron ($n = 2$) scattering dominate in the low temperature regime.

The continued increase in resistance in field down to lowest temperatures is quite distinct from the compensated rare earth pnictides, where the increase below

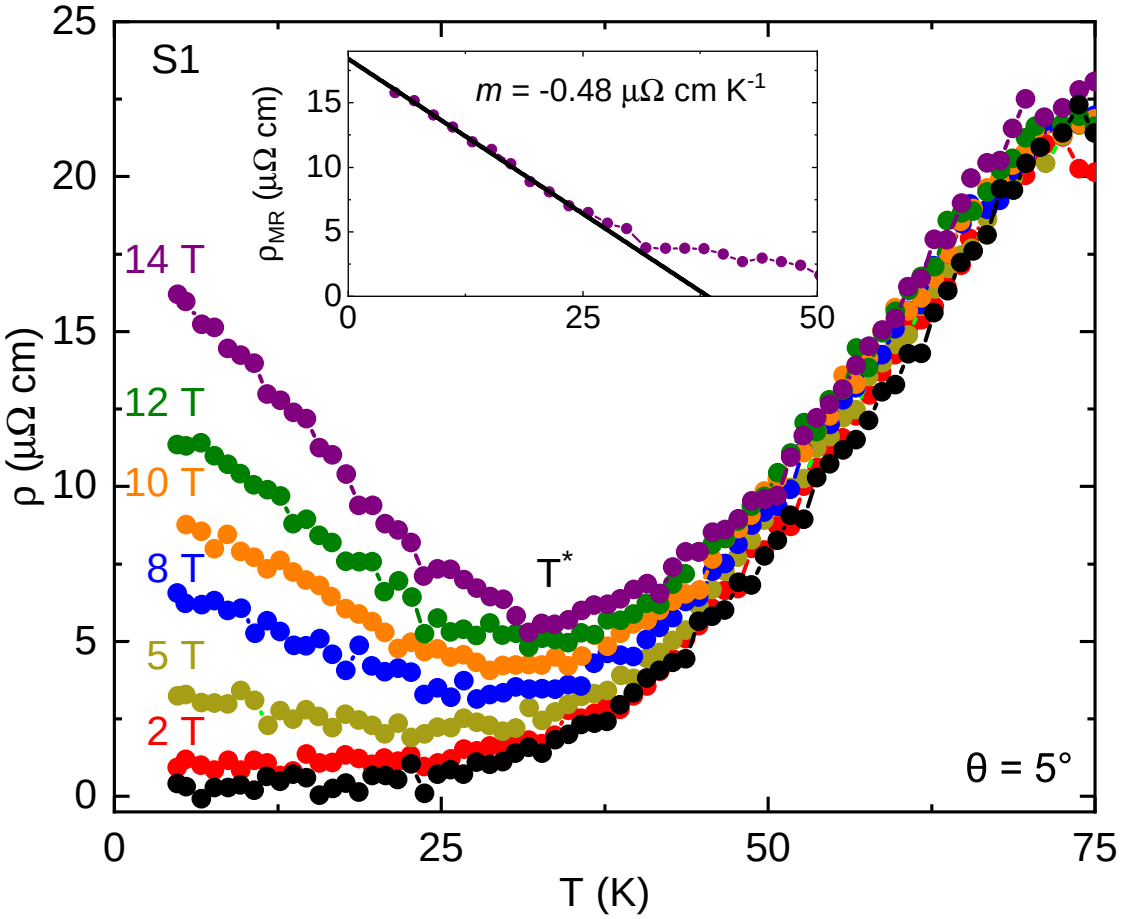

Figure 5.4: Temperature dependence of the resistivity of FeP sample S1 at the maximal magnetoresistive angle in the a-c plane from Fig. 5.3(a), $\theta = 5°$. The black points are at 0 T, the colored and labeled points in applied field. The inset shows the difference between the 14 T and 0 T data, or the "magnetoresistive ρ", with a linear fit to the data below 25 K and the obtained slope.

T^* promptly gives way to a plateau [113]. Instead, in FeP even for fields 5 T or below the resistance continues to increase down to 1.8 K. In this region the zero field resistance has plateaued, indicating that the MR is no longer simply a function of ρ_0 and thus violates Kohler's rule [121, 122]. This means that a different scattering process has emerged below T*, that must generate the sinusoidal anisotropy of the MR and the anomalies seen at unexpected angles.

5.4 Hall Effect

Hall effect measurements can also help to illuminate the changes in FeP with temperature, field, and orientation. The Hall resistance was measured for three high RRR samples with different orientations [Fig. 5.5(a)], two of which were shown in Figs. 5.2 and 5.3: **B** ∥ [101] (S1), [010] (S2), and [001] (S3). The Hall coefficient R_H was extracted by antisymmetrizing ±14 T field sweeps. It is known from QO work that there are various Fermi surface pockets in this material [111] and thus likely both electrons and holes. Still, the value of R_H was negative for all orientations both above and below T_N. There is, however, a noticeable temperature dependence, with $|R_H|$ maxima in the **B** ∥ [001] and [101] samples in the vicinity of T_N, and $|R_H|$ minima in all three samples at lower temperatures between 25-75 K. Sample S1 (**B** ∥ [101]) showed slight nonlinearity below 50 K [Fig. 5.5(b)], but the other two were linear in field over the entire temperature range. The two-band model (2.16) can be used to extract the Hall coefficient of the nonlinear data. The only way for ρ_{xy} to be nonlinear in that model is if the B^2 term is nonzero. Thus, $(p-n)$ must be

nonzero, and the material cannot be perfectly compensated. This single equation has three unknowns, so some assumptions must be made. From the higher temperature R_H values it is possible to estimate $n = 5 \times 10^{21}$ cm^{-3}. A value of 2.5×10^{21} cm^{-3}, slightly less than n, is chosen for p. This is because the two carrier densities must be somewhat comparable to result in a nonlinear slope, and the negative R_H is a sign that electrons are always the more abundant carrier. It was found that values of 1-4 $\times 10^{21}$ cm^{-3} give equally good fits, indicating that the fit is robust to moderate variation in p. Thus it is the ratio of the mobilities is more relevant, and can be solved for. μ_n is always larger, unsurprising given the consistently negative R_H. But μ_n/μ_p drops dramatically from 50 K to 2 K with values that are also robust to the choice of p [Fig. 5.5(b), inset]; the hole mobility is becoming increasingly comparable to the electron mobility. A significant temperature dependence of the carrier mobilities is unsurprising when a material has a low resistivity [112,121,122].

The beginning of nonlinearity in the Hall effect is about the same temperature at which MR becomes appreciable in longitudinal resistance. The increasing presence of the hole band, due primarily to a change in mobility rather than carrier density, is then likely a source for the large magnetoresistance as well. This is also the case for WTe_2 and the cubic rare earth pnictides [53,113]. However, the change in those materials is much more extreme, and ρ_{xy} actually changes sign at high field. Even at 2 K in FeP, electrons are still eight times more mobile than holes, and the nonlinearity of the Hall resistivity is much more subtle and only observed for one of three measured orientations. The negative R_H at all orientations and temperatures is proof that electron transport is still dominant in FeP. It is not as well compen-

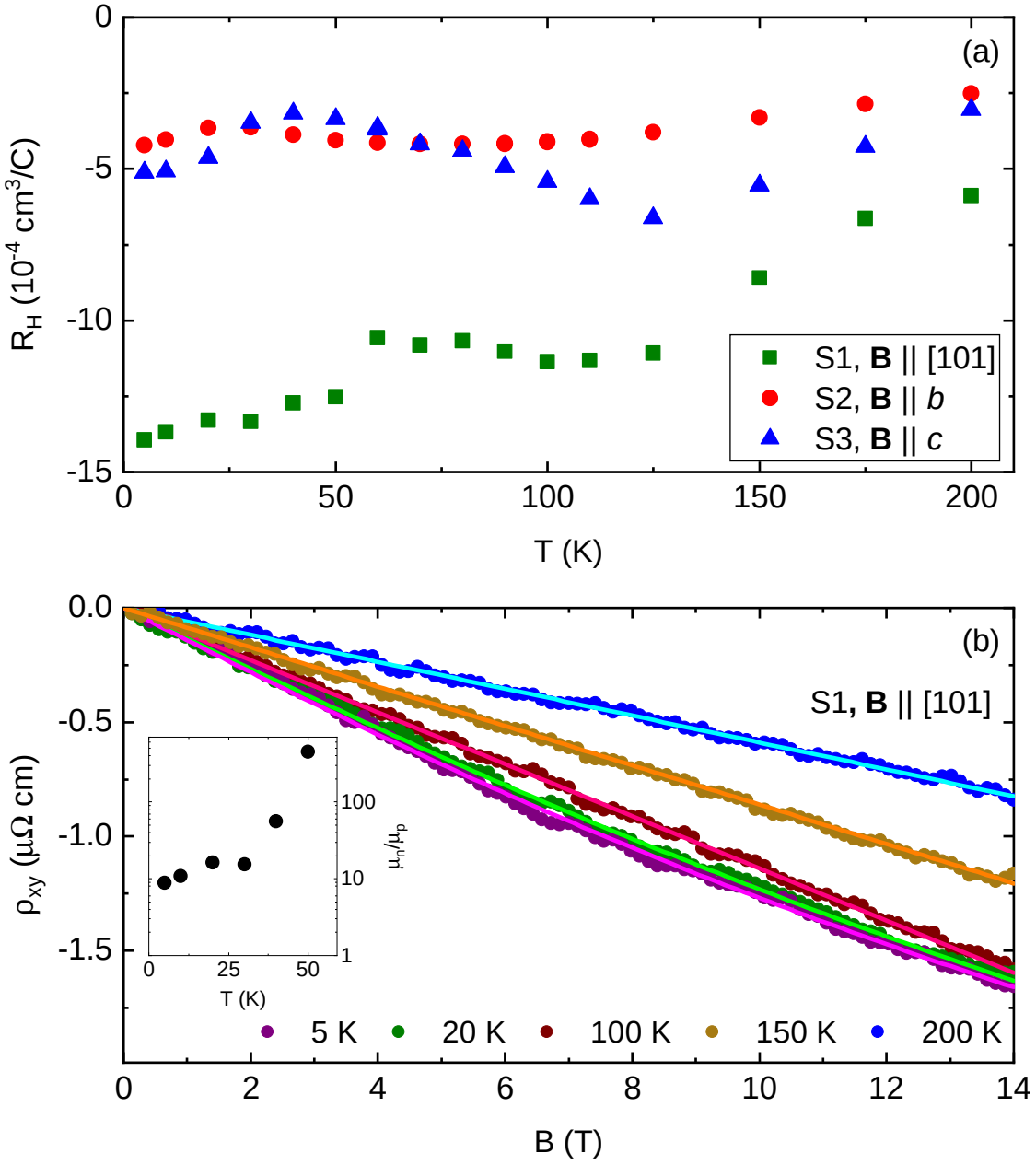

Figure 5.5: (a) The Hall coefficient as a function of temperature for field along three different crystal orientations. (b) Hall resistivity from antisymmetrization of ±14 T field sweeps for **B** ∥ [101] at representative temperatures. Solid lines are fits to the data, and which become nonlinear below 50 K. The inset shows μ_n/μ_p, the ratio of the electron to hole carrier mobility obtained from (2.16), at low temperatures where ρ_{xy} is no longer linear. The slight oscillations visible in the data are an artifact from ansymmetrization.

sated as the previously mentioned materials, or classic examples like Bi [52], but the electron and hole concentrations are close enough that it can lead to large, non-saturating MR when the mobilities are also comparable. This, along with carrier concentrations an order of magnitude larger, may be why the MR, while sizeable, does not reach the values of 10^5 or more seen with other compounds at similar field and temperature [56, 58, 113].

5.5 Discussion

The magnetotransport of FeP is interesting for two separate reasons: because it is large with clear orientation dependence, and because it is linear for $\mathbf{B} \parallel c$-axis. Focusing initially on the former, there are as mentioned various generators of large MR. Somewhat unique to its observation here is that FeP is antiferromagnetically ordered and a very good metal. The latter, along with the strong anisotropy of MR magnitude, rules out disorder. Samples with small amounts ($< 10\%$) of Co doping on the FeP site have a magnetoresistance of less than 5% at 10 T with a more quadratic field dependence. This is substantially lower even than FeP samples with similarly low RRR values, another sign that disorder is actually antagonistic to large MR. Rather the low residual resistivity is benificial, as it increases $\omega_c\tau$. Large MR has been found in isostructural MnP [119] and CrP [112], though the highest field reached in those studies was just 8 T and 14 T, respectively. This result seems to indicate that magnetic ordering is not a significant factor in producing large MR, since CrP is paramagnetic and MnP passes through several different stages

of magnetic ordering with field at low temperature [21]. FeP and MnP can also be contrasted with FeAs and CrAs, which have similar magnetic structures [29] but MR merely on the scale of sample resistivity at 14 T [13,19]. There is also no significant magnetoresistance in the vicinity of T_N, indicating little change in scattering when going from strong magnetic fluctuations to an ordered state.

Instead, electron-hole compensation is the most likely explanation, with semimetallic bismuth being the classic example [52]; more recently nearly perfect compensation has been pertinent to the family of rare earth-pnictide 1:1 binaries [56, 123, 124] as well as CrP. Compensated or nearly compensated materials also should see MR saturation either only at very high fields or not at all, and up to 35 T MR does not saturate in any direction for FeP. Additionally, from Hall effect measurements conduction is electron-dominated at all temperature and alignments. For comparison, FeAs has multiple changes in carrier sign [95] but has a much smaller MR [13, 101]. However, quantum oscillations clearly show the contribution from multiple Fermi surface pockets [111], some of which surely come from hole bands. It cannot be a coincidence that nonlinearity in the Hall effect at one orientation comes near the "turn on" temperature [58, 112]. Compensation explains the independence of MR from magnetic order, as its size depends primarily on the different in hole and electron carrier density, which is a product of the band structure. Slight differences in dispersion or shifts of the Fermi energy for different elements would tweak the degree of MR.

The angle-dependent linear magnetoresistance is an even more intriguing result. Such behavior has been observed in the Fe-pnictide superconductors, where

theory attributes it to the changes that occur in the Fermi surface as those materials enter the spin density wave regime [125]. The field at which magnetoresistance crosses from a quadratic to linear dependence is proportional to the SDW gap and the scattering rate. A typical value for the parent pnictides was estimated to be 2 T. The relatively high 120 K transition temperature, large RRR, and low Dingle temperatures seen in FeP would all contribute to a similarly low crossover field. The slightly lower T_N and RRR in FeAs then fit with its quadratic-linear crossover at 5 T [Fig. 4.1].

There are also parallels to observations in CrAs under pressure. With the application of about 1 GPa, superconductivity with $T_c = 2$ K emerges [18, 34] as T_N decreases. Near the critical pressure for competition between magnetism and superconductivity, the magnetoresistance becomes increasingly linear [19]. This is attributed to non-Fermi liquid physics arising at a quantum critical point. However, quantum criticality is associated with linear scaling of resistance with both field and temperature [75]. Under pressure CrAs has a T^2 dependence just above T_c [34], and for FeP resistivity is similarly never linear. This suggests that the binary pnictides are not quantum critical materials. This was already suspected for CrAs due to the first order nature of its magnetic transition, which is accompanied by a large magnetostriction [44]. But despite not following typical quantum critical physics, there is still evidence of unconventional superconductivity in CrAs that is often linked to the presence of magnetic fluctuations [44, 120]. So it is still of interest to look at the effect of pressure on FeP, which may also become a superconductor, perhaps at lower pressure due to its lower T_N.

The mostly likely potential source of LMR is the Abrikosov quantum picture [78]. In this scenario, conduction comes from a single Fermi surface pocket, for which above a certain field strength all the carriers will be in the lowest Landau level. If this pocket has a (Dirac-like) linear dispersion, then there will be a linear scaling of MR with field. This explanation is also applicable in the case of CrAs. With $\mathbf{B} \parallel c$-axis only a single, small Fermi surface pocket contributes to conductivity. It has a "semi-Dirac" dispersion, meaning it is linear in only a single k-space direction, just below the Fermi energy. There are, unfortunately, no angle-dependent measurements on CrAs at ambient or applied pressure to see if its behavior is as angle-sensitive as LMR in FeP. But a comparison can be made to CrP, which has the same semi-Dirac point at an even lower energy. The MR in that compound is very large (much larger than that of CrAs) with significant anisotropy, but is not linear for any field orientation, which can be explained by the semi-Dirac point being further from E_F [112]. Evidently large and linear MR have two separate origins in the Cr pnictides. The difference in magnetotransport between CrP and CrAs despite similar RRR values is another sign that large MR is not solely a product of high sample purity. FeP, then, just happens to have the right combination of properties to exhibit both linear and large MR. DFT calculations from Limin Wang show that there is a semi-Dirac point at about -100 meV. This is further away than that predicted for CrP (-47 meV), but the evidence from EDS for nonstoichiometry in high RRR FeP samples could lead to a change in E_F that potentially moves it closer to the partially linear dispersion.

Previous quantum oscillations results detected multiple frequencies with field

along the FeP c-axis [111]. But based on the lattice parameters and the size of the effective Brillouin zone below T_N, only frequencies below about 1000 T can potentially correspond to orbits of a single pocket. All higher frequencies represent orbits whose areas are larger than the $k_a - k_b$ plane of the first Brillouin zone. That means they must stem from "magnetic breakdown", a situation in which the energy of the field enables carriers to skip between multiple pockets and zones [52], that has been suggested to occur in both MnP and FeP [111, 119]. Only one of the observed frequencies for $\mathbf{B} \parallel c$-axis is below 1000 T. Therefore it seems that FeP, like CrAs under pressure, has conduction through only a single pocket when field is applied along [001]. In fact, only for $\mathbf{B} \parallel c$-axis is there a single frequency below 1000 T, and all others are above 3000 T, far exceeding orbits that stay only in the first BZ.

For S1, SdH oscillations appear at many angles for fields up to 35 T, but not $\mathbf{B} \parallel$ [001]. Oscillatory behavior is not possible if all carriers are in the lowest Landau level; this is the same condition for linear MR, and thus explains both observed phenomena for this orientation. As was noted in the work on CrAs, the critical field for all carriers to be in the lowest LL goes as $(E_c - E_F)^{\frac{3}{2}}$, where E_c is the energy of the crossing point [19]. Thus a very small pocket, at low temperatures, will require a very small field to enter the quantum limit. The vanishing effective mass in the case of a linear dispersion further lowers this requirement.

5.6 FeP: Conclusions

The magnetoresistance of FeP is large and nonsaturating at all angles. Its dependence on sample quality and the results of Hall measurements indicate that it is related to electron-hole compensation, though to a lesser degree than in other, semimetallic systems. Large MR has a "turn on" temperature of around 35 K similar to that seen in binary pnictides in the MnP family and others. At most angles MR has a quadratic dependence, evolving to linear by 35 T. However, with field along the c-axis MR is linear from very low field, and quantum oscillations vanish. This is ascribed this uniqueness to the highly anisotropic Fermi surface, as evidenced by angular MR measurements, in which only a single, small pocket is responsible for conduction in this orientation, and carriers quickly enter the lowest Landau level. Quantum criticality seems less likely due to the nonlinear temperature dependence in this system and the related pressurized CrAs, but that the presence of a semilinear dispersion might be required. Hints of unconventional superconductivity in CrAs under pressure are also an intriguing line of further study in this material.

Chapter 6: Near Ferromagnetism in CoAs

6.1 Introduction

While at first glance CoAs has obvious structural and compositional similarities to FeAs and FeP, there are some distinguishing features. Near 1000 °C, CoAs transitions to the hexagonal NiAs structure, a property also seen in some other materials from this family but neither of the Fe-based binaries. Moreover, the electron count differs, because Co is one spot to the right on the periodic table, and has seven, not six, $3d$ electrons. The Fe-Co line is the border of magnetic ordering in this family. From left to right on the periodic table, CrAs, MnP, FeP, and FeAs are all ferro- or antiferromagnetic at low temperatures. In contrast, CoAs, CoP, and NiAs are all paramagnetic [40].

There were previously no low temperature reports on CoAs single crystals beyond neutron work to characterize the structure and show that there was no long range magnetic order [28]. Despite that, the magnetic susceptibility had been observed to have an unexplained nonmonotonic temperature dependence [28,40]. CoAs merited investigation as a PM but potentially magnetically unstable comparison to the complicated ordering of the Cr, Mn, and Fe-based materials. As already noted, interesting behavior such as superconductivity can emerge near the boundary of

magnetic transitions [126].

This chapter will parallel that on FeAs. CoAs crystals can be grown by both CVT and bismuth flux, and quantum oscillations were seen in flux samples samples in torque measurements at the NHMFL. As in the case of FeAs, predicted QO frequencies and masses can be compared to theoretical values coming from DFT calculations. Here, experiment does an even better job of matching theory, resulting in an experimentally verified Fermi surface picture. This can be combined with resistivity, Hall effect, heat capacity, and magnetization measurements to provide a comprehensive overview of the properties of binary CoAs. Interestingly, DFT calculations actually favor, though only very slightly, a FM ground state, despite the confirmation that CoAs is indeed paramagnetic. However, features in the temperature-dependent magnetic susceptibility and heat capacity are signs of the presence of magnetic fluctuations. The conclusion is that CoAs is nearly ferromagnetic, and future work to manipulate magnetic fluctuations with pressure, chemical substitution, or other techniques may stabilize interesting ground states.

6.2 Crystal Growth

As noted in Chapter 2, synthesizing CoAs single crystals is very similar to growing FeAs, and can be done with Bi flux or I_2 CVT at comparable temperatures. One difference is that flux-grown crystals CoAs are platelike, with typical dimensions of $0.4 \times 0.2 \times 0.1$ mm^3, in contrast to the needlelike FeAs Bi flux single crystals and the much larger and irregularly shaped crystals that result from CVT

[Fig. 6.1(a)]. The axis perpendicular to the basal plane is always c, the longest crystal axis. Growths whose maximum temperature was 1000 °C and which were spun at 925 °C had a more hexagonal shape [Fig. 6.1(b)]. Several MnP-type compounds transition between the orthorhombic structure and the hexagonal NiAs structure at high temperatures, including CoAs ($T_S \approx 975$ °C) [23]. Tremel et al. theorized that the orthorhombic structure was more stable than the hexagonal one in the binaries only for d^2 to d^6 transition metals, and that starting at d^7 another orthorhombic structure, the NiP type, should be favored [22]. Yet CoAs bucks this trend (as does CoP), and retains the unit cell seen in the Cr-Fe pnictides. Regardless of appearance, room temperature powder XRD of the hexagonally-shaped crystals shows them to be orthorhombic, despite of their appearance, and the conclusion is that they form in the hexagonal structure with the corresponding morphology, before trasitioning during cooldown. CVT was the method used for single crystal growth in past studies of CoAs [28, 127]. CVT crystals are much larger than those grown out of flux, with dimensions exceeding 1 mm. Like the Fe-based materials, they have an irregular, polyhedral shape, making principal axes more difficult to identify. But if orientation can be established, they are much easier to use for Hall effect, heat capacity, and magnetic measurements than flux samples. Powder XRD measurements of CVT and flux crystals give the same lattice parameters: $a = 5.28$ Å, $b = 3.49$ Å, and $c = 5.87$ Å, which also match previous results [28, 40].

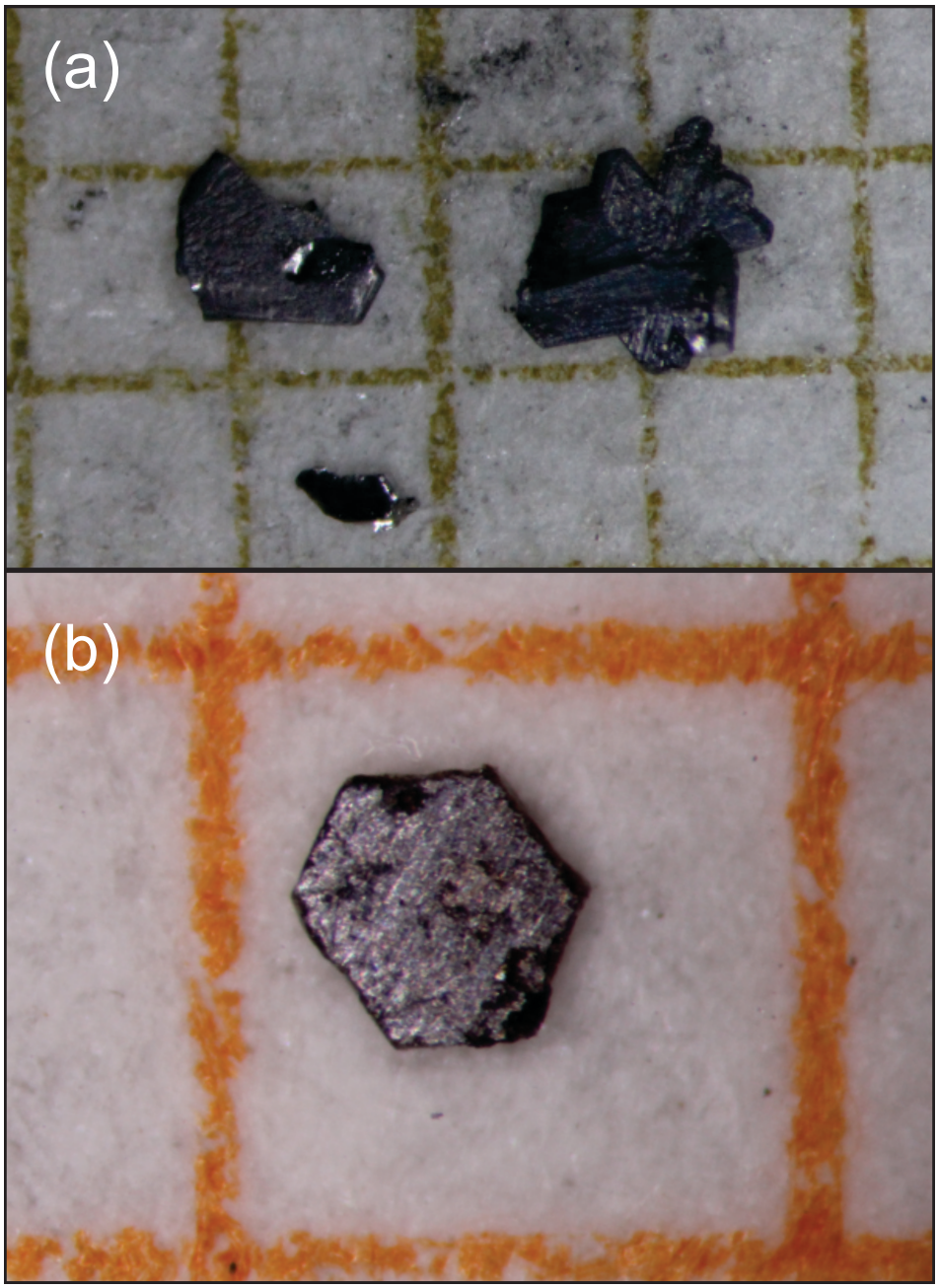

Figure 6.1: (a) Comparison of CoAs crystals grown by I_2 CVT (upper two samples) and Bi flux (lower sample). The CVT samples are much larger, but with a much more irregular shape, sometimes composed of multiple single crystals fused together. (b) A Bi flux crystal from a higher temperature growth with a more hexagonal shape, a product of the high temperature orthorhombic-hexagonal structural transition. In both photos the grid size is 1 mm $\times$ 1 mm.

6.3 Physical Properties

The resistivity of single crystal CoAs [Fig. 6.2(a)] is 60-80 $\mu\Omega$ cm at room temperature and displays a featureless, slightly sublinear temperature dependence before saturating for T $<$ 30 K. The residual resistivity ratio (RRR), defined as ρ(300 K)/ρ(1.8 K), is up to 70 for flux crystals compared to about 40 for the best CVT samples. Typical resistivities at 1.8 K are roughly 1-2 $\mu\Omega$ cm, with slightly higher values for CVT samples. As with FeAs, the lower residual resistivity of the smaller Bi flux crystals is interpreted as an indication that they are of higher quality than those grown with vapor transport, though the effect is not as dramatic in this case. Given the more regular shape of flux-grown crystals in both cases, they may be less likely to have two intergrown crystals with different orientations that would lead to domains and grain boundaries. Measurements of the magnetoresistance up to 31.5 T showed anisotropy, but the MR was only 0.5-2.8, with similar quadratic-to-linear behavior to FeAs.

Hall effect measurements were performed between $\pm$9 T on the wider vapor transport crystals, with the antisymmetric component of the MR in Hall geometry used to calculate R_H [Fig. 6.2(a), inset]. The antisymmetrized curves are linear with a positive slope over the entire temperature range, indicating hole-dominated conduction. Data sets for multiple samples show a peak near 100 K. Similar sharp extrema have been observed in R_H measurements of Sb [128], CrB_2 [129], and of course FeAs [95]. In the previous chapter FeP exhibited a nonmonotonic temperature dependence. The peak is clear evidence for multiband transport with a significant

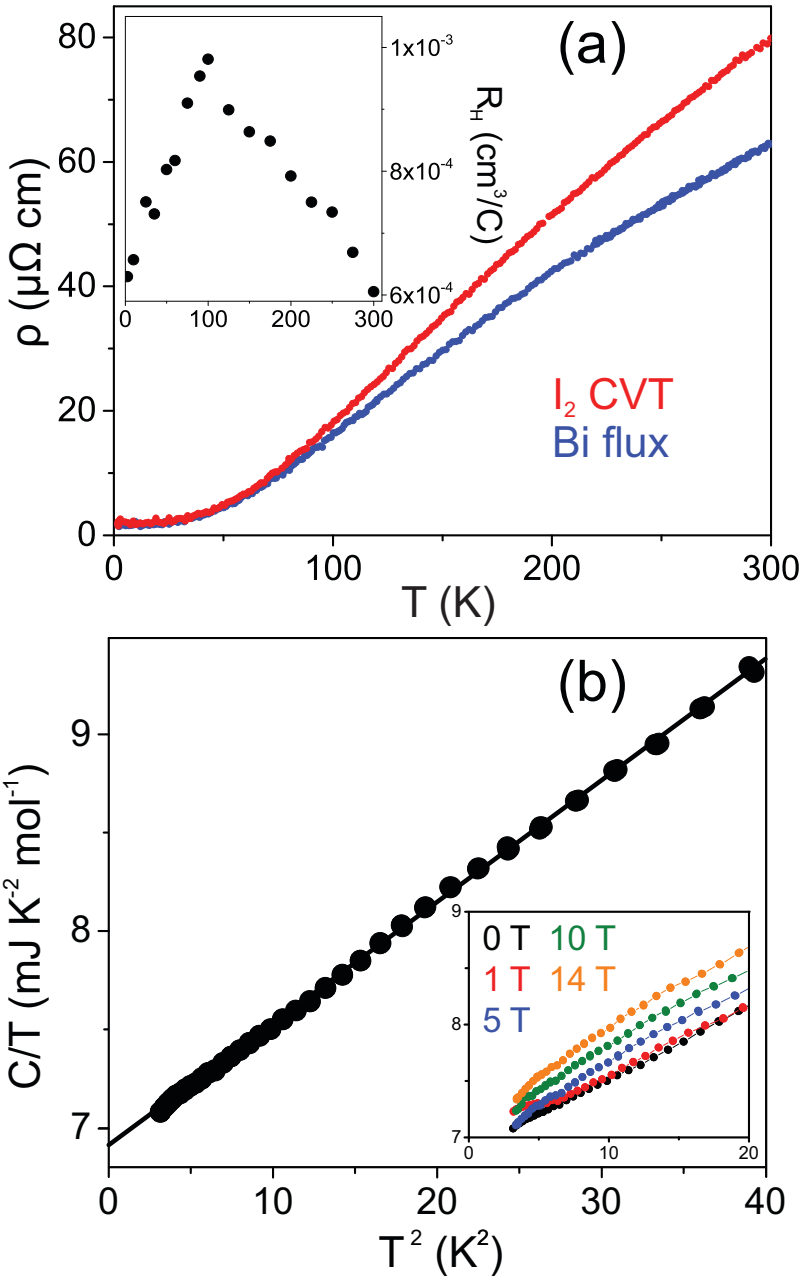

Figure 6.2: (a) The resistivity of CoAs single crystals grown by Bi flux and I_2 vapor transport. Inset: temperature dependence of the Hall coefficient. (b) Low temperature molar heat capacity. The line is a fit of the 0 T data to $C/T = \gamma + \beta T^2$ for 4.5 K $< T <$ 7 K. Inset: a closeup of the same data, as well as that for various applied fields, at lowest temperature. Lines connect points and are not fits.

temperature dependence of carrier density and/or mobility, though the linearity of the Hall resistivity makes this more difficult to assess. The theoretical calculations and quantum oscillations measurements to be presented support the notion that multiple carrier types are present. In FeAs and CrB_2 the R_H peaks occur at the onset of antiferromagnetism. However, no other measured properties of CoAs show features near the location of the R_H maximum.

Single crystal heat capacity data were taken at low temperature. Figure 6.2(b) shows the data in zero field with a straight line fit to the standard low temperature heat capacity model (3.1) for 4.5 K $< T <$ 7 K. The fit yields $\gamma = 6.91$ $\frac{\text{mJ}}{\text{K}^2\ \text{mol}}$ and, from β, a Debye temperature $\theta_D = 397$ K. These values are close to those seen in FeAs ($\gamma = 6.652$ $\frac{\text{mJ}}{\text{K}^2\ \text{mol}}$, $\theta_D = 353$ K) [30] and CrAs (7.5 $\frac{\text{mJ}}{\text{K}^2\ \text{mol}}$ and 370 K) [130]. For MnP, γ is estimated to be 5.4–7.6 $\frac{\text{mJ}}{\text{K}^2\ \text{mol}}$, with a large uncertainty due to magnetic contributions [131]. The closeness of these values shows the electronic and phononic similarities of this group of compounds, even with differences in magnetic order. Closer to 1.8 K, there is a subtle bump followed by a drop in C/T. Similar behavior was observed in near ferromagnets $CaNi_2$ and $CaNi_3$ [132], and a low temperature enhancement in C/T can be an indicator of spin fluctuations [133,134]. This feature is much less noticeable in CoAs than other materials, but it is still present in measurements in fields up to 14 T, where there is a slight positive deviation from linearity in C/T below 10 K^2, followed by a lower temperature drop [Fig. 6.2(b), inset].

Measurements of magnetization were also done on an unaligned CVT crystal. The susceptibility of single crystal CoAs has a small moment that increases slightly

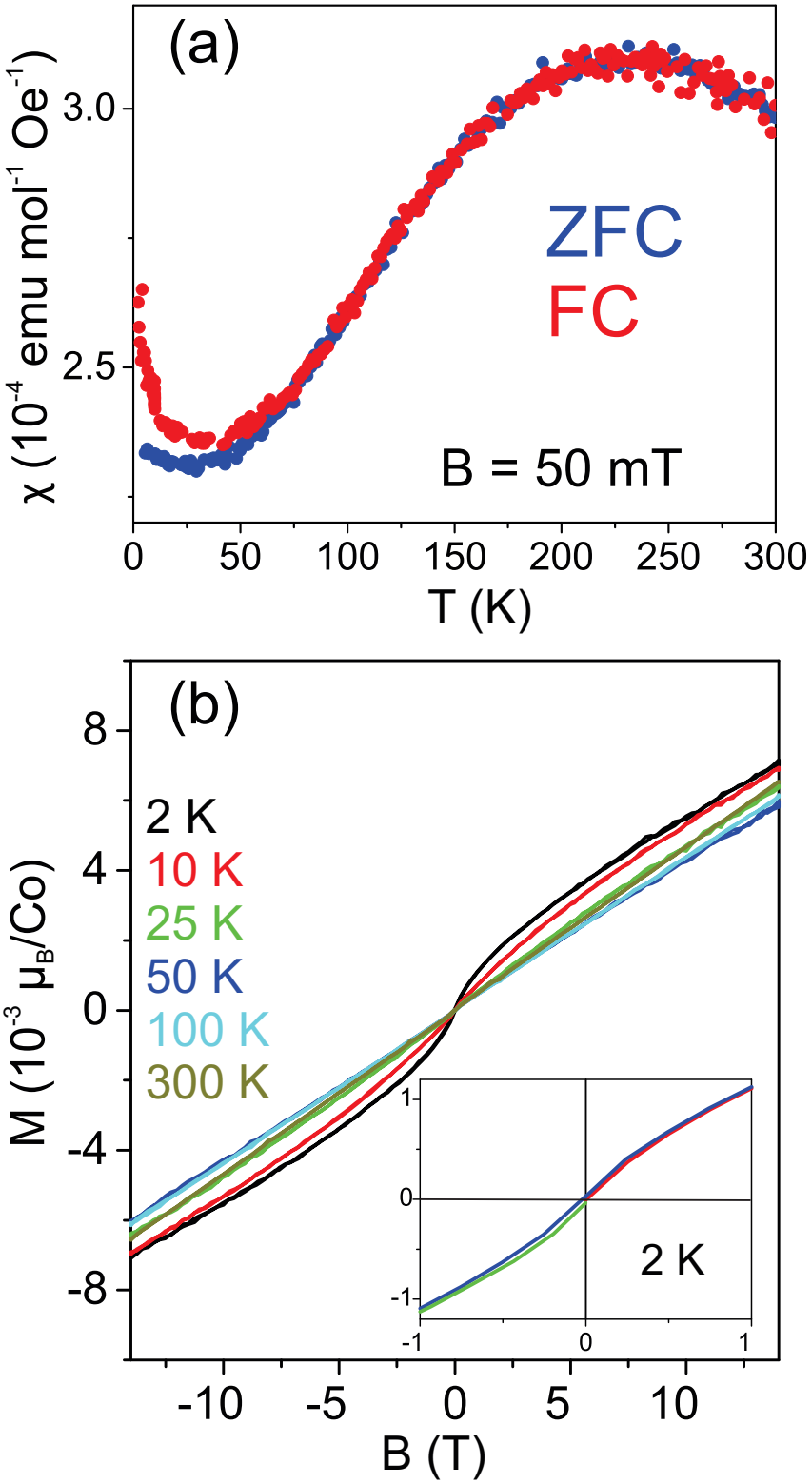

Figure 6.3: (a) Zero field cooled (ZFC) and field cooled (FC) magnetic susceptibility data of a CoAs single crystal. (b) Field dependence of magnetization between ±14 T at various temperatures. Inset: a closeup of the 2 K data between ±1 T. The initial upsweep is red, the downsweep blue, and the return sweep light green.

upon initial cooling, with a broad maximum around 225 K [Fig. 6.3(a)], followed by a minimum near 35 K. The magnitude and features are generally similar to previous reports for polycrystal [28, 40], though the minimum at low temperatures is not as sharp as the kink seen by Saparov et al. This could indicate that the kink reported in that work is actually from an impurity phase. Also, the low temperature susceptibility does not exceed the higher temperature value for single crystals. A similar broad peak just above 200 K is also seen in FeAs [95], which has a similar overall shape of temperature-dependent susceptibility above T_N to CoAs. Motizuki qualitatively explained the observed maxima in both compounds as stemming from the temperature dependent spin fluctuations, which saturate in amplitude above the temperature of the peak [135]. The difference would then be that in FeAs these fluctuations eventually settle into an ordered state. In CoAs on the other hand, like the low temperature bump in heat capacity, the susceptibility peak indicates an unfulfilled tendency to magnetic order.

At low fields, the field-cooled curve shows a larger low temperature upturn than the zero field-cooled curve, but the difference is small and disappears above 0.2 T. The size of the upturn is also sample dependent, and so is most likely the result of paramagnetic impurities, without which χ would simply plateau with further temperature decrease. This would also explain why the upturn is larger for powder samples in other work, as those are more likely to have corruption from other phases. Changing the magnitude of the applied field did not vary the value of χ or location of the peaks between 0.05 and 7 T, nor was there much change the susceptibility values. Field-dependent magnetization up to 14 T [Fig. 6.3(b)] is nonsaturating

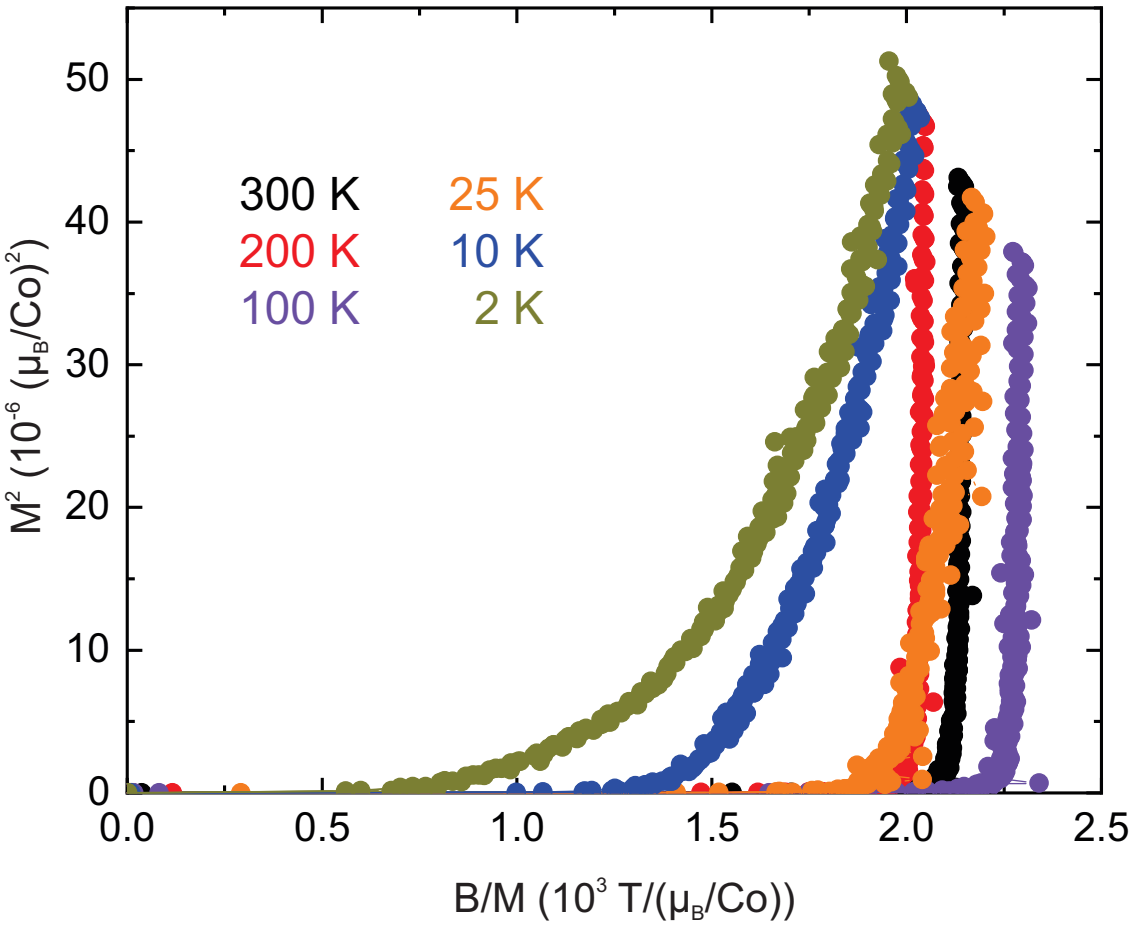

Figure 6.4: An Arrott plot showing B/M vs. M^2 for CoAs at various temperatures. The lack of a positive y-intercept indicates that there is no spontaneous moment at zero field, and therefore no ferromagnetism.

at all temperatures from 300 K to 2 K, and nonlinear at low field for T $\leq$ 10 K. There is negligible hysteresis at 2 K [Fig. 6.3(b), inset], indicating a lack of clear FM behavior. An Arrott plot using M(B) data at 2 K similarly shows no sign of long range magnetic ordering [Fig. 6.4]. All signs point to CoAs being PM, the same conclusion reached in previous magnetic and 4.2 K neutron diffraction measurements [28, 40]. A weak FM moment was observed in a powder sample by another group [136], but could be the result of the inclusion of ^{57}Fe in those samples for later Mössbauer study.

6.4 Theoretical Calculations

The electronic structure of CoAs was obtained via first-principles density functional theory calculation of the paramagnetic state. As with FeAs, all theoretical work was done by Limin Wang. The calculation was conducted using the WIEN2K [137] implementation of the full potential linearized augmented plane wave method within the Perdew-Burke-Ernzerhof generalized gradient approximation using the lattice parameters obtained from powder XRD. The k-point mesh was taken to be 11 $\times$ 17 $\times$ 10. Figure 6.5 shows the PM band structure, density of states and Fermi surface of CoAs. The Fermi surface consists of two hole pockets and two electron pockets, and the bands around the Fermi level are dominated by the Co d orbitals. The electron pockets have a "Czech hedgehog" shape centered at the Y point. The concentric hole pockets occupy the center of the first Brillouin zone but spread into other zones, resembling connected hourglasses.

Four possible magnetic ground states were considered: paramagnetic, ferromagnetic, and two distinct antiferromagnetic orderings—one in which Co atoms align ferromagnetically with nearest neighbors and antiferromagnetically with next nearest neighbors, and another where they are antiferromagnetic with both. These are the same orderings considered for FeAs [99], which do not completely match that compound's SDW. DFT results show a preference for FM over PM in CoAs by 20 meV/Co atom, with the two AFM scenarios at much higher energies. This energy difference translates to about 230 K, the location of the local maximum in susceptibility. The calculated moment for the theoretical FM state is $0.28\mu_B$, smaller than in any of the AFM binary pnictides [Table 2.1], with only FeP having a value at all close. Another theoretical study claimed that the MnP type structure can naturally lead to a FM instability [32]. But measurements here and by others show no indication of long range magnetic ordering in CoAs. Additionally, the magnetization at 140 kOe and 2 K is still two orders of magnitude smaller than the expected moment. Neutron diffraction measurements saw no purely magnetic reflections and set an upper limit of $0.1\mu_B$ at 4.2 K on any potential FM moment [28], ruling out a moment close to the $0.28\mu_B$ prediction. The energy difference between ferro- and paramagnetism is in truth small. It is possible that the onset of magnetic ordering occurs at an even lower temperature than that reached in these experiments or previous ones, but measurements with an adiabatic demagnetization refrigeration setup showed no resistive transitions down to 100 mK. The small energy difference is within the inherent uncertainty of DFT due to the need to arbitrarily choose approximations without full knowledge of the relevant parameters. Experimentally,

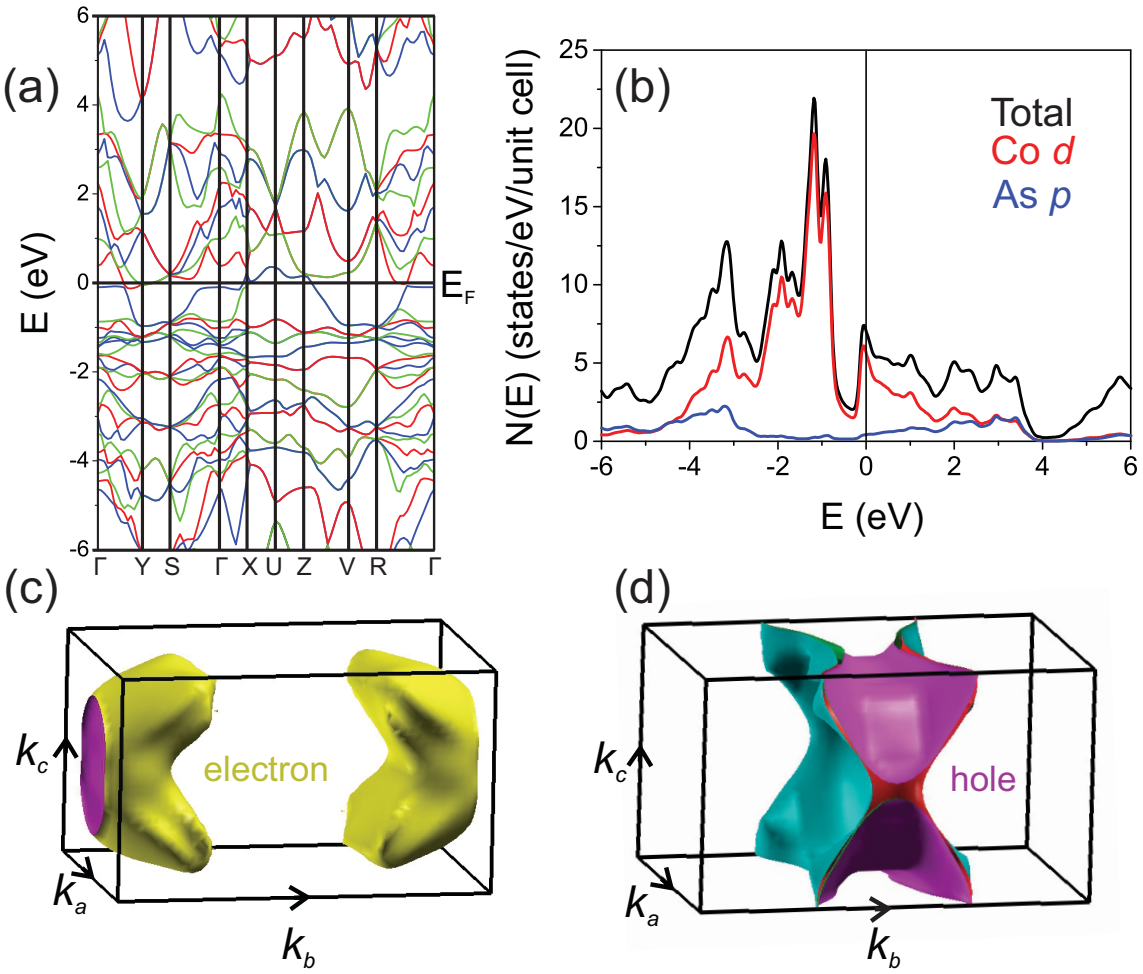

Figure 6.5: DFT-calculated (a) band structure (where different colors distinguish different bands), (b) density of states, (c) electron and (d) hole Fermi surfaces of paramagnetic CoAs.

CoAs is by all indications paramagnetic; DFT simply reinforces the idea of its nearly ferromagnetic properties.

One way to quantify near ferromagnetism is the dimensionless Wilson ratio R_W (2.1). For CoAs, $R_W = 6.2$, comparable to the values for the known near ferromagnet Pd (R_W = 6–8) [49] and $BaCo_2As_2$ (7–10, depending on field orientation) [50], which is thought to be near a magnetic quantum critical point. R_W can be reconfigured as the Stoner factor Z = 1-$\frac{1}{R_W}$, where Z $\rightarrow$ 1 signifies stronger ferromagnetic correlations. $Z_{CoAs} = 0.84$, similar to near ferromagnets $CaNi_2$ (0.79) and $CaNi_3$ (0.85) [132], which showed a low temperature enhancement in C/T. Both theoretical and experimental results point to strong low temperature FM fluctuations in CoAs.

DFT calculations were also made for paramagnetic FeAs with the same methods and a comparison to CoAs is in Fig. 6.6. The electronic structures of PM FeAs and CoAs differ only by a rigid band shift, as demonstrated by the fact that raising the Fermi level of the calculated FeAs band structure [Fig. 6.6(a)] and density of states plot [Fig. 6.6(b)] nearly reproduces the CoAs equivalent in both cases. The shift is about 1 eV, which is logical given that Co has an extra electron compared to Fe. To explore this relationship further the PM FeAs band structure was recalculated using the CoAs lattice parameters. It should be noted that while the *a*- and *c*-axes are smaller for CoAs compared to FeAs, the *b*-axis is actually longer, and that in general there is no simple dependence of the lattice parameters in the MnP family with element selection [Table 1.1]. There is a negligible difference in PM FeAs band structure calculated using the two unit cell sizes, indicating that the 70 K spin density wave onset in FeAs and corresponding lack of ordering in CoAs

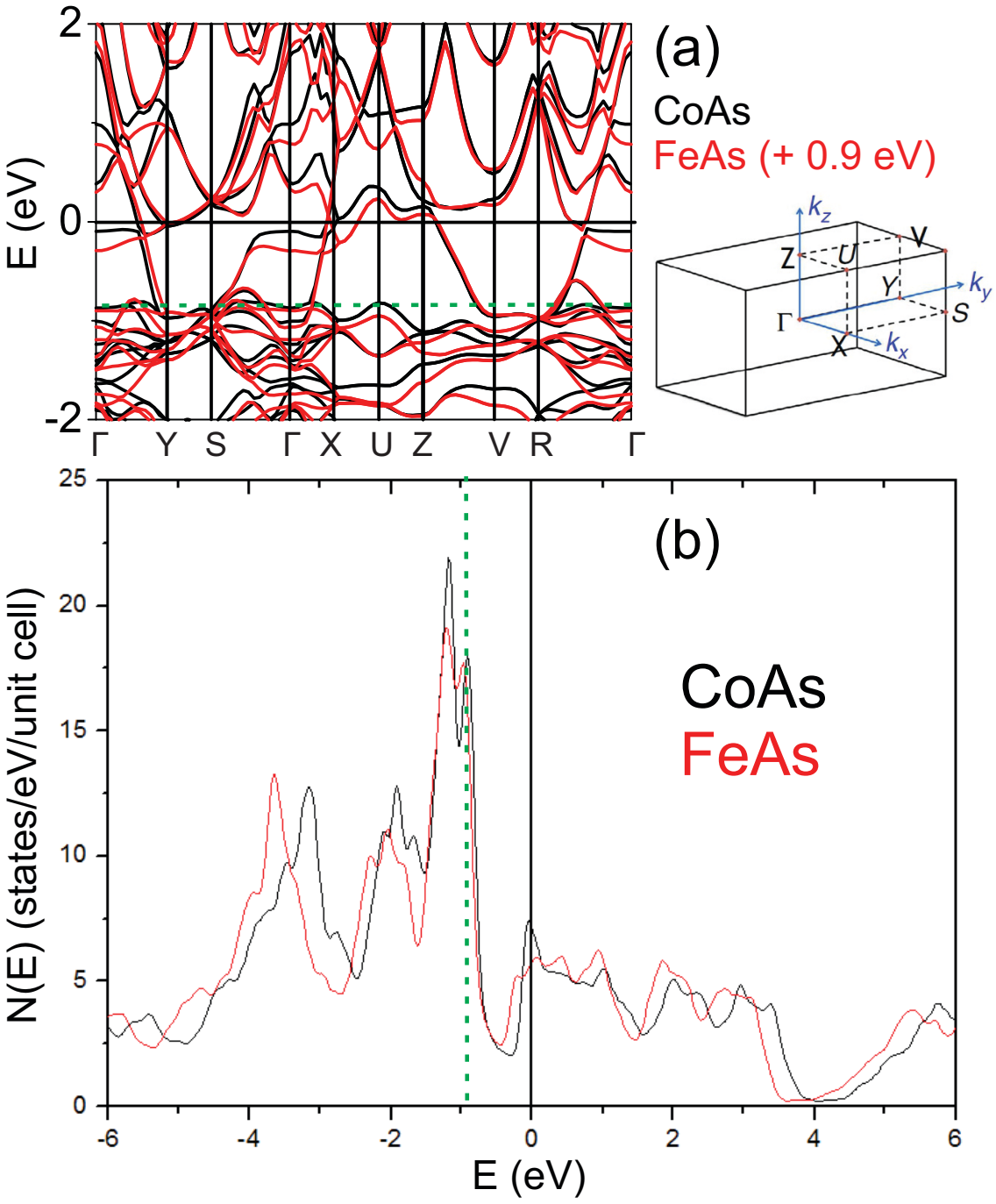

Figure 6.6: (a) A comparison of the band structures of paramagnetic FeAs (after having its Fermi level shifted up by 0.9 eV) and CoAs, with a schematic of the Fermi surface convention used. (b) A density of states comparison, with FeAs again shifted by 0.9 eV. In both plots a dashed green line indicates the original Fermi level of FeAs.

has a more complicated origin than just unit cell size and bond distance.

The predicted PM Fermi surface of CoAs is very different from that of FeAs [99], and low temperature AFM is also highly unfavored in CoAs. The relatively empty dispersion in the region between -1 and 0 eV and significant dropoff in the density of states at E_F are probably responsible for this, as the density of states near E_F is thought to have a large impact on the behavior of spin fluctuations [135], as is seen in Stoner theory. A significant difference in magnetic ordering occurs in other Fe and Co binaries. FeSe and CoSe can both be synthesized in a tetragonal structure. FeSe is a PM, potentially spin-fluctuation mediated superconductor ($T_c = 8$ K) [138], while below 10 K CoSe is a spin glass [12]. Like the arsenides, their band structures and densities of states have essentially a 1 eV shift between them [139]. CoSb (in the hexagonal NiAs structure) goes from PM to a spin glass phase with Fe substitution, while FeSb itself is AFM [140]. For both pnictides and selenides of Fe and Co, rigid band shifts coming from the extra cobalt electron have a large effect on ground state magnetism.

6.5 Quantum Oscillations

Measurements of longitudinal resistance and magnetic torque were made at the NHMFL up to 31.5 T on single crystals grown from Bi flux. Magnetotransport was featureless and reached about three times the sample resistance without a significant change in field dependence, and no oscillations were visible. However, oscillations were readily observable in the more sensitive torque signal as low as

6 T. Figure 6.7(a) shows the torque at selected orientations of the sample relative to applied field. Various oscillation frequencies emerge in the data over the entire angular range, though some correspond to harmonics or the sum of independent fundamental frequencies. As with FeAs, experimental results could be compared to DFT band structure predictions with the SKEAF program [82].

6.5.1 Fermi Surface Geometry

The change in oscillation frequency spectrum with applied field angle reflects the geometry of the Fermi surface pockets. In the measurement $\phi = 0°$ corresponded to $\mathbf{B} \parallel c$-axis, while $\phi = 90°$ was $\mathbf{B} \parallel b$-axis. The c-axis was confirmed by single crystal XRD on the platelike sample. Given the ambiguity of the orthorhombic structure for a square plate crystal, the second axis determination was made on the basis of comparison to theoretically predicted frequencies. The observed angular dependence matched very well to predictions for $\mathbf{B} \parallel b$-axis but not at all for $\mathbf{B} \parallel a$-axis. Data were taken in 5° intervals from 0° to 100° and at 120°, 150°, and 180° [Fig. 6.7(b)].

There were four distinct frequencies predicted by SKEAF, but in the experimental data only three independent sets of oscillations were observed. Each one can be assigned to one of the predicted electron bands and the two hole bands based on similarities between calculated and observed frequencies [Fig. 6.7(c)]. There is some slight disagreement in exact frequency value, but the angular dependence matches well. The unobserved band corresponds to a second electron band, and does not

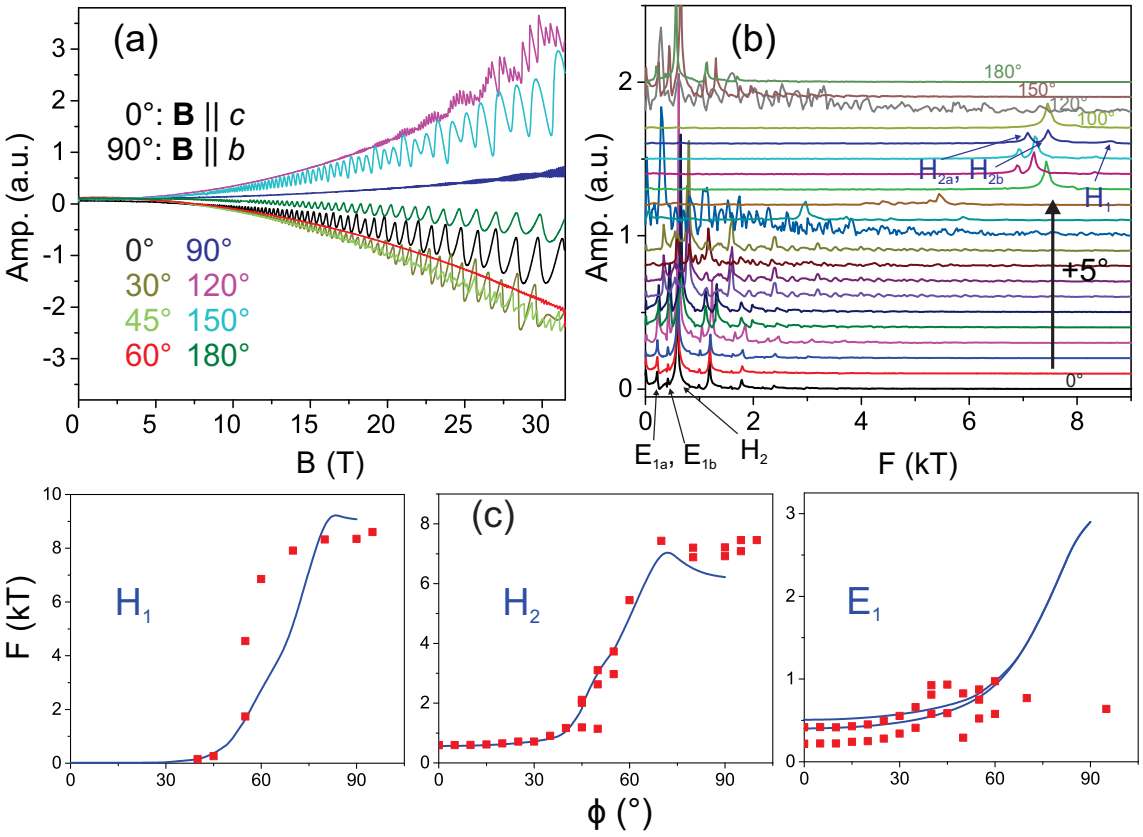

Figure 6.7: (a) Magnetic torque of a CoAs single crystal at various angles at base temperature (400-500 mK), where **B** $\parallel$ c-axis at 0° and the b-axis at 90°. (b) Fast Fourier transforms of the oscillatory component of the torque for each angle, offset for clarity. Unlabeled peaks are either higher harmonics or sums of the fundamental frequencies. Data between 0° and 100° were taken in 5° increments. (c) A comparison of observed oscillation frequencies (red squares) and those expected from the paramagnetic DFT band structure (blue lines) for three of the four predicted oscillation bands. H_1 and H_2 are hole bands, E_1 is an electron band. The latter two have some peak splitting.

match any of the angular dependent data. It is not atypical for a predicted band to be absent in measurements [82]. The missing band has the highest predicted effective mass, which would reduce the oscillation amplitude and make it more difficult to detect. Additionally, the predicted frequencies correspond to cross sectional areas much larger than the first Brillouin zone, and an erratic angular dependence indicative of a potentially unrealistic orbit, another known phenomenon with the SKEAF program. More important is that all experimentally observed frequencies can be indexed to a theoretical band. The extremal orbits predicted around the electron and hole pockets all have a nontrivial shape, and correspondingly the expected oscillation frequency also varies widely with angle.

The fact that, in spite of this complexity, there is still agreement in the plane in which rotational measurements were done indicates that the paramagnetic Fermi surface in Fig. 6.5 reflects the true CoAs Fermi surface as far as can be determined. The three bands are denoted H_1, H_2, and E_1, with H and E signifying hole and electron, respectively. The observed hole pockets show consistently higher oscillation frequencies than the electron pocket, meaning that they are larger, explaining the positive Hall coefficient. The linearity of the Hall signal, despite the presence of multiple carriers, can be attributed to a much greater number of hole carriers indicated by the larger oscillation frequencies of the hole bands. Carrier concentration scales as with oscillation frequency as $F^{1.5}$, so frequencies roughly three times as large for the two hole bands compared to the one electron band would mean n_h is an order of magnitude larger than n_e.

To extract oscillation frequencies a third order polynomial was fit to the raw

data and subtracted to obtain a residual oscillatory signal. Figure 6.8(a) gives examples at 100° and 180°. The frequency spectrum after a FFT is in Fig. 6.7(b). The oscillation frequencies, and therefore Fermi surface cross sectional areas, increase as the field more closely aligns with the b-axis. Accordingly, both the electron and hole Fermi surfaces have their largest cross sections in the ac-plane [Fig. 6.5]. Figure 6.7(c) shows the frequency at which peaks were observed at different angles (red squares), as well as the angular dependence predicted via SKEAF (blue lines) in the range 0°–90°. E_1 shows multiple peaks in this range. This and the increase in frequency closer to 90° are both in line with theory. The increase in frequency also comes with a decrease in amplitude, and it is not until 70° that peaks are again clear. At this point only H_1 and H_2 are observed, in the 7–8 kT range, with intermittent lower peaks potentially corresponding to E_1.

There are two angular ranges for which fewer than three bands appear: H_1 does not appear for $0° < \phi < 40°$, and E_1 does not appear at almost all angles above 60°. In both cases the disappearance of frequencies can be explained by experiment-related factors, rather than disagreement with theory. Until 40°, predicted H_1 frequencies are less than 35 T. Such a low frequency is hard to pick out in the FFTs, which cover a large, higher frequency range, and at fields comparable to oscillation frequency it is possible that the "quantum limit", where all carriers are in the lowest Landau Level, is reached, and no oscillations will be seen anyway. At high angles, the predicted effective mass for E_1 increases, exceeding $4m_e$. This will decrease oscillation amplitude, and so it is unsurprising to see this frequency band become less prominent in the data.

6.5.2 Effective Mass

Temperature-dependent measurements were made to determine effective masses in the k_a–k_c and k_a–k_b planes using the LK factor (2.22). At 100° [Fig. 6.8(a), left] H_1 and two split peaks stemming from the H_2 band appear. While the amplitudes show a decay with temperature, the fits to the LK formula are not great. In any case, they give $m^*_{H1,\ exp.} = 2.3m_e$, $m^*_{H2a,\ exp.} = 2.6m_e$, and $m^*_{H2b,\ exp.} = 2.4m_e$. The subscripts a and b denote the lower and higher of the two split frequencies. Theoretical predictions gave $m^*_{H1,\ th.} = 2.99m_e$ and $m^*_{H2,\ th.} = 1.91m_e$ at 90°—the frequency splitting of H_2 was not predicted. At 180° [Fig. 6.8(a), right] two split E_1 frequencies as well as one H_2 frequency are seen. Here the effective mass fits are much better [Fig. 6.8(b), right], and the H_2 signal survives to at least 15 K, indicative of lighter masses at this angle: $m^*_{E1a,\ exp.} = 0.70m_e$, $m^*_{E1b,\ exp.} = 0.36m_e$, and $m^*_{H2,\ exp.} = 0.46m_e$, compared to predicted values of $m^*_{E1a,\ th.} = 1.43m_e$, $m^*_{E1b,\ th.} = 1.44m_e$, and $m^*_{H2,\ th.} = 0.33m_e$. Overall the predicted and observed masses do not show close agreement, which speaks to the failure of DFT to capture the shape of the band dispersion. Encouragingly, however, the prediction of smaller masses for $\mathbf{B} \parallel c$-axis compared to $\mathbf{B} \parallel b$-axis is borne out by the data.

As with FeAs, the effective mass gives an alternate method of calculating the Sommerfeld coefficient (4.1). For $\mathbf{B} \parallel [010]$, the total γ comes out to 3.9 $\frac{\text{mJ}}{\text{K}^2\ \text{mol}}$, close to the value of 6.83 $\frac{\text{mJ}}{\text{K}^2\ \text{mol}}$ directly measured in heat capacity experiments. For $\mathbf{B} \parallel [001]$, $\gamma = 16.9$ $\frac{\text{mJ}}{\text{K}^2\ \text{mol}}$, a much larger value due to the reduced effective

masses in the *ab* plane. In either case no contributions at the Fermi level seem to be missing, despite not observing the fourth, heavier, DFT-predicted band.

6.5.3 Dingle Temperature

With the masses known, the Dingle temperature (2.23) and scattering rate (2.24) can be assessed. Again, it is only feasible to do Dingle analysis for peaks with a large relative amplitude at an angle for which m^* is known. Thus T_D could only be obtained for H_2 at 100° (by averaging the split peaks) and 180°, since the exponential decay of H_2 dominates the oscillatory signal [Fig. 6.8(a)]. Fitting the position of peaks with inverse field results in $T_{D,\ H2} = 3.66$ K and 14.1 K at 100° and 180°, corresponding to $\Gamma_{H2} = 3.0 \times 10^{12}$ s^{-1} and 1.2×10^{13} s^{-1}, respectively. The angular dependence of H_2 clearly shows it is not spherical, but it is possible to average the values for the two different field directions to obtain a rough estimate of $\ell = 500$ Å for H_2. The hole pocket has a significant directional dependence in terms of both effective mass and Dingle temperature between the *ac* and *ab*planes, as the values listed in Table 6.1 indicate. In the AFM states of CrAs, MnP, FeP, and FeAs, the *ab*-plane features two noncollinear rotating magnetic moments [21,29,46]. This could be a sign that any magnetic fluctuations in CoAs are occurring in the *ab* plane.

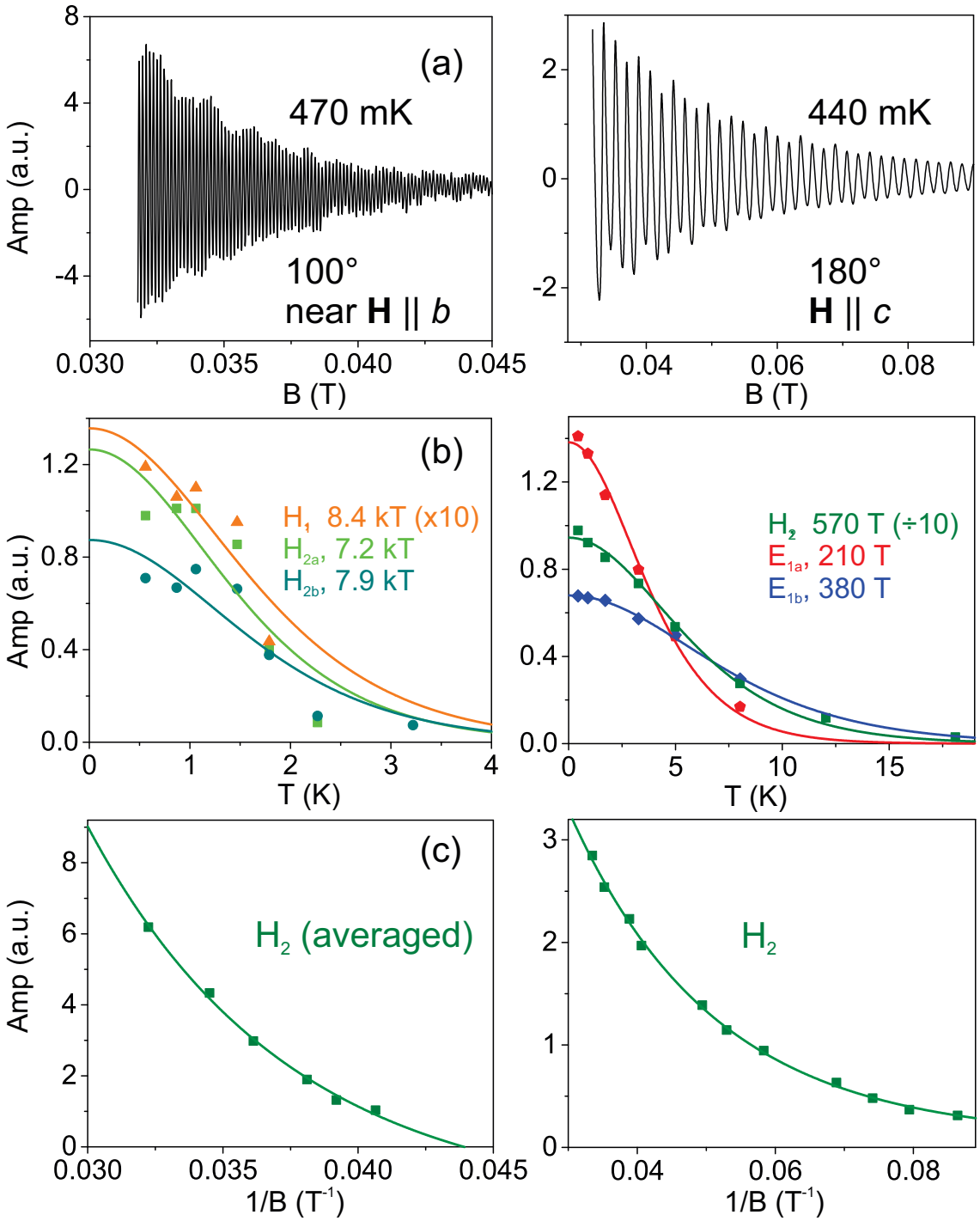

Figure 6.8: (a) Residual oscillatory signal for 100° (near **B** ∥ b-axis) and 180° (**B** ∥ c-axis). (b) Temperature dependence of the amplitude of the observed peaks at both angles, with fits to the Lifshitz-Kosevich factor. To ease comparison between different bands, on the left H_1 amplitude is increased by a factor of 10 and on the right H_2 decreased a factor of 10. (c) A plot of the peak amplitude versus inverse field for H_2 at both angles, with accompanying exponential decay fits to solve for the Dingle temperature. Only H_2 was used since it was the most prominent frequency in both cases. Data for 100° are an average of the two observed peaks.

Band	**B** ∥ [hkl]	F (T)	m^*/m_e	T_D (K)
H_1	[010]	8390	2.3	—
H_{2a}	[010]	7200	2.6	—
H_{2b}	[010]	7900	2.4	—
$H_{2,ave}$	[010]	—	—	3.66
H_2	[001]	570	0.46	14.1
E_{1a}	[001]	210	0.70	—
E_{1b}	[001]	380	0.36	—

Table 6.1: Parameters extracted from CoAs torque oscillations data with field applied in different directions. Note that what is called [010] actually corresponds to an angle 10° off of the b-axis. The average m^* of H_{2a} and H_{2b} was used in calculating T_D for $H_{2,ave}$.

6.6 CoAs: Conclusions

The flux-grown crystals of CoAs have a lower residual resistivity and more consistent orientation, but the vapor transport samples can grow much larger, enabling bulk measurements such as magnetization or heat capacity. Data show hole-dominated conduction with no indication of long range magnetic ordering down to 1.8 K. This is in line with previous polycrystal work, even as predictions slightly favor weak moment ferromagnetism. Quantum oscillations are present in torque starting from 6 T up to 31.5 T, and their angular dependence is in line with the geometry of the calculated paramagnetic Fermi surface.

Transition metal pnictide compounds and the iron-based superconductors have shown unique magnetic arrangements and often superconductivity upon suppression of ordered magnetism. CoAs is paramagnetic, but the nonmonotonic temperature dependence of its magnetic susceptibility and a low temperature enhancement of

heat capacity point to possible magnetic fluctuations. The notion of a ferromagnetic instability is also supported by DFT calculations favoring long range ordering at zero temperature, and other theoretical work has claimed that the inherent band structure of B31 materials may make them susceptible to ferromagnetic Stoner instabilities [32]. Furthermore, there are many similarities to antiferromagnetic FeAs. Both show a maximum in paramagnetic susceptibility, and their calculated electronic structure differs only by a one electron rigid band shift, with the effect of unit cell size apparently negligible.

An earlier pressure study [127] up to 10 GPa showed a possible structural transition at 7.8 GPa, and other elements of the structure identified by the authors indicate a potential sensitivity to lattice shifts at high pressures. Very basic high pressure measurements were made as a corollary to this study, but at 2 GPa ρ(T) was nearly indistinguishable from ambient pressure results. It is possible CoAs is already close to the crossover between stabilizing magnetic order and being dominated by fluctuations. Future work with chemically substituting or applying pressure to binary CoAs may lead to the discovery of structural, magnetic, or superconducting transitions.

Chapter 7: CoP: A Nonmagnetic Contrast

A look at CoP will round out the four possible Fe/Co-P/As combinations in the MnP-type family. As with CoAs, single crystal reports on this material were scant before the work shown here, consisting of just crystal structure analysis and high temperature magnetic susceptibility [23, 141, 142]. It too is void of magnetic order, a property that it can now be seen is determined by the occupant of the transition metal site in this family. It was previously found that, unlike CoAs, CoP does not undergo a high temperature transition to the hexagonal NiAs structure[1]. There are other differences between the two, and in fact some similarities in terms of transport properties to FeP. Investigation into CoP makes it possible to look at the effect of changing out the metal and pnictogen atom in the *Pnma* structure individually.

7.1 Crystal Growth

Unsurprisingly, CoP can also be grown with vapor transport. One notable aspect is that polycrystalline powders without impurity phases were much easier to make than for FeP. There is, evidently, a difference in reactivity of the two elements

[1] In fact, it has been noted that only arsenides can take on both structures [22].

with phosphorus. A previous report on crystal growth compared transport with the elements in a stoichiometric ratio or prereacted powders (with I_2 as the transport agent in both cases) [142], and saw higher mass transfer with the individual elements. However single crystals produced from either method are of to similar quality, and growths were left long enough for all material to react (10-14 days). As was also noticed for FeP, crystals grown from either starting material showed about a 55:45 Co:P ratio with EDS. Temperatures at the hot end of the tube from 900 °C to 1025 °C had no obvious impact on the growth. Since large crystals of sufficient quality could be grown with CVT, and flux growth was unsuccessful in the case of FeP, no attempts were made at flux growth of CoP. Lattice parameters from powder XRD of CVT crystals are $a = 5.08$ Å, $b = 3.28$ Å, and $c = 5.59$ Å, in agreement with previous reports [23].

7.2 Physical Properties

The electrical transport behavior of CoP is very similar to that of CoAs. The temperature-dependent resistivity has an initial linear decrease from room temperature (which is seen when electron-phonon scattering dominates) before saturating at lower temperature [Fig. 7.3(a)]. RRR of the best samples is about 80, higher than what was found with CoAs crystals grown by any method. The residual resistivity is about 0.5 $\mu\Omega$ cm. This parallels the higher RRR and lower ρ_0 of FeP in comparison to FeAs, indicative of a general trend of less impurity scattering in the phosphide binaries in comparison to the arsenides. That being said, the difference between the

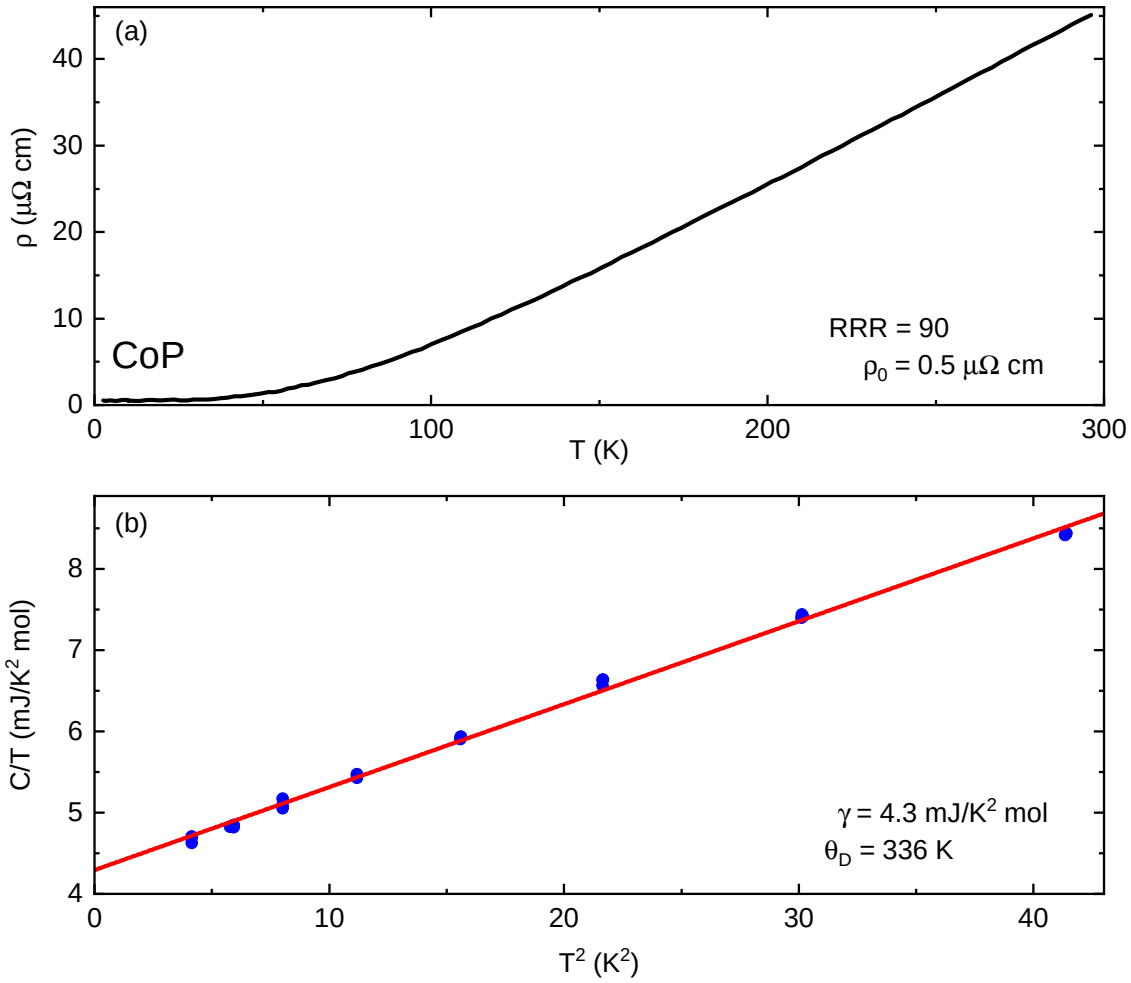

Figure 7.1: (a) Zero field resistivity as a function of temperature for a CoAs single crystal. (b) Low temperature specific heat of a CoP single crystal. The red line is a fit to the low temperature Debye model [Eq. 3.1], and extracted parameters from the fit are given.

two Co compounds in terms of RRR is much less.

Measurements of the specific heat were also made at low temperature. The data, when plotted as C/T vs. T^2, can be fit to a straight line with $\gamma = 4.3\ \frac{\mathrm{mJ}}{\mathrm{K}^2\ \mathrm{mol}}$ and $\theta_D = 336$ K [Fig. 7.1(c)]. Both values are slightly smaller than in CoAs and FeAs [11,30], but nevertheless indicate metallic behavior and a similar phonon dispersion to the other B31 structure materials. The smaller γ can be interpreted as a sign of slightly weaker correlations. This fits with the fact that CoP is further from long range magnetism than the three materials discussed thus far.

Magnetoresistance is large in CoP, increasing by nearly 100 times up to 31 T [Fig. 7.2]. As with FeP, the smallest increase comes for field very close to the c-axis. The lowest value at 31 T was actually found to be at -5°, but that could be from a slight misalignment of the rotator or the sample on the rotator. The inset to Fig. 7.2 shows the MR at 31 T for more angles, and illustrates the steep decline in MR over a narrow angular range near the c-axis. Data were not taken with as fine of spacing near $\mathbf{B} \parallel a$-axis, but the decrease in MR at 86° indicates that the same phenomenon may happen there as well. This would contrast with FeP, where the B $\parallel$ a-axis results in the highest magnetoresistance. None of the curves showed the linearity of FeP near B $\parallel$ c-axis, but rather the gradual crossover to high field linearity seen in FeAs and, away from the c-axis, FeP. Given that CoP is paramagnetic, it also confirms that the magnetism is not the primary reason for large MR in FeP, which also makes sense given that AFM FeAs has only a moderate field-induced increase. Though not as much Hall effect or temperature-dependent

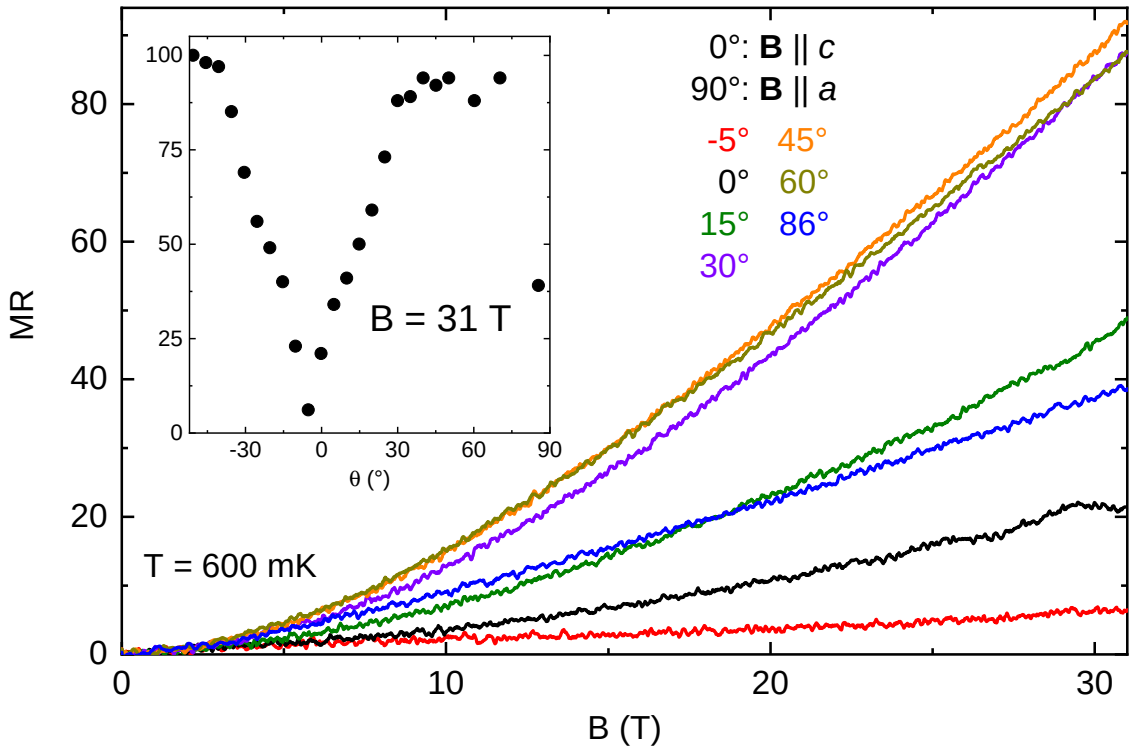

Figure 7.2: Transverse magnetoresistance of CoP at 600 mK and up to 31 T at different angles, with field rotated between being parallel to the a- and c-axes. Inset: the 31 T MR at various angles, extracted from different field sweeps rather than a single angle sweep.

MR data was taken on CoP, presumably it too shows some degree of compensation, resulting in the large increase in scattering in field. Note that MR never saturates, as was the case with FeAs or FeP. This indicates either some amount of compensation, or open Fermi surface orbits. While no quantum oscillations were seen in transport except possibly near $\mathbf{B} \parallel c$-axis (likely attributable to somewhat noisy data, and the generally difficulty of observing SdH oscillations in many of these compounds), many dHvA were seen at all angles in magnetic torque, making the latter scenario unlikely.

Magnetic measurements of CoP show an almost flat temperature dependence, with a slight dip around 250 K and divergence at lowest temperatures [Fig. 7.3(a)]. The data shown are with a 5 T applied field due to the small signal, but temperature sweeps at lower fields down to 0.1 T showed the same general temperature dependence, including the 250 K dip. There was none of the nonmonotonic behavior above the upturn that could be linked to magnetic fluctuations in CoAs and FeAs [135]. An Arrott plot has a negative y-intercept [Fig. 7.3(b)], indicating no spontaneous zero field magnetization. Using the specific heat and magnetization data, the Wilson ratio (2.1) can be calculated, and $R_W = 1.7$ is obtained. This is quite a bit lower than the value of 6.2 for CoAs, indicating much weaker ferromagnetic fluctuations.

7.3 Quantum Oscillations

As with FeAs and CoAs, magnetic torque measurements were carried out for a CoP crystal rotated such that field moved in the orthogonal ab and bc planes. This

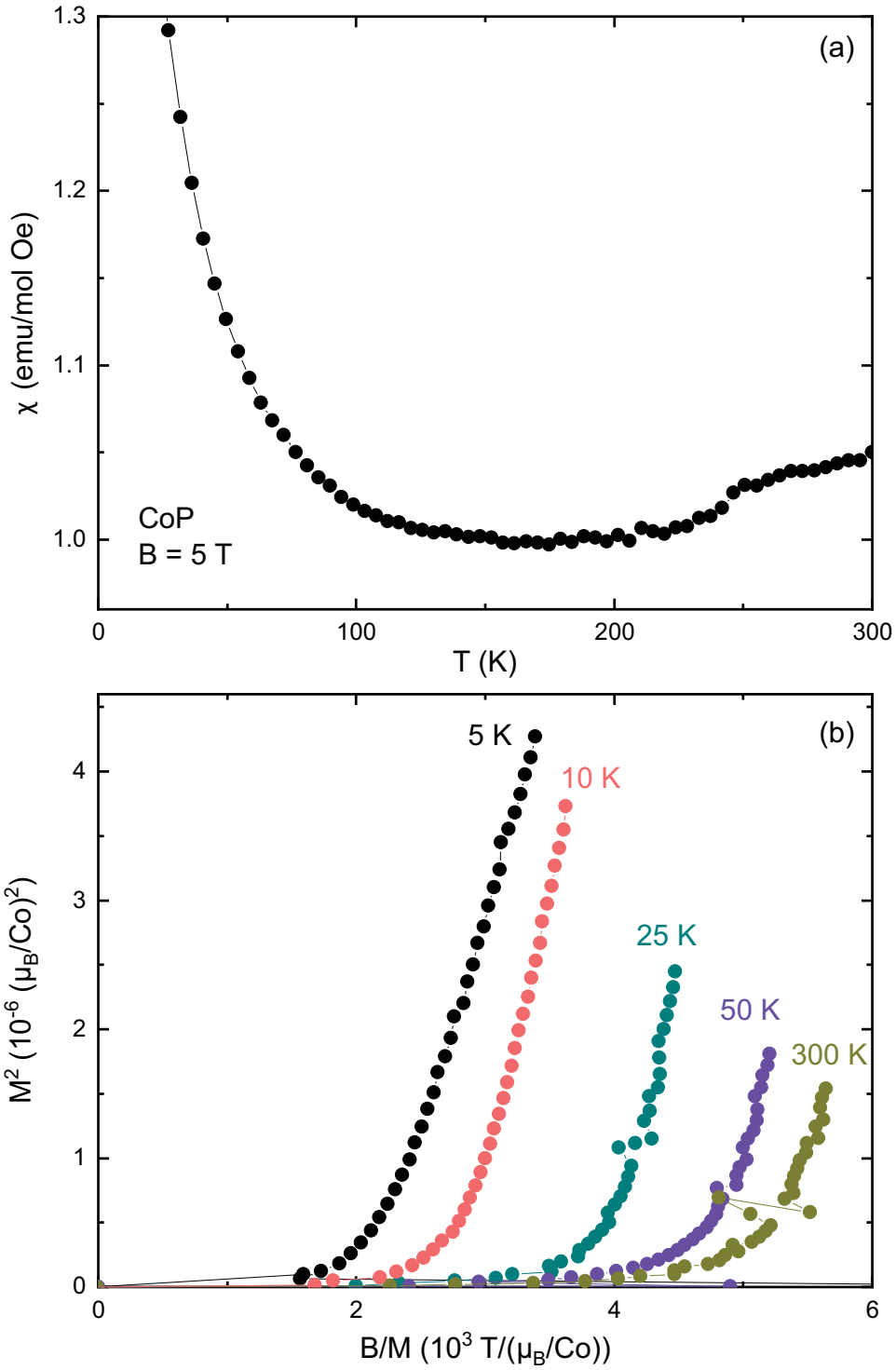

Figure 7.3: (a) M(T) of an unaligned CoP single crystal at B = 5 T. Fields down to 0.1 T had the same temperature dependence. (b) An Arrott plot for the same sample, showing a lack of ordered magnetism down to 5 K.

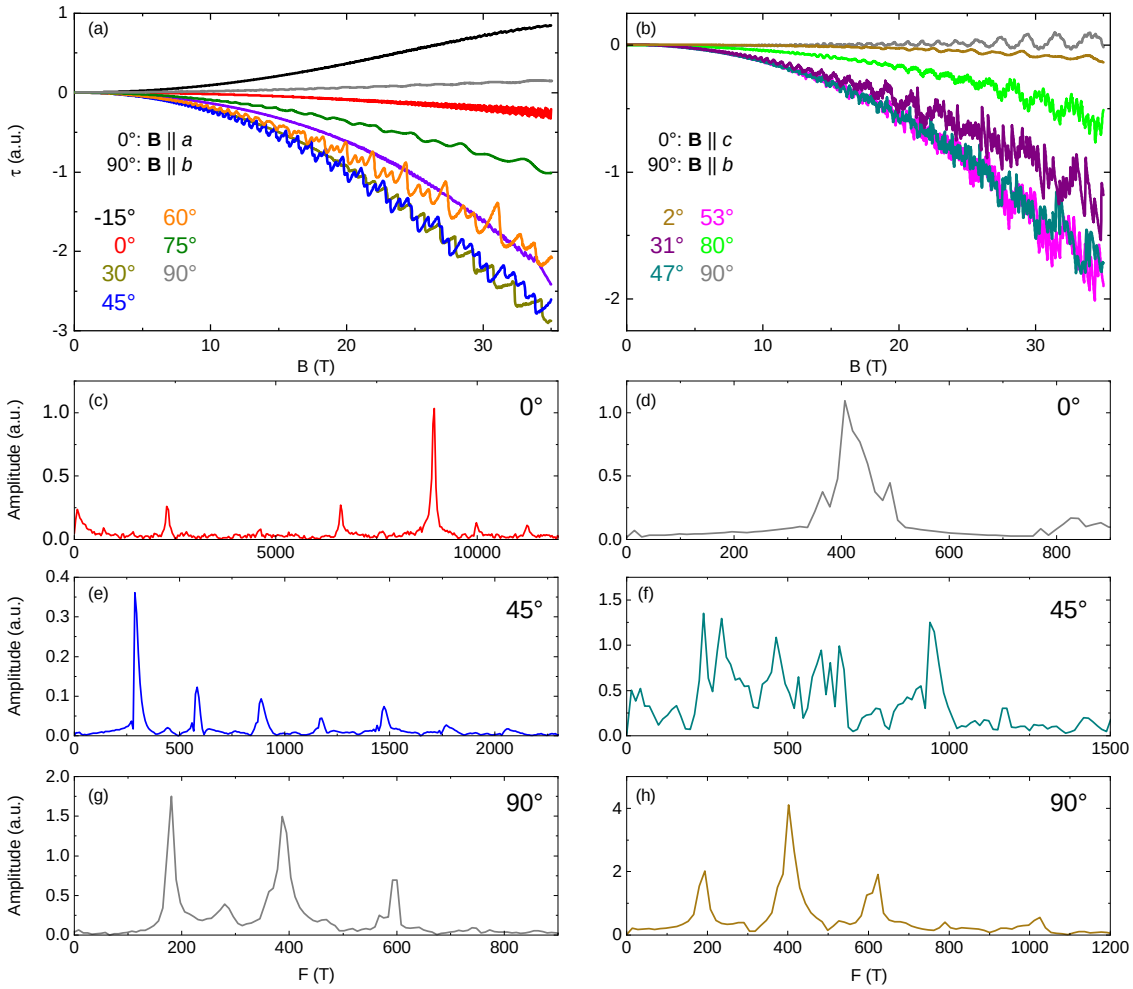

Figure 7.4: Magnetic torque of the same CoP crystal from 0 to 35 T rotated such that field moves in the (a) *ab* and (b) *bc* planes. (c-h) Fast Fourier transforms of the residual oscillatory signal after subtraction of a polynomial at 0°, 45°, and 90° for each of the two measurements. Note that (g) and (h) are at the same field orientation. Some higher frequency peaks have been cut off for ease of seeing lower frequencies.

allowed for a three dimensional analysis of quantum oscillation frequencies, of which there were many with widely varying frequencies. No band structure calculations were made for CoP from which theoretical frequencies and effective masses could be generated. For that reason, it is difficult to extract a detailed picture of the Brillouin zone from QO measurements alone, nor can it be determined whether fundamental frequencies come from electron or hole orbits. But still some comments can be made.

7.3.1 Angular Dependence

Raw torque data are shown in Fig. 7.4 for select angles up to 31 T, with more angles measured beyond those shown. Oscillations are clear at fields as low as 5 T. Measurements with field rotated in the b-c direction were slightly more noisy. There are clear differences in the oscillation pattern as orientation is changed, and these are reflected in the FFTs. The change in oscillation peak frequency as a function of angle is given in more detail in Fig. 7.5 for the two directions in which $\mathbf{B}$ was rotated. Note that the points connected by lines are only assumed to be the same orbit due to their similar frequencies; without theoretical input there is no way to confirm this. In tracking individual orbit frequencies, it does not seem that specific peak frequencies are changing significantly in value, though some appear over a limited angular range, which could potentially be put down to signal resolution (especially for higher frequency peaks, which often had a lower amplitude). This is quite different from FeAs and CoAs, where a smaller number of fundamental frequencies showed a clear angle dependence. The CoP Fermi surface generally

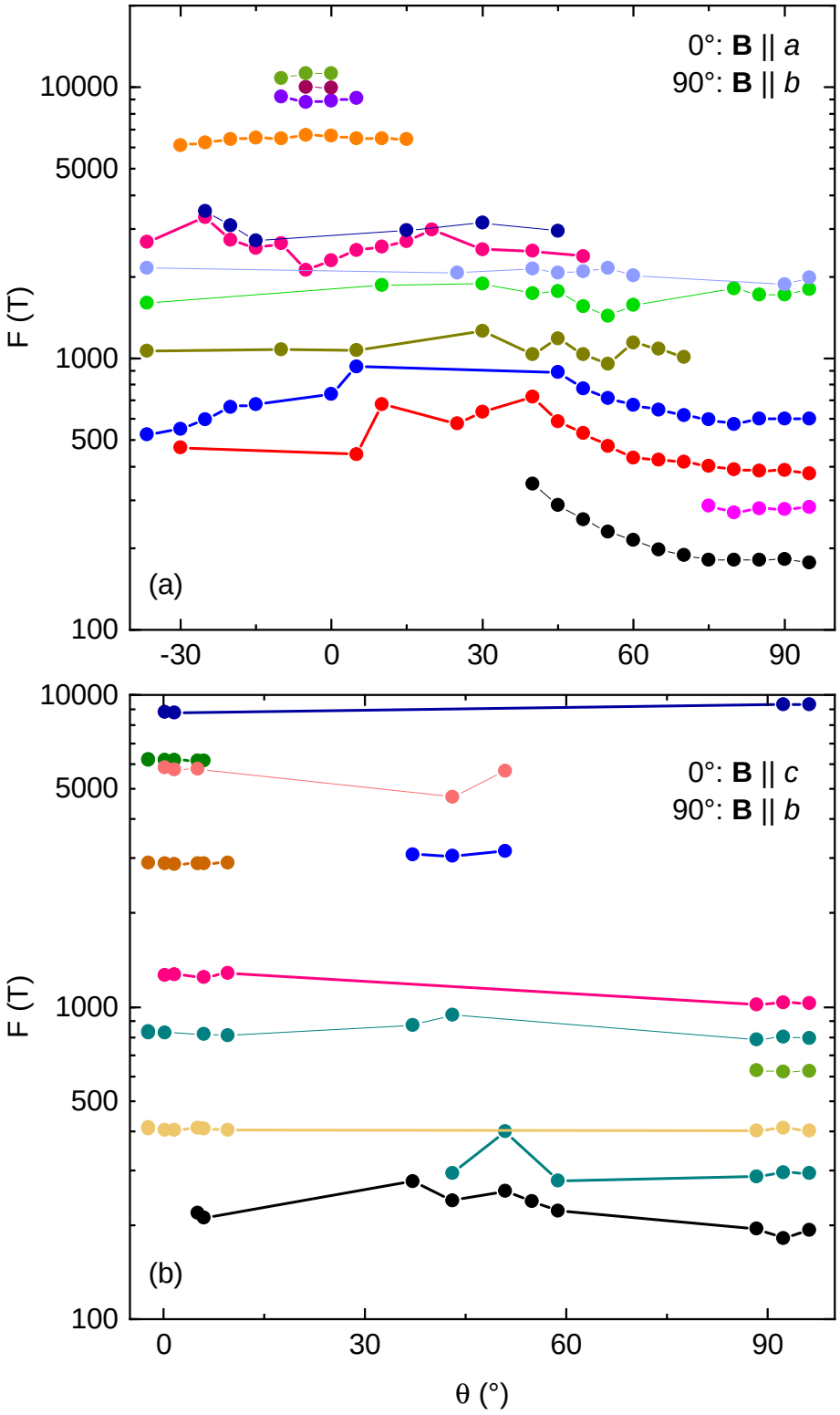

Figure 7.5: Quantum oscillation peak frequency as a function of angle for field rotated in the (a) *ab* and (b) *bc* planes. Different colors correspond to presumed different extremal Fermi surface pocket orbits in each plane, with no correspondence between (a) and (b). Note that data were taken for a smaller number of angles for (b), which is the reason for the large gaps in angle.

seems to be composed of pockets with a more spherical shape, which therefore would have minimal angular dependence.

Some of the observed peaks, especially low frequencies near 0° or 90° in Fig. 7.5, are clearly harmonics of a single fundamental. The FFTs in Fig. 7.6(d) and (g) are at the same orientation and both show peaks at 200, 400, and 600 T, which are almost certainly related. Fig 7.6(e) also has its most prominent peak at about 300 T with others appearing every multiple of 300 T above that with low amplitude. Such clear harmonics indicate low scattering rates, in line with the low residual resistivity. The presence of relatively high frequency oscillations (1 kT or more, up to 10 kT) at some angles is a sign of large area orbits. Both of these point to CoP being very conductive, with a high carrier density.

7.3.2 Temperature and Field Dependence

Temperature dependence was only done for the *a*-*b* rotation measurements, with **B** along [100], [110], and [010]. The results for some frequency bands are shown in Fig. 7.6, and the full slate of parameters is in Table 7.1. For **B** ∥ [100] and [110], only the temperature dependence of the highest amplitude peak was tracked, since the others peaks disappeared at too low of temperature for adequate fitting. For **B** ∥ [010], the effective masses of six peaks, four at low frequency and two at high frequency, were obtained. The mass of the four low frequency peaks increases with each successively higher frequency, as should be the case for harmonics of a single fundamental. In general, all effective masses were close to the electron rest mass,

indicating a lack of strong correlations. That being said, they are not substantially lower than those of CoAs. Once again calculating $\gamma = \frac{\pi N_a k_B^2}{3\hbar^2} x_i x_j \sum m^*$, where x_i and x_j are the lattice parameters in the plane perpendicular to field, the values are 2.2, 1.4, and 5.3 mJ/K^2 mol for [100], [110], and [101]-oriented fields. That the first two values are smaller than the 4.3 mJ/K^2 mol from specific heat is expected, since there are known oscillation frequencies not included. The last was computed using only the 180 and 9950 T parameters, as the other four observed peaks are either harmonics or split peaks. It is approximately equal to the direct measurement, a good indicator that there are no additional missing orbits and that the other FFT peaks do indeed correspond to harmonics.

Again, the Dingle analysis is limited to only the most prominent oscillation frequency at each angle. This is easy enough for field along [100] or [110], but for [010] the 180 T dominates. T_D values for CoP are a bit higher than most of the others calculated for FeAs and CoAs, a bit surprising given its lower residual resistivity. The calculated Γ values are 5.8×10^{12}, 4.1×10^{12}, and 6.3×10^{12} s^{-1} for $\mathbf{B} \parallel$ [100], [110], and [010] respectively. Given the relative angle insensitivity of most CoP oscillation frequencies, a spherical Fermi approximation may be more legitimate than in the case of FeAs or CoAs. The calculated ℓ values from doing so are 860, 580, and 280 Å for the same orientations. These are actually some of the longest mean free paths of the three compounds this analysis has been done far, in part because of the low masses (and in some cases high frequencies) of the orbits. This could account for why harmonics are much more visible in CoP than the two arsenides examined in previous chapters.

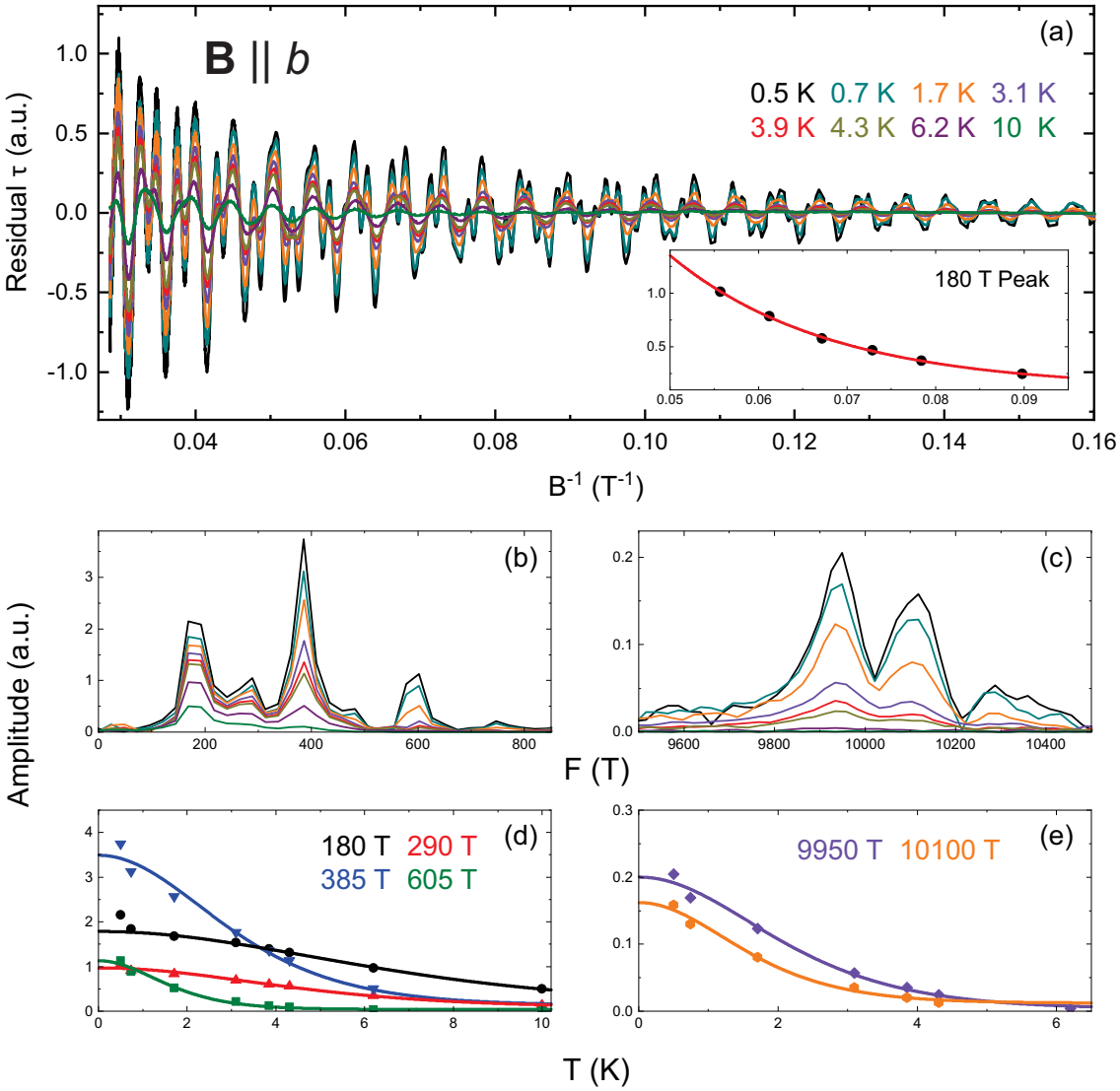

Figure 7.6: (a) Residual torque amplitude after subtraction of the nonoscillatory component for CoP at various temperatures for $\mathbf{B} \parallel b$-axis. The inset is a fit of the lowest frequency (180 T) peaks in the residual data to the Dingle factor [Eq. 2.23]. The temperature dependence of FFT amplitudes at (b) low and (c) high frequencies, with colors corresponding to the same temperatures as in (a). Peak amplitudes as a function of temperature for (d) low and (e) high frequency oscillation bands (labeled). Solid lines are fits to the Lifshitz-Kosevich factor [Eq. 2.22]

B ∥ **[hkl]**	F (T)	m^*/m_e	T_D (K)
[100]	8910	1.21	6.99
[110]	295	0.46	4.99
[010]	180	0.49	7.71
[010]	290	0.61	—
[010]	385	0.94	—
[010]	605	1.73	—
[010]	9950	1.39	—
[010]	10100	1.61	—

Table 7.1: Parameters extracted from CoP torque oscillations data with field applied in different directions. The four low frequencies for **B** ∥ [010] are likely all harmonics of the same fundamental.

7.4 CoP: Conclusions

Looking at CoP crystallizes some of the ideas that came from examining the different properties of FeAs, FeP and CoAs. It is clear that magnetic fluctuations have much less relevance to describing this material; it is not ordered, and beyond that has a much lower Wilson ratio than CoAs. Therefore any properties common to CoP and any of the other three compounds must not be related to magnetism. The high quality of CVT crystals is reflected in the low residual resistivity and significant number of harmonics seen in QO measurements. It seems then that B31 phosphides are "cleaner" than the arsenides. The lack of magnetism also indicates that it is the transition metal that plays a significant role in the presence or absence of magnetic order. On the other hand, the large, anisotropic, and nonsaturating magnetoresistance in CoP indicates that that of FeP is likely unrelated to magnetic order, and reinforces compensation, combined with the low residual resistivity, as

the most logical explanation. The linear MR of FeP at a specific angle, however, is not replicated here, another sign that the two large and linear MR have separate origins in this material class.

Future investigation into the theorized properties of CoP would be useful, especially if it could describe the Fermi surface that seems to be composed mostly of low dimensional bands that appear over only a short angular span. CoP serves an important role as a contrast to the others presented here. Investigation of the properties of this compound are a useful basis to further understand the interesting behavior stemming from this family it belongs to.

Chapter 8: $Fe_{1-x}Co_xPn$

Given the differences in the low temperature magnetic state of FeAs and FeP in comparison to CoAs and CoP, it was natural to investigate the effect of Fe-Co substitution. In the iron pnictides, chemical substitution to suppress the spin density wave is one way of stabilizing the unconventional high-temperature superconducting phase [16]. Chemical substitution, along with magnetic field or pressure, is a common way to generate the same quantum critical phase diagram. For that reason samples of both $Fe_{1-x}Co_xAs$ and $Fe_{1-x}Co_xP$ were grown and their properties measured[1].

Chemical substitution series in the B31 family have been produced before, including with magnetic end members [23,25,26,141]. In fact, the early neutron studies on CrAs, MnP, and FeP also included work on the $CrAs_{1-x}Sb_x$ series, showing a change in T_N and antiferromagnetic structure with substitution [29]. The movement from helimagnetic, orthorhombic CrAs to collinear AFM, hexagonal CrSb made things especially complicated in that case. In the case of the insulating Ru-based pnictides of P and As, it was found that with Rh doping emerged a metallic state and superconductivity, with a maximum $T_c = 3.7$ K at $x = 0.45$ in the P series [143].

[1]Growth of $Fe_{1-x}Cr_xAs$ was also attempted to look at a series in which both end members were AFM, but no pure phase crystals were obtained. A $Co_{1-x}Rh_xAs$ series produced no interesting behavior.

In this case, there was also a "pseudogap" phase that emerged at lower doping in which a superstructure (possibly from charge density wave formation) was noticed in x-ray measurements. The cuprates are the most famous example of a pseudogap material, whose temperature is heavily dependent on doping level [17]. Ru and Rh lie just below Fe and Co on the periodic table; the similarities in electron count with doping between the two are yet another reason to examine the $3d$ elements. Combined with the requirement that magnetism be at some point suppressed with lowered Fe content, Co doping on the Fe site was of high interest.

8.1 Crystal Growth

Synthesis was first attempted for the $Fe_{1-x}Co_xAs$ series. It was found that crystals grown with Bi flux were too small for transport measurements, so CVT was tried instead. For safety reasons, instead of starting with the elements, prereacted FeAs and CoAs were combined with I_2 in an evacuated quartz ampule. Since the optimal vapor transport conditions for FeAs and CoAs are slightly different, various temperatures were tried to find the best way to mix the two. The temperature at the hot end of the ampule was varied from 850-950 °C, where the lower temperature had been used for pure FeP and higher temperatures for CoP. Temperatures of at least 900 °C seemed to be better for substituted samples, as lower temperatures led to little material transporting or a large deviation from expected stoichiometry. Concentrations were checked with EDS, and all single crystal data presented here is from samples for which Co doping level was determined individually.

Often, crystals appeared at both the hot and cold ends of the CVT ampule once the growth was cooled. EDS showed that samples at the hotter end typically had a lower x than those on the cold end, and one that was substantially lower than the molar ratio of the initial mixed powders. This implies different thermodynamics for the growth of samples depending on Co concentration, and that it was easier to transport samples with more Co. This may be connected to the fact that CoP formed more easily than FeP as a powder, indicating Co reacts more readily with pnictogen atoms. The value of x for crystals from the cold end of these growths was generally close to the nominal value, with a variation (in terms of x) of about 0.05. Measurements on individual crystals produced more consistent results, indicating that the variation between samples was real and not the result of uncertainty in the EDS measurement itself.

Although CVT produced larger samples, they were still not as big as those obtained for the end members for either the phosphide or arsenide series. The small mass made heat capacity and magnetization (especially given the relatively small moments) measurements difficult. Given the variation in the Co doping level, even powder measurements or those incorporating multiple single crystals were likely to wipe out a lot of the features that were very sensitive to x value, due to the variation observed in EDS. Therefore, the only data to be presented on these series is from resistance measurements.

8.2 Transport

As seen in Chs. 4 and 5, a distinct kink in resistivity marks T_N in both FeAs and FeP, which both have a somewhat sigmoidal resistivity curve. In contrast, both of the Co compounds have a mostly featureless ρ(T). With increased Co doping, there is a continuous evolution from one form to the other, as the curves begin to look more linear. The RRR for doped samples is much lower than either parent compound, which is unsurprising, as the mixture of two kinds of transition metal on a single site should increase disorder. Inherent disorder or differing sample quality could also explain the variation in room temperature resistivity values, as does the fact that they differ by a factor of about five for the two parent compounds. The effect of substitution on scattering is most obvious in the phosphide series, where RRR can exceed 1000 for FeP but quickly falls below 10 with only a small amount of doping. [Fig. 8.1].

Notable, however, is that the kink to mark the AFM transition disappears after very little doping. In fact, it does not appear once there is more than 5% Co in either case, and instead becomes more washed out and is replaced by an inflection point. There is no way of determining from resistance alone whether the inflection point still corresponds to a magnetic transition. However, it was assumed to do so and was tracked as a function of Co concentration. This was done by looking for the maximum in $d\rho/dT$ (equivalent to the inflection point, where $d^2\rho/dT^2 = 0$). The presumed Néel temperature is suppressed by 50% Co concentration in both cases [Fig. 8.1], and takes on the linear (and at low temperature, constant) shape typical

of Co(P,As), but with much higher residual resistivity. For the arsenides, the critical doping for suppression of the inflection point is slightly lower, likely due to the fact that T_N of the pure compound is 50 K lower.

The suppression of a second order magnetic transition to zero temperature is a critical point. However, typically quantum critical points also come with resistivities that are linear in both temperature and magnetic field, due to the dominance of quantum fluctuations and loss of an internal energy scale [2, 76]. That is not the case in $Fe_{1-x}Co_xPn$. While at higher temperatures ρ(T) is linear, it still shows the same plateau at the lowest temperatures. The higher temperature behavior simply gradually looks more like CoAs, where such a dependence likely from a typical electron-phonon scattering, and the plateau is the impurity scattering baseline. Additionally, magnetoresistance is negligible for doped samples, 10% or less at 14 T and 2 K, despite being massive in the case of the phosphides and appreciable even for the arsenides. Measurements below 200 mK using adiabatic demagnetization refrigeration showed no change in resistance (i.e., no superconducting transitions). The lack of superconductivity and linearity with temperature or field demonstrate that the suppression of magnetism in the Fe-Co binaries does not lead to the same kind of quantum critical physics as in other systems.

8.3 Conclusions

Already, there were differences between the MnP-type binaries and the tetragonal, layered iron-pnictide superconductors. The arrangement of As atoms around

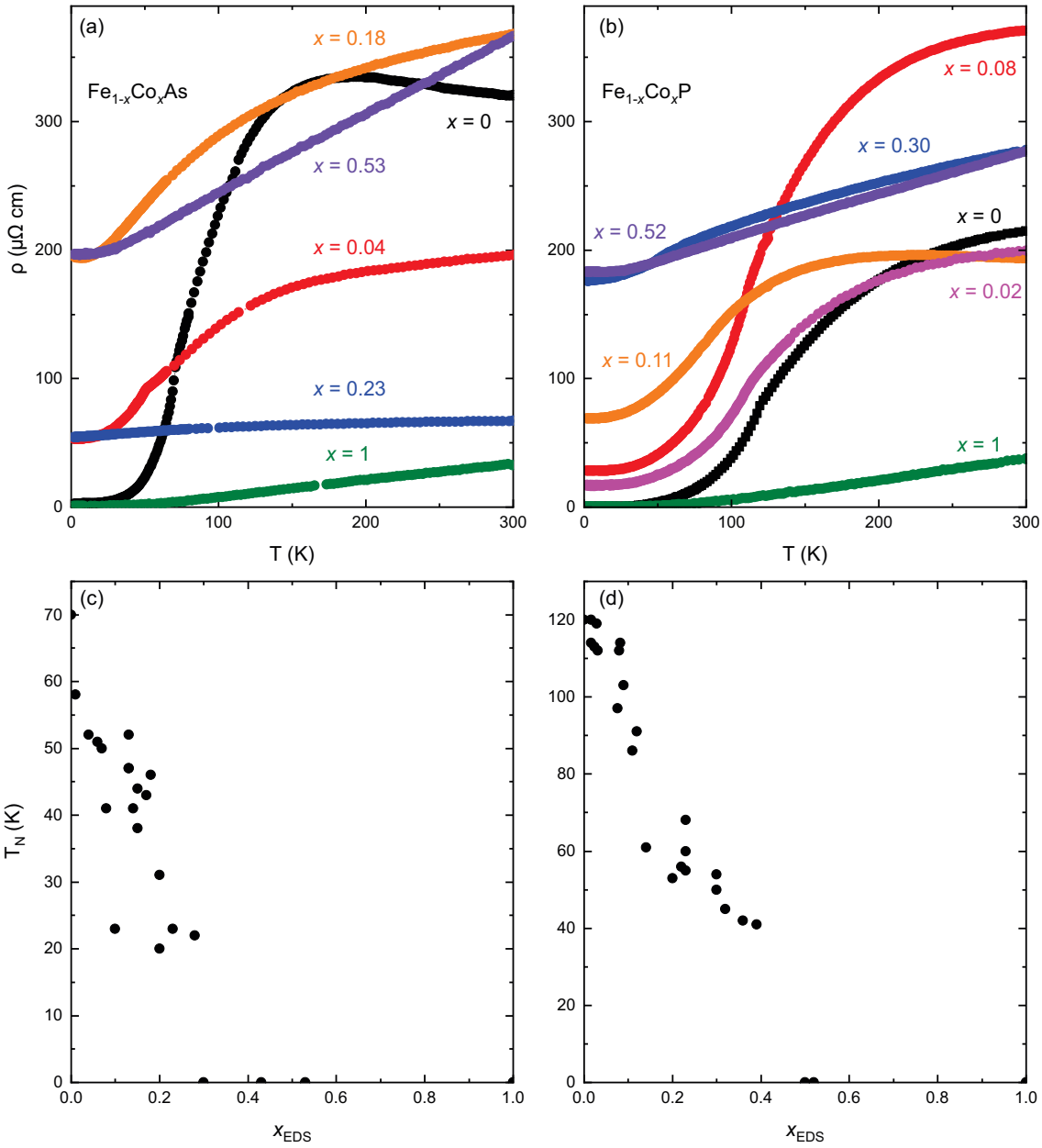

Figure 8.1: Resistivity as a function of temperature for $Fe_{1-x}Co_xAs$ (a) and $Fe_{1-x}Co_xP$ (b) with various cobalt concentrations (labeled). Below are phase diagrams of presumed T_N (based on the ρ(T) inflection point) for the (c) As and (d) P series.

the Fe atoms was different in the two systems, and pressure studies on FeAs showed no superconductivity [144]. Now, by having doped Co onto the Fe site, this difference has been reconfirmed. There is no familiar phase diagram with the suppression of AFM leading to the emergence of superconductivity [16]. While long range order is indeed suppressed, that result was unavoidable given that the Co materials are PM. At some point between 100% Fe or Co, the system has to lose its ordered state. Neutron scattering measurements could better confirm that the inflection point of the resistivity does still correspond to a magnetic transition, as it was assumed to, but may also require growths with a more consistent Co concentration. As is seen from transport, even a few percent difference in x can change the presumed T_N substantially. Such measurements could also examine if there is any change to magnetic ordering wavevector, or its strength, with doping. But the most important question was whether the AFM suppression leads to a QCP and superconducting state as in the Fe-based superconductors or CrAs, MnP, and $Ru_{1-x}Rh_x$(P,As) [19, 21, 34, 143]. The answer to that is definitively negative.

Chapter 9: Chapter 9: Conclusion

9.1 Summary of Findings

The five principal chapters of this thesis have dealt with the properties of the four possible combinations of (Fe/Co)(P/As) in the MnP-type structure, and the effect of Fe-Co substitution. In doing so, some trends have become clear.

The presence or absence of magnetic ordering is determined by the transition metal, and by extension electron number. While Fe and Co are both elemental ferromagnets, the former forms AFM compounds in this structure, and the latter PM ones. The only two other magnetic materials in this family are composed of Cr or Mn, both to the left of Fe. The Fe-Co line is the boundary between stabilizing the strong magnetic fluctuations of CoAs into an ordered state. Electron count in these materials has also been thought to determine whether hexagonal NiAs or two orthorhombic distortions (the MnP and NiP-type) is favored [22], and the topological properties of the Fermi surface [32]. This is due to the change in metal-metal bonding that occurs as more electrons are added and energy levels change. The same effect may be related to the development of long range order. As seen in Ch. 6, the band structures of CoAs and FeAs with the CoAs lattice parameters, both in the PM state, are nearly identical, indicating that the differences in ground state

magnetism are not simply a matter of unit cell size. The change in interactions or shift in the Fermi level associated with a change in valence electron number must also be considered. The $Fe_{1-x}Co_x$(P,As) substitution series showed that magnetic order is suppressed with 30-50% Co, though the distinctness of the transition vanishes at much lower levels ($< 5\%$). The disappearance of ordered magnetism does not lead to a superconducting or otherwise interesting low temperature state, in contrast to other members of this family.

On the other hand, though transition metal choice is the key to stabilizing long range order, it seems that the pnictogen element determines the strength of magnetic fluctuations. CoAs has a higher Wilson ratio than CoP, among other signs of being nearly ferromagnetic. And while T_N is higher in FeP than FeAs, the moment is much smaller than the other B31 helimagnets [Table 2.1], although at about $0.5\mu_B$ it is comparable to that of FeAs. Additionally, the linear magnetoresistance when field is applied along the c-axis indicates that it may be near the point at which the magnetic state is suppressed. A previous study showed that not only does the SDW state in FeAs survive up to 11 GPa, but that T_N changes by less than 5 K in that range [144], rather than the continuous suppression of T_N seen in MnP and CrAs [21]. Analysis of Cr-based pnictides found a continually weaker moment with lighter pnictogen atom. This was attributed to the shorter b-axis with the smaller atoms [18]. Similarly, the phosphides studied here have smaller b-axes than the arsenides, in large due to the atomic size of P compared to As.

The presence of As or P also impacts the magnetoresistance. CoP and FeP both have substantially larger MR values at high field than their arsenide coun-

terparts. The same has been found by other researchers for the Cr-based equivalents [19,112]. Based on those results and data shown here for FeP, it is possible to infer that large MR is driven by a combination of moderate electron-hole compensation and a highly anisotropic Fermi surface. However, it is clear that compensation is not perfect, since the Hall effect only shows slight nonlinearity in FeP, and the MR is still orders of magnitude smaller than in semimetals. The larger mass of the As atom may lead to a spin-orbit coupling effect that changes the band structure at the Fermi energy, as was suggested in a study of FeAs [98], and may be why theoretical predictions are unable to describe the material's behavior. The lower residual resistivities of the phosphides, 0.5 $\mu\Omega$ cm or lower at 1.8 K, indicate reduced impurity scattering, even as the temperature dependence of resistivity looks similar for materials with the same transition metal component. Given that transport behavior in field has been a key driver to claim possible quantum critical or topological physics in these materials [19,32,112], the knowledge that phosphorus is the determining element of those phenomena could be significant in pinning down the source of large MR both theoretically and experimentally, and for future study of potential topological physics in this family.

9.2 Future Directions

There are several potential paths of followup study in the metal-pnictide binaries. An obvious next step for comparison is a study of the behavior of FeP under pressure to see if helimagnetism is suppressed and a different phase emerges.

The behavior of each lattice parameter with pressure, and any structural transitions such as the one that seems to occur in CoAs under pressure [127], are a related line of investigation. The b-axis collapse accompanying the magnetic transition in CrAs [18] and negative thermal expansion of the CoAs a-axis [23] are hints that the MnP structure may have some unusual behavior under compression. The negative thermal expansion may also be a sign of changing strength of magnetic interactions. The emergence of unconventional superconductivity in CrAs and MnP under pressure makes study of magnetically and structurally similar materials of clear interest. Such work has already been done for FeAs [144], but not for FeP, CoP, or CoAs, outside of a cursory measurement at 2 GPa in the last of these that showed minimal change in resistivity. Compared to the pressure-induced superconductors, FeP has a lower magnetic ordering temperature (recall that while $T_N = 50$ K in MnP, $T_C = 291$ K) and the Co compounds do not order, meaning all may superconduct at lower pressures than were needed for the two already studied compounds.

So far, density functional theory calculations have failed to reproduce the correct low temperature magnetic state for FeAs and CoAs, and quantum oscillation measurements further indicate that the predicted Fermi surfaces, especially for FeAs, do not match experiment. More effort is clearly needed to understand the relevant interactions that must be considered so that the proper ordering is energetically favored. That may also require more precise mapping of the band structure. While quantum oscillations are a good probe, they cannot give the same clear picture that as something like angle-resolved photoemission spectroscopy. Improved band structure pictures would also help determine the influence of semi-Dirac

points, specifically their proximity to the Fermi energy, on the magnetotransport, and accordingly what role topology plays in these systems. The differences between the type of pnictogen in the structure also indicate that spin-orbit coupling, whose strength depends on atomic mass, may be relevant. Further work with other related materials that form with even heavy atoms, such as those to be covered in the Appendix, could shed light on this.

Appendix Additional MnP-Type Compounds

Beyond those covered so far in this thesis, there are a whole host of binary transition metal-pnictogen compounds. Many, including several different doping series have been characterized in depth in other works [23, 25, 26, 40, 141]. However, due to a combination of a lack of time and interest on the part of researchers, there are still some for which complete physical property reports are lacking. This section will briefly go over additional work, which was either not compelling or not complete enough for to be included as an independent section.

A.1 Rh*Pn*

There exist three Rh-based pnictogen compounds: RhAs, RhSb, and RhBi. In a report on the properties of almost all MnP- or NiAs-type transition metal arsenides, Saparov et al. specifically mention that RhAs was the only one not studied, simply saying that it was "expensive" [40]. However, interesting results have been noted in the past for Rh-based binaries. In the 1960s, RhAs and RhBi were reported to be superconductors with transition temperatures of 0.58 and 2.06 K, respectively [145]. While those are not high temperatures, only one other binary pnictide has been reported as an ambient pressure superconductors: WP, to be dis-

cussed in the next section. A much more recent study on insulating RuPn materials found that Rh substitution suppressed the metal-insulator transition and led to a superconducting dome with a maximum T_c of 1.8 K for $Ru_{1-x}Rh_xAs$ and 3.7 K for $Ru_{1-x}Rh_xP$ (note that pure RhP does not form) [143]. Furthermore, lying just below Co on the periodic table, Rh would add another layer of complexity to the near-magnetism seen in the Co-based pnictides.

A.1.1 Crystal Growth

It was found that each of RhAs, RhSb, and RhBi differ substantially in the required growth process. All three involve different fluxes. To grow single crystals of RhAs, Rh and As were first prereacted to form a binary powder. Bismuth can be used as a flux for single crystal growth; Sn flux and vapor transport were both unsuccessful. The optimal growth profile was found to be a 1:20 RhAs:Bi ratio, in which the material was heated to 1050 °C, held for 24 h, then cooled at 3 °/h to 650 °C and spun in a centrifuge. It was observed that lower spin temperatures often led to formation of $RhAs_2$. Given the lack of a Rh-As phase diagram, however, the exact temperature at which the 1:2 phase begins to form is still unknown. Samples grown in this way have a hexagonal or diamond-like shape, indicating that there is likely a higher temperature hexagonal-orthorhombic structural transition for RhAs, as there is for CoAs and other B31 compounds [22, 23].

RhSb can be grown from flux, however $RhSb_2$ begins to form at 1000 °C, thus requiring a very high spin temperature to get the 1:1 phase exclusively. Sn, Bi, and

self flux were unsuccessful, but Pb was found to work. The temperature profile used was to heat to 1160 °C, hold for 10 h, and spin at 1090 °C after very slow cooling at a rate of 1 °/h. It is likely that this temperature range could be extended to produce more crystals, with a higher max temperature (but below the melting point of the quartz ampule, about 1225 °C) and spin temperature closer to the $RhSb_2$ formation boundary.

The heaviest member of this family, RhBi, received the least thorough investigation of optimal growth conditions. However, it was found that self flux could be used to produce crystals. Rh and Bi in a 2:3 ratio can be heated to 1050 °C, held for some time, and cooled at 3 °C/h to 800 °C before being put into a centrifuge. This was intended to avoid the $RhBi_2$ formation temperature of 780 °C, however growths with this profile still had both the 1:1 and 1:2 phases. However, given the different morphology resulting from different crystal structures ($RhBi_2$ is triclinic) it is easy to separate crystals by picking through the growth. However, they were two small for any measurements beyond XRD and EDS. It is possible that a higher spin temperature or greater proportion of bismuth flux would favor the formation of exclusively RhBi in the form of large crystals.

A.1.2 Physical Properties

Resistivity as a function of temperature and field was measured for RhAs and RhSb single crystals [Fig. A.1(a)]. While ρ(300 K) differs between the two, the overall temperature dependence is similar, being primarily linear until low temper-

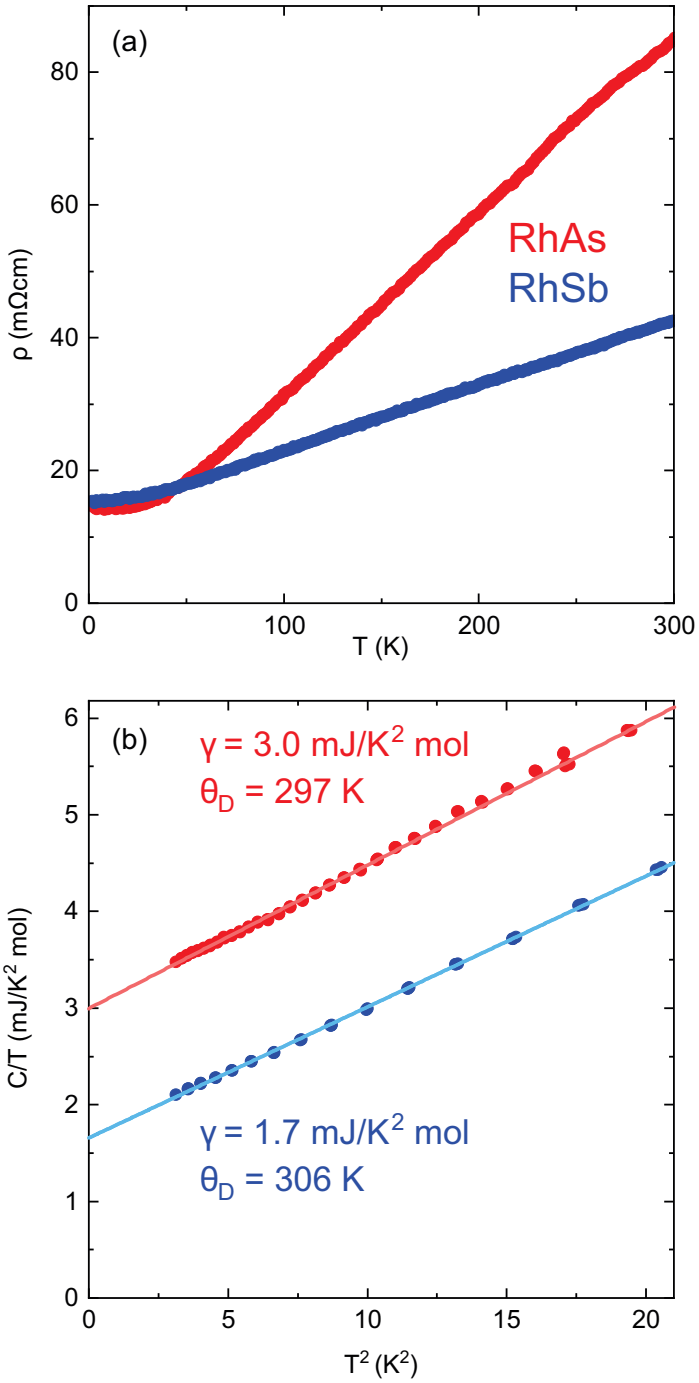

Figure A.1: (a) Resistivity in zero field as a function of temperature for RhAs and RhSb single crystals. (b) Specific heat of two single crystal samples of RhAs and RhSb. Lines are fits to the Debye low temperature model with obtained parameters from those fits next to the data.

ature saturation, much like CoAs and CoP. RRR values were low, below five for all measured samples and lower in RhSb. This may be related to overall molar mass, as it was seen that phosphide samples had consistently higher RRRs among the $3d$ pnictides. It could also be due to the fact that not as much time was invested in perfecting growth conditions. In line with the low RRR, MR was very small in comparison to other *Pnma* binaries, reaching values of about 3% in both compounds at 9 T.

No superconducting transition was found to temperatures below 200 mK using an ADR for RhAs, in contrast to the report of Ref. [145]. The explanation for this could be that other compounds mentioned in that work have similar elemental ratios and T_c values to the MnP-type binaries; if samples of those materials were slightly off stoichiometry, they could have been confused for the 1:1 materials and also have had a slight change in transition temperature. RhBi was also reported as a superconductor in that paper. Whether it really is, or suffers from the same misidentification problem as RhAs, ought to be pursued.

Heat capacity data fit well below about 20 K^2 (4.5 K) to the Debye low temperature specific model (3.1) [Fig. A.1]. Values of the Sommerfeld coefficient are 3.0 and 1.7 mJ/K^2 mol for RhAs and RhSb, respectively. These are both a bit smaller than in the $3d$-based materials, which is perhaps related to the higher residual resistivity and indicative of smaller Fermi surface pockets and poorer conduction. It is also a sign that increasing the mass of the transition metal atom does not significantly affect electron correlations, which would increase γ. The Debye temperatures are 297 K and 306 K for the As and Sb compound are also slightly lower than has

been seen so far.

A.1.3 Conclusions

While preliminary, there is no indication of ordered magnetism or superconductivity in the Rh-based pnictides. Of course, more effort to synthesize RhBi would determine whether that material is a superconductor as reported, or was misidentified as seems to be the case for RhAs. The movement to the $4d$ transition metal block should increase the spin-orbit coupling strength, thought to be influential in the band structure of some MnP-type materials [32, 98]. The decrease in the Sommerfeld coefficient in RhAs and RhSb is a sign that there is no great enhancement in correlated electron behavior.

A.2 WP

Having established that RhAs is not a superconductor down to 0.1 K, it seems that WP the only MnP-type parent compound to superconduct at ambient pressure. It was in fact only recently discovered, with T_c reported to be 0.8 K [33]. As mentioned in the Introduction, superconductivity in a nonsymmorphic space group is interesting on its own, due to potential associations with topological physics. Previous study on WP is scant, but the lack of any transition in resistivity, and the elemental composition, indicate that ordered magnetism is unlikely, as opposed to the results for superconducting CrAs and MnP. Attempts were made to look at more of the basic properties of WP.

A.2.1 Crystal Growth and Characterization

In the only previous extensive work on single crystal WP, samples were grown by I_2 chemical vapor transport using prereacted WP powder [33]. However, the suspicion was that this was not optimal for two reasons. First, in FeP samples had a much lower residual resistivity when grown directly from the elements, as opposed to powder. Second, the vastly different melting temperatures of W (3422 °C) and P (590 °C in the less volatile red form) foretell that it will be very difficult to get them to react well. Thus inspiration for CVT growth was taken from an earlier work that used the oxides of heavy transition metals (Hf, Ta, W, and others) to produce single crystal transition metal phosphides with CVT [88]. WO_3 has a lower melting point (1473 °C), and it is also thought that the release of oxygen contributes to gas phase transport, along with I_2.

WO_3 and red P powders were ground together and placed into a quartz tube in a 1:1 ratio of W:P, with additional I_2. The reactants were placed in the middle of a furnace at 900-1000 °C with the cold end at the edge of the furnace and left for 10-14 days, similar to other CVT growths already covered. After that time, it was found that powder remained at the hot end, while a mixture of material was at the cold end [Fig. A.2]. X-ray diffraction of the powder showed that it was WP, while the cold end was a mixture of WP single crystals, which were black and shiny, and larger, red-tinged chunks of what was identified by XRD as $W_8P_4O_{32}$ (which can also be written as $W_2O_4[PO_4]$). Often the WP crystals were found fused to the $W_8P_4O_{32}$, but could easily be polished to leave just the desired material. Lattice

parameters were $a = 5.73$ Å, $a = 3.25$ Å, and $c = 6.22$ Å, very close to previous reports [33, 146].

As is the case with most of the other materials covered so far, CVT-grown crystals generally grew along the b-axis, the shortest crystallographic direction. They were, however, more platelike than the needlelike crystals reported by Liu et al. [33] This enabled proper alignment of the samples for investigation of anisotropy in the orthorhombic system, and facilitated Hall measurements (which require a wide enough face to place two opposing voltage leads). The naturally flat faces perpendicular to the long growth axis were typically either the a-axis or (101).

EDS on WP showed a similar pattern to FeP grown directly from the elements. Again, there was an excess transition metal content, with consistently about 53-55% W (and thus 47-45% P). The prior study reported an EDS-derived composition of exactly 1:1 [33], which may account for some of the differences in behavior that will be shown in the next section. As with FeP, a slight change in stoichiometry may change the density of scattering sites or the Fermi level location, both of which could subsequently affect other properties.

A.2.2 Normal State Properties

The increased crystal size enabled several kinds of measurements on WP in the normal state. The resistivity has an almost perfectly linear dependence at high temperature, before plateauing down to 1.8 K [Fig. A.3(a)]. This is similar to what was previously seen, however crystals grown by the new WO_3 method have

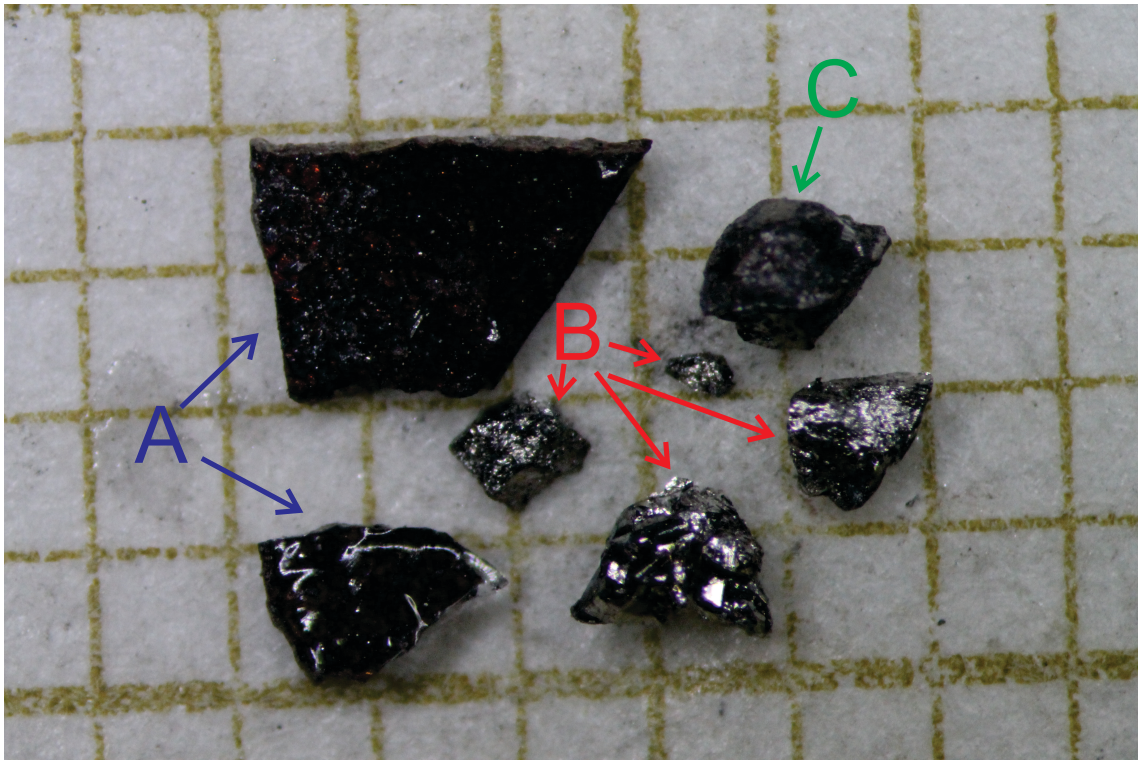

Figure A.2: The different materials that form at the cold end of a sealed quart ampule when starting with WO_3, P, and I_2 at the hot end. Pieces marked A are chunks of $W_8P_4O_{32}$, those marked B are WP (either single crystals, or multiple crystals intergrown), and C is a piece of WP fused to a piece of $W_8P_4O_{32}$. All three were commonly found in these growths.

substantially lower residual resistivity than those grown from WP polycrystals. This, as noted, parallels what was seen in FeP, which also had nonstoichiometric EDS results. The RRR could be several hundred, with ρ_0 as low as 0.25 $\mu\Omega$ cm. The suspicion, as mentioned, is that WP are not able to form a high quality powder to their vastly different states at temperatures of roughly 800 °C under which powders are typically prepared. Magnetoresistance becomes significant around 50 K, about the same temperature as for FeP and other "turn on" materials [58, 112]. A field of 9 T is enough to cause an upturn in the resistivity with further cooling, with the minimum coming at 35 K.

The large magnetoresistance made it difficult to get a clear Hall signal due to corruption of the symmetric component. Thus, it cannot yet be determined whether the Hall resistivity is linear up to 14 T. However, temperature sweeps were made at ±14 T with $\mathbf{B} \parallel [101]$, with the difference at the two field extremes used to calculate a slope, which implicitly assumes a linear Hall resistivity [Fig. A.3(b)]. Conduction is electron-dominated at all temperatures, but there is a clear temperature dependence to R_H, including a peak at 130 K. Given the presence of the MR "turn on" temperature, it is likely that multiple bands of both carrier types, with differing mobilities, are present in WP. However, there is no clear, interesting behavior below 50 K, in the vicinity of the increase in MR. If taken as a carrier density, R_H corresponds to $n \approx 10^{22}$ cm^{-3}, indicating a large number of carriers, as there should be in such a good metal.

The low temperature specific heat also differs from the previous report [Fig. A.3(c)]. The data, while they can be fit decently by the Debye low tem-

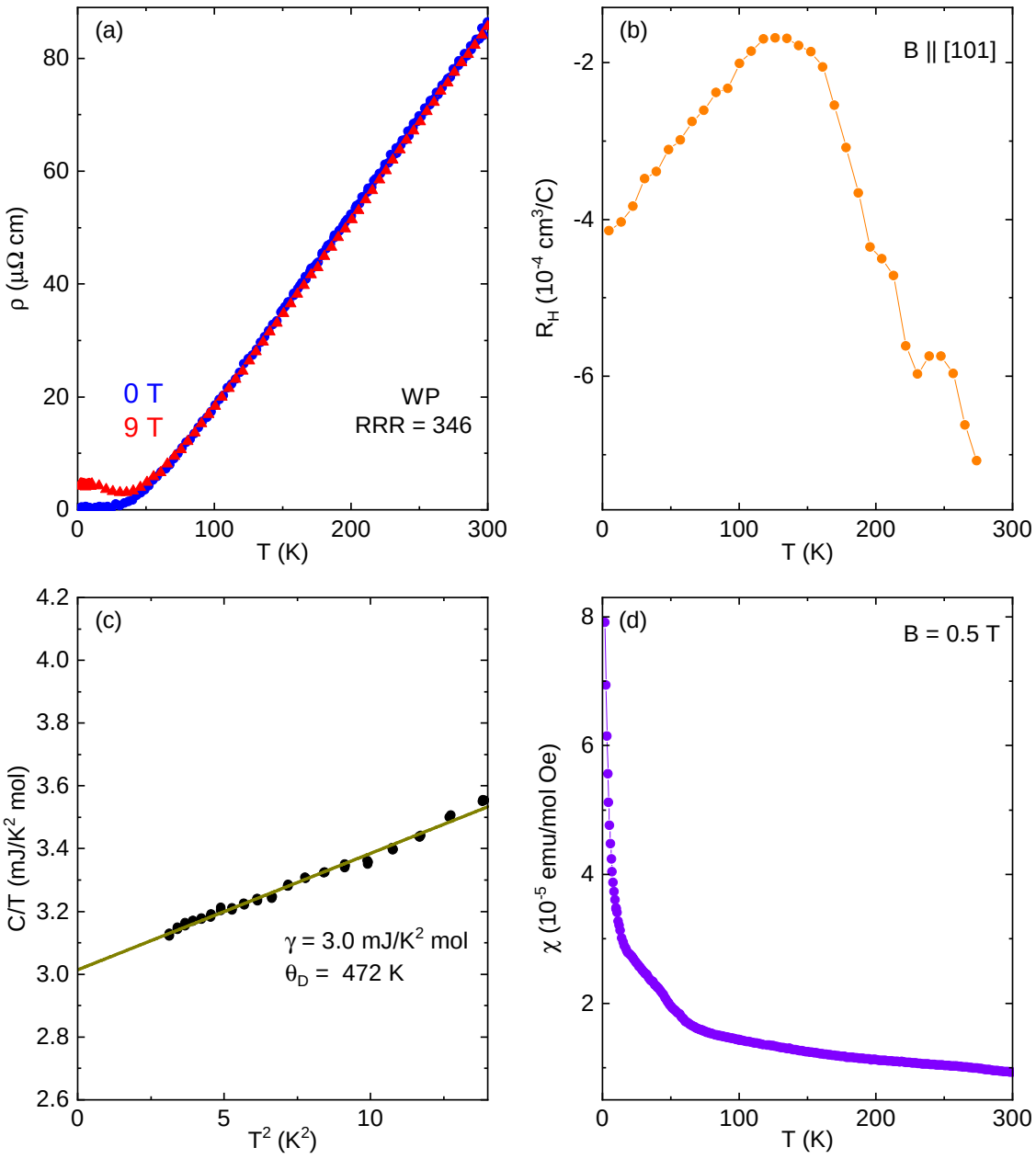

Figure A.3: (a) Resistivity as a function of temperature for a WP single crystal with current along the b-axis, in zero field and with field along the [101] direction. (b) Hall coefficient (based on temperature sweeps in ± 14 T) for a WP single crystal with field along [101]. (c) Low temperature specific heat of a different WP single crystal. The green line is a fit to the Debye model, with extracted parameters noted. (d) Magnetization of WP powder as a function of temperature. Data shown is field cooled, but there was no difference with zero field cooling.

perature model, are not smooth down to 1.8 K. This may be experimental error, or could be from some other contribution to the specific heat, such as the magnetic fluctuations seen in CoAs-not enough measurements were done to be certain. Regardless, the extracted γ value of 3.0 $\frac{\text{mJ}}{\text{mol K}^2}$ is lower than most of the other binary pnictides presented. However, the value is still twice that reported for the needlelike samples [33]. As speculated, a change in W:P ratio may also change the Fermi level, and therefore the density of states at E_F. If that is the source of the increase in γ, it would also account for superior low temperature conductivity in oxide-grown samples.

The magnetic susceptibility of a WP single crystal was also measured [Fig. A.3(d)]. Data shown are only for zero field cooling in low field, but no difference was seen with field cooling or higher fields. There is some noise and jumpiness in the data, due to the small moment against the large background of the sample holder. WP has generally paramagnetic behavior, with increasing χ with cooling. However, the change is very small across 300 K, only about 6% of the 300 K value. As suspected, there are no signs of strong magnetic fluctuations in this material.

Two WP samples were also brought to the 41.5 T resistive magnet at the NHMFL for temperature dependent measurements. One was only measured at low temperatures, 0.4-3 K, with field along the *a*-axis [Fig. A.4(a)]. It showed a quasilinear dependence on field, but with two distinct regions of slope that crossed over at about 20 T (green and red lines). Data were nearly identical across all measured temperatures. The second samples had its [011] axis aligned with the field, and data were taken over a wider temperature range, allowing the drop in MR

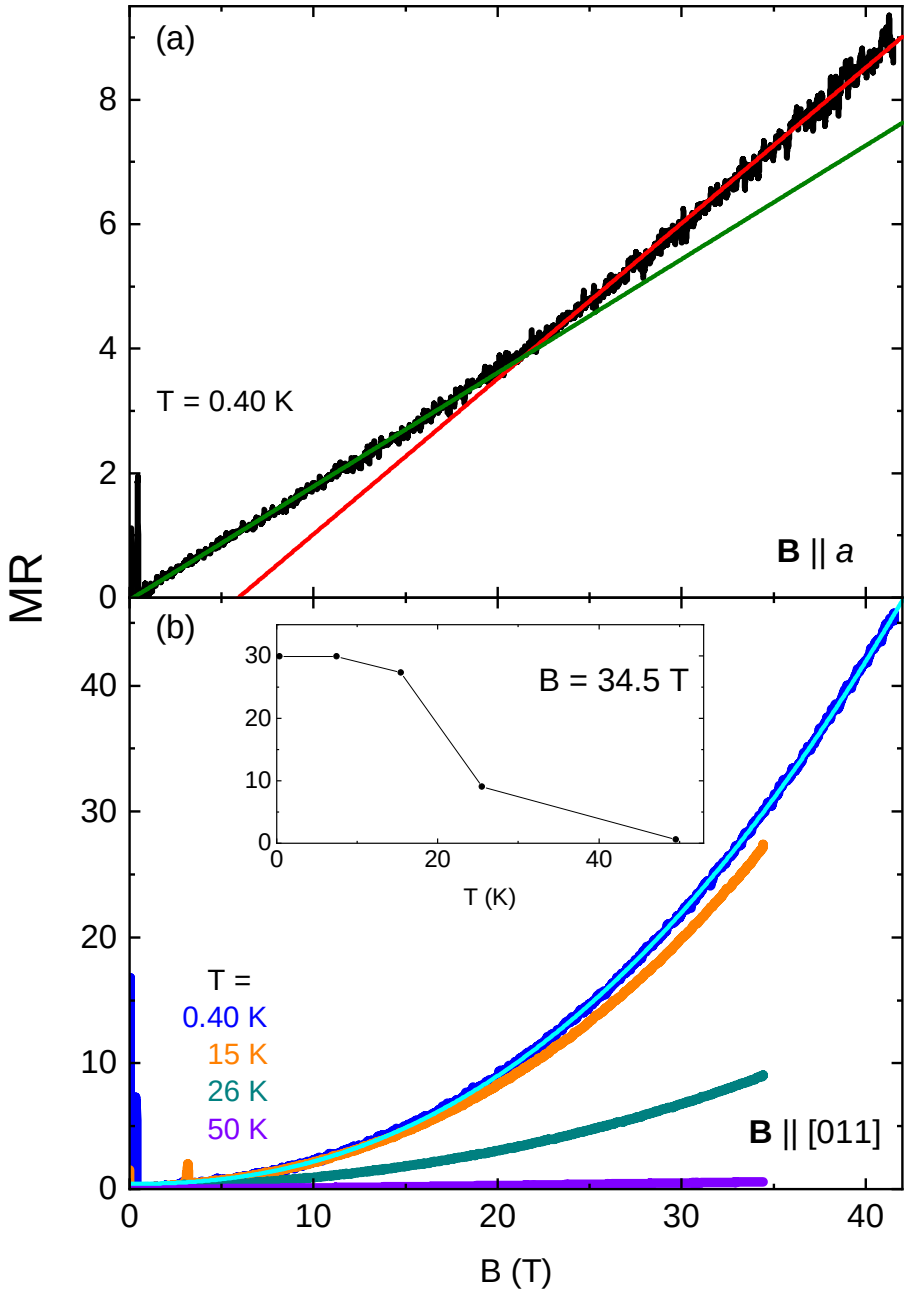

Figure A.4: (a) Magnetoresistance of a WP sample with $\mathbf{B} \parallel a$-axis at 0.39 K up to 41.5 T. Data up to 3 K looked identical. Low field blips come from errors associated with the superconducting transition and low resistance electronics. The green and red lines are linear fits to low and high field data, respectively. (b) Magnetoresistance of a different WP crystal with $\mathbf{B} \parallel [011]$ at multiple temperatures. Data did not vary from base temperature to 8 K, and the next lowest temperature was 15.4 K. The light blue line is a power law fit of the base temperature data, yielding $n = 2.27$. The inset shows MR at 34.5 T (the highest field obtained at higher temperature) as a function of temperature, including a 7.49 K data point not shown in the main graphic.

with increasing temperature to be seen [Fig. A.4(b)]. Due to issues with magneti power supplies, the field range was limited to 34.5 T for higher temperatures. The field dependence is much better fit by a higher order power law in this case, yielding $n = 2.27$ for the lowest temperature data. The MR is also much larger in this orientation, reaching a value of about 45 for 0.39 K, compared to only 9 for the other sample at the same temperature. This also seems similar to FeP, where the direction of smaller MR also shows more linear behavior. However, in this case that is the a-axis. Of course, more extensive angular dependence was not performed to see how the value with field at other orientations compares, and it may be the case that MR is even smaller for another direction. The inherent anisotropy, however, is evident from these data, which make an excellent case for further study with a rotating probe. No quantum oscillations were observed in either sample, but this may be due to the overall noisier appearance of the data, and they may be more obvious in magnetic torque measurements, as has been the case for other B31 materials.

A.2.3 Superconducting Properties

Measurements below 1.8 K were made with a He3 insert to the PPMS, except in the case of one sample where zero field temperature sweeps were also acquired with an ADR. WP samples grown from WO_3 and P do indeed superconduct at low temperature, but with some differences from the prior report. A sample with a higher residual resistivity (1.5 $\mu\Omega$ cm) had a very sharp zero field transition at 0.85 K,

similar to what has been reported [33]. However, three samples with lower residual resistivities showed broader transitions, but at higher temperatures [Fig. A.5(a); note that the lower T_c sample has had ρ reduced by a factor of 10]. The data for these samples are much noisier, for two reasons. First of all, the residual resistivities are an order of magnitude lower. Secondly, the three higher RRR, higher T_c samples were platelike, whereas the single low T_c samples was needlelike, like those of Liu et al [Fig. A.5(b)]. While the platelike samples could be polished to try to maximize resistance, this could not be done to the extreme degrees of needlelike samples (an as-grown length over 1 mm, and a thickness of less than 50 μm). As a result they hit up against the PPMS noise floor. Nevertheless, with enough averaging of the data there is a clear transition from zero to nonzero resistance, with the zero coming close to 1.0 K for all three samples. A concern given the low upper critical field of WP is residual flux in the magnet, which can change T_c and also broaden superconducting transitions. However, magnetic field was oscillated to zero above T_c for all samples, and the low T_c sample was measured simultaneously with a high T_c one with a similar current, indicating that the broadness is an inherent feature of the sample.

The upper critical field is, like T_c, increased in the platelike samples. In the case of samples A and B, measured together, 200 mT is still enough to suppress the transition below 0.5 K, though there may still be a slight dip in the data for B [Fig. A.5(c)]. A plot of B_{c2} vs. T_c is complicated by the broadness of the transitions, so the initial dip of the resistance from its plateau value is used [Fig. A.5(d)]. For two samples, A and C, measured in the same orientation, it is clear that the higher

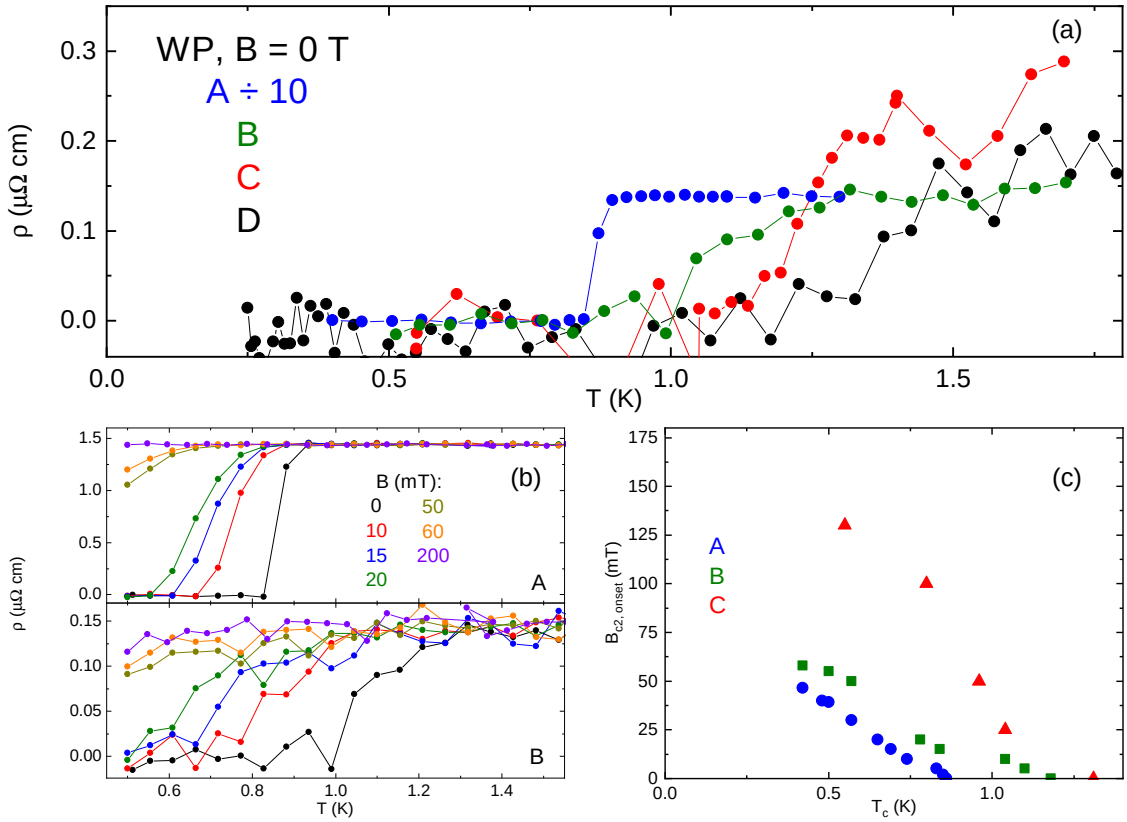

Figure A.5: (a) Zero field temperature sweeps, showing superconducting transitions, of four different WP single crystals. Sample A has had its resistivity reduced 10 times to fit on the scale. (b) Temperature sweeps in field for WP samples (top) A and (bottom) B, measured simultaneously. (c) Upper critical field as a function of temperature for WP crystals A, B, and C, based on the onset of the superconducting transition, judged by the initial dip in resistivity. A and C have $\mathbf{B} \parallel c$-axis, for B the orientation is unknown.

T_c results in a much higher critical field. Furthermore, in the case of sample A, B_{c2} is roughly three times larger than for samples with a similar T_c. This may also be attributable to the improved RRR (while lower than other samples, it is still higher than those of Liu et al.). It may also be due to a different orientation, as in the previous study the axis parallel to field was not know.

A.2.4 Conclusions

It is obvious that growth method plays a significant role in determining the behavior of WP. Vapor transport growth using WO_3 and elemental P produces much better quality samples that WP polycrystalline starting material, based on residual resistivity. These samples also seem to have higher superconducting transition temperatures, though that seems to be also linked to sample morphology, with a lower T_c seen in a platelike sample reminiscent of that grow by the alternate technique. The dependence of T_c on sample purity is an indicator of unconventional superconductivity, and an obviuos motivator for further study of the only ambient pressure superconducting parent compound in the MnP series.

Bibliography

[1] D. J. Campbell, Z. E. Brubaker, C. Roncaioli, P. Saraf, Y. Xiao, P. Chow, C. Kenney-Benson, D. Popov, R. J. Zieve, J. R. Jeffries, and J. Paglione, "Pressure-Driven Valence Increase and Metallization in Kondo Insulator $Ce_3Bi_4Pt_3$," *arXiv:1907.09017*, 2019.

[2] Y. Nakajima, T. Metz, C. Eckberg, K. Kirshenbaum, A. Hughes, R. Wang, L. Wang, S. R. Saha, I.-L. Liu, N. P. Butch, D. J. Campbell, Y. S. Eo, D. Graf, Z. Liu, S. Borsenko, P. Y. Zavalij, and J. Paglione, "Planckian dissipation and scale invariance in a quantum-critical disordered pnictide," *arXiv:1902.01034*, 2019.

[3] C. Eckberg, D. J. Campbell, T. Metz, J. Collini, H. Hodovanets, T. Drye, P. Zavalij, M. H. Christensen, R. M. Fernandes, S. Lee, P. Abbamonte, J. Lynn, and J. Paglione, "Sixfold enhancement of superconductivity in a tunable electronic nematic system," *Nat. Phys.*, 2019.

[4] S. Ran, I.-L. Liu, Y. S. Eo, D. J. Campbell, P. Neves, W. T. Fuhrman, S. R. Saha, C. Eckberg, H. Kim, J. Paglione, D. Graf, J. Singleton, and N. P. Butch, "Extreme magnetic field-boosted superconductivity," *Nat. Phys.*, 2019.

[5] R. L. Stillwell, X. Wang, L. Wang, D. J. Campbell, J. Paglione, S. T. Weir, Y. K. Vohra, and J. R. Jeffries, "Observation of two collapsed phases in $CaRbFe_4As_4$," *Phys. Rev. B*, vol. 100, p. 045152, 2019.

[6] D. J. Campbell, C. Eckberg, P. Y. Zavalij, H.-H. Kung, E. Razzoli, M. Michiardi, C. Jozwiak, A. Bostwick, E. Rotenberg, A. Damascelli, and J. Paglione, "Intrinsic insulating ground state in transition metal dichalcogenide $TiSe_2$," *Phys. Rev. Mater.*, vol. 3, no. 5, p. 053402, 2019.

[7] S. Lee, G. De La Peña, S. X.-L. Sun, M. Mitrano, Y. Fang, H. Jang, J.-S. Lee, C. Eckberg, D. Campbell, J. Collini, J. Paglione, F. de Groot, and P. Abbamonte, "Unconventional Charge Density Wave Order in the Pnictide Superconductor $Ba(Ni_{1-x}Co_x)_2As_2$," *Phys. Rev. Lett.*, vol. 122, no. 14, p. 147601, 2019.

[8] Z. E. Brubaker, R. L. Stillwell, P. Chow, Y. Xiao, C. Kenney-Benson, R. Ferry, D. Popov, S. B. Donald, P. Söderlind, D. J. Campbell, J. Paglione, K. Huang, R. E. Baumbach, R. J. Zieve, and J. R. Jeffries, "Pressure-dependent intermediate valence behavior in $YbNiGa_4$ and $YbNiIn_4$," *Phys. Rev. B*, vol. 98, p. 214115, 2018.

[9] H. Hodovanets, C. J. Eckberg, P. Y. Zavalij, H. Kim, W.-C. Lin, M. Zic, D. J. Campbell, J. S. Higgins, and J. Paglione, "Single-crystal investigation of the proposed type-II Weyl semimetal CeAlGe," *Phys. Rev. B*, vol. 98, p. 245132, 2018.

[10] C. Eckberg, L. Wang, H. Hodovanets, H. Kim, D. J. Campbell, P. Zavalij, P. Piccoli, and J. Paglione, "Evolution of structure and superconductivity in $Ba(Ni_{1-x}Co_x)_2As_2$," *Phys. Rev. B*, vol. 97, no. 22, p. 224505, 2018.

[11] D. J. Campbell, L. Wang, C. Eckberg, D. Graf, H. Hodovanets, and J. Paglione, "CoAs: The line of $3d$ demarcation," *Phys. Rev. B*, vol. 97, p. 174410, 2018.

[12] B. Wilfong, X. Zhou, H. Vivanco, D. J. Campbell, K. Wang, D. Graf, J. Paglione, and E. Rodriguez, "Frustrated magnetism in the tetragonal CoSe analog of superconducting FeSe," *Phys. Rev. B*, vol. 97, p. 104408, 2018.

[13] D. J. Campbell, C. Eckberg, K. Wang, L. Wang, H. Hodovanets, D. Graf, D. Parker, and J. Paglione, "Quantum oscillations in the anomalous spin density wave state of FeAs," *Phys. Rev. B*, vol. 96, p. 075120, 2017.

[14] C. K. H. Borg, X. Zhou, C. Eckberg, D. J. Campbell, S. R. Saha, J. Paglione, and E. E. Rodriguez, "Strong anisotropy in nearly ideal tetrahedral superconducting fes single crystals," *Phys. Rev. B*, vol. 93, p. 094522, 2016.

[15] Y. Kamihara, T. Watanabe, M. Hirano, and H. Hosono, "Iron-based layered superconductor $LaO_{1-x}F_xFeAs$ (x = 0.05-0.12) with T_c= 26 K," *J. Am. Chem. Soc.*, vol. 130, no. 11, pp. 3296–3297, 2008.

[16] J. Paglione and R. L. Greene, "High-temperature superconductivity in iron-based materials," *Nat. Phys.*, vol. 6, no. 9, p. 645, 2010.

[17] D. Rybicki, M. Jurkutat, S. Reichardt, C. Kapusta, and J. Haase, "Perspective on the phase diagram of cuprate high-temperature superconductors," *Nat. Commun.*, vol. 7, p. 11413, 2016.

[18] W. Wu, J. Cheng, K. Matsubayashi, P. Kong, F. Lin, C. Jin, N. Wang, Y. Uwatoko, and J. Luo, "Superconductivity in the vicinity of antiferromagnetic order in CrAs," *Nat. Commun.*, vol. 5, p. 5508, 2014.

[19] Q. Niu, W. Yu, K. Yip, Z. Lim, H. Kotegawa, E. Matsuoka, H. Sugawara, H. Tou, Y. Yanase, and S. K. Goh, "Quasilinear quantum magnetoresistance in

pressure-induced nonsymmorphic superconductor chromium arsenide.," *Nat. Commun.*, vol. 8, p. 15358, 2017.

[20] J.-G. Cheng, K. Matsubayashi, W. Wu, J. Sun, F. Lin, J. Luo, and Y. Uwatoko, "Pressure induced superconductivity on the border of magnetic order in MnP," *Phys. Rev. Lett.*, vol. 114, no. 11, p. 117001, 2015.

[21] J. Cheng and J. Luo, "Pressure-induced superconductivity in CrAs and MnP," *J. Phys.-Condens. Mat.*, vol. 29, no. 38, p. 383003, 2017.

[22] W. Tremel, R. Hoffmann, and J. Silvestre, "Transitions between NiAs and MnP type phases: an electronically driven distortion of triangular (3^6) nets," *J. Am. Chem. Soc.*, vol. 108, no. 17, pp. 5174–5187, 1986.

[23] K. Selte, A. Kjekshus, A. F. Andresen, Å. Pilotti, S. Svensson, and C. G. Swahn, "Phase Transitions Between the MnP and NiAs Type Structures," *Acta Chem. Scand.*, vol. 27, no. 9, pp. 3195–3206, 1973.

[24] K. Selte, A. Kjekshus, and A. F. Andresen, "Magnetic structure and properties of FeAs," *Acta Chem. Scand.*, vol. 26, no. 8, pp. 3101–3113, 1972.

[25] K. Selte, H. Fjellvag, A. Kjekshus, and A. F. Andresen, "Magnetic Structures and Properties of $Cr_{1-t}Fe_tAs$," *Acta Chem. Scand.*, vol. 33, no. 10, pp. 727–731, 1979.

[26] K. Selte, A. Kjekshus, and T. A. Oftedal, "On the Structural and Magnetic Properties of $V_{1-t}Fe_tAs$," *Acta Chem. Scand.*, vol. 28, no. 7, 1974.

[27] K. Selte, A. Kjekshus, and A. Andresen, "Structural and Magnetic Properties of FeP," *Acta Chem. Scand.*, vol. 26, no. 3, pp. 1276–1277, 1972.

[28] K. Selte and A. Kjekshus, "Structural and magnetic properties of CoAs," *Acta Chem. Scand.*, vol. 25, no. 9, pp. 3277–3284, 1971.

[29] A. Kallel, H. Boller, and E. F. Bertaut, "Helimagnetism in MnP-type compounds: MnP, FeP, CrAs and $CrAs_{1-x}Sb_x$ mixed crystals," *J. Phys. Chem. Solids*, vol. 35, no. 9, pp. 1139–1152, 1974.

[30] D. Gonzalez-Alvarez, F. Grønvold, B. Falk, E. F. Westrum, R. Blachnik, and G. Kudermann, "FeAs: Heat capacity, enthalpy increments, other thermodynamic properties from 5 to 1350 K, and magnetic transition," *J. Chem. Thermodyn.*, vol. 21, no. 4, pp. 363 – 373, 1989.

[31] B. Westerstrandh, L. Lundgren, U. Gäfvert, and B. Carlsson, "Magnetic susceptibility resistivity and thermal expansion measurements on FeP," *Phys. Scripta*, vol. 15, no. 4, p. 276, 1977.

[32] G. Cuono, F. Forte, M. Cuoco, R. Islam, J. Luo, C. Noce, and C. Autieri, "Multiple band-crossings and Fermi surface topology: role of double nonsymmorphic symmetries in MnP-type crystal structures," *arXiv:1905.04675*, 2019.

[33] Z. Liu, W. Wu, Z. Zhao, H. Zhao, J. Cui, P. Shan, J. Zhang, C. Yang, P. Sun, Y. Wei, S. Li, J. Zhao, Y. Sui, J. Cheng, L. Lu, J. Luo, and G. Liu, "Superconductivity in WP single crystals," *Phys. Rev. B*, vol. 99, p. 184509, 2019.

[34] H. Kotegawa, S. Nakahara, H. Tou, and H. Sugawara, "Superconductivity of 2.2 K under pressure in helimagnet CrAs," *J. Phys. Soc. Jpn.*, vol. 83, no. 9, p. 093702, 2014.

[35] N. Mathur, F. Grosche, S. Julian, I. Walker, D. Freye, R. Haselwimmer, and G. Lonzarich, "Magnetically mediated superconductivity in heavy fermion compounds," *Nature*, vol. 394, no. 6688, p. 39, 1998.

[36] S. Rundqvist, "Phosphides of the B31 (MnP) structure type," *Acta Chem. Scand*, vol. 16, no. 2, pp. 287–292, 1962.

[37] K. Selte, A. Kjekshus, W. E. Jamison, A. F. Andresen, and J. Engebretsen, "Magnetic structure and properties of CrAs," *Acta Chem. Scand.*, vol. 25, no. 5, pp. 1703–1714, 1971.

[38] R. H. Wilson and J. S. Kasper, "The crystal structure of MnAs above 40 °C," *Acta Crystallogr.*, vol. 17, no. 2, pp. 95–101, 1964.

[39] H. Kandler and B. Reiss, "Zur Kristallstruktur der intermetallischen Phasen MoAs und Mo_5As_4," *Z. Naturforsch.*, vol. 21, no. 5, pp. 549–554, 1966.

[40] B. Saparov, J. E. Mitchell, and A. S. Sefat, "Properties of binary transition-metal arsenides (TAs)," *Supercond. Sci. Tech.*, vol. 25, no. 8, p. 084016, 2012.

[41] K. Endresen, S. Furuseth, K. Selte, A. Kjekshus, T. Rakke, and A. F. Andresen, "MnP Type Structure of RuSb and RhSb," *Acta Chem. Scand.*, vol. 31, no. 4, pp. 249–252, 1977.

[42] S. Blundell, *Magnetism in Condensed Matter*. Oxford, United Kingdom: Oxford University Press, 2003.

[43] N. W. Ashcroft and N. D. Mermin, *Solid State Physics*. Orlando, Florida: Saunders College Publishing, 1976.

[44] H. Kotegawa, K. Matsushima, S. Nakahara, H. Tou, J. Kaneyoshi, T. Nishiwaki, E. Matsuoka, H. Sugawara, and H. Harima, "Superconductivity and magnetic fluctuations developing in the vicinity of strong first-order magnetic transition in CrAs," *J. Phys.: Condens. Mat.*, vol. 29, no. 23, p. 234002, 2017.

[45] M. S. Reis, R. M. Rubinger, N. A. Sobolev, M. A. Valente, K. Yamada, K. Sato, Y. Todate, A. Bouravleuv, P. J. von Ranke, and S. Gama, "Influence of the strong magnetocrystalline anisotropy on the magnetocaloric properties of MnP single crystal," *Phys. Rev. B*, vol. 77, p. 104439, 2008.

[46] E. E. Rodriguez, C. Stock, K. L. Krycka, C. F. Majkrzak, P. Zajdel, K. Kirshenbaum, N. P. Butch, S. R. Saha, J. Paglione, and M. A. Green, "Noncollinear spin-density-wave antiferromagnetism in FeAs," *Phys. Rev. B*, vol. 83, no. 13, p. 134438, 2011.

[47] E. Hüger and K. Osuch, "Ferromagnetism in hexagonal close-packed Pd," *Europhys. Lett.*, vol. 63, no. 1, pp. 90–96, 2003.

[48] S. Ran, C. Eckberg, Q.-P. Ding, Y. Furukawa, T. Metz, S. R. Saha, I.-L. Liu, M. Zic, H. Kim, J. Paglione, and N. P. Butch, "Nearly ferromagnetic spin-triplet superconductivity," *Science*, vol. 365, no. 6454, pp. 684–687, 2019.

[49] Z. Qu, L. Spinu, H. Yuan, V. Dobrosavljević, W. Bao, J. W. Lynn, M. Nicklas, J. Peng, T. Liu, D. Fobes, E. Flesch, and Z. Q. Mao, "Unusual heavy-mass nearly ferromagnetic state with a surprisingly large Wilson ratio in the double layered ruthenates $(Sr_{1-x}Ca_x)_3Ru_2O_7$," *Phys. Rev. B*, vol. 78, no. 18, p. 180407, 2008.

[50] A. S. Sefat, D. J. Singh, R. Jin, M. A. McGuire, B. C. Sales, and D. Mandrus, "Renormalized behavior and proximity of $BaCo_2As_2$ to a magnetic quantum critical point," *Phys. Rev. B*, vol. 79, p. 024512, 2009.

[51] R. Hadimani, Y. Melikhov, J. Snyder, and D. Jiles, "Determination of Curie temperature by Arrott plot technique in $Gd_5(Si_xGe_{1x})_4$ for x $>$ 0.575," *J. Magn. Magn. Mater.*, vol. 320, no. 20, pp. e696 – e698, 2008.

[52] A. B. Pippard, *Magnetoresistance in Metals*, vol. 2. Cambridge University Press, 1989.

[53] Y. Wang, K. Wang, J. Reutt-Robey, J. Paglione, and M. S. Fuhrer, "Breakdown of compensation and persistence of nonsaturating magnetoresistance in gated WTe_2 thin flakes," *Phys. Rev. B*, vol. 93, p. 121108, 2016.

[54] Royal Swedish Academy of Sciences, *The Discovery of Giant Magnetoresistance*, Oct 2007.

[55] Physics Web, *Colossal magnetoresistance*, Feb 1999.

[56] F. Tafti, Q. Gibson, S. Kushwaha, N. Haldolaarachchige, and R. J. Cava, "Resistivity plateau and extreme magnetoresistance in LaSb," *Nat. Phys.*, vol. 12, no. 3, p. 272, 2016.

[57] I. Pletikosić, M. N. Ali, A. Fedorov, R. J. Cava, and T. Valla, "Electronic structure basis for the extraordinary magnetoresistance in WTe_2," *Phys. Rev. Lett.*, vol. 113, no. 21, p. 216601, 2014.

[58] M. N. Ali, L. Schoop, J. Xiong, S. Flynn, Q. Gibson, M. Hirschberger, N. P. Ong, and R. J. Cava, "Correlation of crystal quality and extreme magnetoresistance of WTe_2," *Europhys. Lett.*, vol. 110, no. 6, p. 67002, 2015.

[59] P. N. Hai, S. Ohya, M. Tanaka, S. E. Barnes, and S. Maekawa, "Electromotive force and huge magnetoresistance in magnetic tunnel junctions," *Nature*, vol. 458, no. 7237, p. 489, 2009.

[60] C. Shekhar, A. K. Nayak, Y. Sun, M. Schmidt, M. Nicklas, I. Leermakers, U. Zeitler, Y. Skourski, J. Wosnitza, Z. Liu, Y. Chen, W. Schnelle, H. Borrmann, Y. Grin, C. Felser, and B. Yan, "Extremely large magnetoresistance and ultrahigh mobility in the topological Weyl semimetal candidate NbP," *Nat. Phys.*, vol. 11, no. 8, pp. 645–649, 2015.

[61] D. Wu, J. Liao, W. Yi, X. Wang, P. Li, H. Weng, Y. Shi, Y. Li, J. Luo, X. Dai, and Z. Fang, "Giant semiclassical magnetoresistance in high mobility $TaAs_2$ semimetal," *Appl. Phys. Lett.*, vol. 108, no. 4, p. 042105, 2016.

[62] I. A. Leahy, Y.-P. Lin, P. E. Siegfried, A. C. Treglia, J. C. W. Song, R. M. Nandkishore, and M. Lee, "Nonsaturating large magnetoresistance in semimetals," *P. Natl. Acad. Sci. USA*, vol. 115, no. 42, pp. 10570–10575, 2018.

[63] N. Alekseevskii and Y. P. Gaidukov, "Measurement of the electrical resistance of metals in a magnetic field as a method of investigating the Fermi surface," *J. Exp. Theor. Phys.*, vol. 9, p. 311, 1959.

[64] J. Sólyom, *Fundamentals of the Physics of Solids: Volume II: Electronic Properties*, vol. 2. Springer Science & Business Media, 2008.

[65] A. Husmann, J. Betts, G. Boebinger, A. Migliori, T. Rosenbaum, and M.-L. Saboungi, "Megagauss sensors," *Nature*, vol. 417, no. 6887, p. 421, 2002.

[66] A. L. Friedman, J. L. Tedesco, P. M. Campbell, J. C. Culbertson, E. Aifer, F. K. Perkins, R. L. Myers-Ward, J. K. Hite, C. R. Eddy, G. G. Jernigan, and D. K. Gaskill, "Quantum Linear Magnetoresistance in Multilayer Epitaxial Graphene," *Nano Lett.*, vol. 10, no. 10, pp. 3962–3965, 2010.

[67] J. Babiskin and P. Siebenmann, "Saturating and linear magnetoresistive effects in sodium and potassium," *Physik Kondens. Mater.*, vol. 9, no. 1, pp. 113–121, 1969.

[68] T. Amundsen and P. Jerstad, "Linear magnetoresistance of aluminum," *J. Low Temp. Phys.*, vol. 15, no. 5, pp. 459–471, 1974.

[69] H. Taub, R. L. Schmidt, B. W. Maxfield, and R. Bowers, "Study of the Transverse Magnetoresistance of Polycrystalline Potassium," *Phys. Rev. B*, vol. 4, pp. 1134–1152, 1971.

[70] J. Hu and T. Rosenbaum, "Classical and quantum routes to linear magnetoresistance," *Nat. Mater.*, vol. 7, no. 9, p. 697, 2008.

[71] M. Parish and P. Littlewood, "Non-saturating magnetoresistance in heavily disordered semiconductors," *Nature*, vol. 426, no. 6963, p. 162, 2003.

[72] F. Kisslinger, C. Ott, and H. B. Weber, "Origin of nonsaturating linear magnetoresistivity," *Phys. Rev. B*, vol. 95, p. 024204, 2017.

[73] J. C. W. Song, G. Refael, and P. A. Lee, "Linear magnetoresistance in metals: Guiding center diffusion in a smooth random potential," *Phys. Rev. B*, vol. 92, p. 180204, 2015.

[74] A. Narayanan, M. D. Watson, S. F. Blake, N. Bruyant, L. Drigo, Y. L. Chen, D. Prabhakaran, B. Yan, C. Felser, T. Kong, P. C. Canfield, and A. I. Coldea, "Linear Magnetoresistance Caused by Mobility Fluctuations in n-Doped Cd_3As_2," *Phys. Rev. Lett.*, vol. 114, p. 117201, 2015.

[75] T. Shibauchi, A. Carrington, and Y. Matsuda, "A Quantum Critical Point Lying Beneath the Superconducting Dome in Iron Pnictides," *Annu. Rev. Conden. Ma. P.*, vol. 5, no. 1, pp. 113–135, 2014.

[76] I. M. Hayes, R. D. McDonald, N. P. Breznay, T. Helm, P. J. Moll, M. Wartenbe, A. Shekhter, and J. G. Analytis, "Scaling between magnetic field and temperature in the high-temperature superconductor $BaFe_2(As_{1-x}P_x)_2$," *Nat. Phys.*, vol. 12, no. 10, pp. 916–919, 2016.

[77] P. Giraldo-Gallo, J. A. Galvis, Z. Stegen, K. A. Modic, F. F. Balakirev, J. B. Betts, X. Lian, C. Moir, S. C. Riggs, J. Wu, A. T. Bollinger, X. He, I. Božović, B. J. Ramshaw, R. D. McDonald, G. S. Boebinger, and A. Shekhter, "Scale-invariant magnetoresistance in a cuprate superconductor," *Science*, vol. 361, no. 6401, pp. 479–481, 2018.

[78] A. A. Abrikosov, "Quantum magnetoresistance," *Phys. Rev. B*, vol. 58, pp. 2788–2794, 1998.

[79] Y. Luo, H. Li, Y. M. Dai, H. Miao, Y. G. Shi, H. Ding, A. J. Taylor, D. A. Yarotski, R. P. Prasankumar, and J. D. Thompson, "Hall effect in the extremely large magnetoresistance semimetal WTe_2," *Appl. Phys. Lett.*, vol. 107, no. 18, p. 182411, 2015.

[80] D. Shoenberg, *Magnetic Oscillations in Metals*. Cambridge, United Kingdom: Cambridge University Press, 1984.

[81] N. Garcia, Y. H. Kao, and M. Strongin, "Galvanomagnetic studies of bismuth films in the quantum-size-effect region," *Phys. Rev. B*, vol. 5, pp. 2029–2039, 1972.

[82] P. M. C. Rourke and S. R. Julian, "Numerical extraction of de Haas–van Alphen frequencies from calculated band energies," *Comput. Phys. Commun.*, vol. 183, no. 2, pp. 324–332, 2012.

[83] P. C. Canfield and Z. Fisk, "Growth of single crystals from metallic fluxes," *Philos. Mag. B*, vol. 65, no. 6, pp. 1117–1123, 1992.

[84] H. Okamoto, *Phase diagrams for binary alloys*, vol. 44. Materials Park, Ohio: ASM International, 2010.

[85] M. Binnewies, R. Glaum, M. Schmidt, and P. Schmidt, *Chemische Transportreaktionen*. Berlin, Germany: Walter de Gruyter, 2011.

[86] F. J. Di Salvo, D. Moncton, and J. Waszczak, "Electronic properties and superlattice formation in the semimetal $TiSe_2$," *Phys. Rev. B*, vol. 14, no. 10, p. 4321, 1976.

[87] L. Zhao, H. Deng, I. Korzhovska, M. Begliarbekov, Z. Chen, E. Andrade, E. Rosenthal, A. Pasupathy, V. Oganesyan, and L. Krusin-Elbaum, "Emergent surface superconductivity in the topological insulator Sb_2Te_3," *Nat. Commun.*, vol. 6, p. 8279, 2015.

[88] J. Martin and R. Gruehn, "Synthesis of transition metal phosphides form their oxides using the chemical transport (CVT) method," *Solid State Ionics*, vol. 43, pp. 19 – 22, 1990.

[89] A. E. Böhmer, V. Taufour, W. E. Straszheim, T. Wolf, and P. C. Canfield, "Variation of transition temperatures and residual resistivity ratio in vapor-grown FeSe," *Phys. Rev. B*, vol. 94, p. 024526, 2016.

[90] Quantum Design, San Diego, California, *PPMS DynaCool Options Manual*, 25 ed., 2014.

[91] Quantum Design, San Diego, California, *MPMS 3 User's Manual*, 15 ed., 2016.

[92] J. Brugger, M. Despont, C. Rossel, H. Rothuizen, P. Vettiger, and M. Willemin, "Microfabricated ultrasensitive piezoresistive cantilevers for torque magnetometry," *Sensors Actuat. A: Phys.*, vol. 73, no. 3, pp. 235 – 242, 1999.

[93] C. Rossel, P. Bauer, D. Zech, J. Hofer, M. Willemin, and H. Keller, "Active microlevers as miniature torque magnetometers," *J. Appl. Phys.*, vol. 79, no. 11, pp. 8166–8173, 1996.

[94] J. R. Jeffries, N. P. Butch, H. Cynn, S. R. Saha, K. Kirshenbaum, S. T. Weir, Y. K. Vohra, and J. Paglione, "Interplay between magnetism, structure, and strong electron-phonon coupling in binary FeAs under pressure," *Phys. Rev. B*, vol. 83, no. 13, p. 134520, 2011.

[95] K. Segawa and Y. Ando, "Magnetic and transport properties of FeAs single crystals," *J. Phys. Soc. Jpn.*, vol. 78, no. 10, pp. 104720–104720, 2009.

[96] E. E. Rodriguez, C. Stock, K. Krycka, C. Majkrzak, P. Zajdel, K. Kirshenbaum, N. Butch, S. R. Saha, J. Paglione, and M. A. Green, "Noncollinear spin-density-wave antiferromagnetism in FeAs," *Phys. Rev. B*, vol. 83, no. 13, p. 134438, 2011.

[97] H. Ido, N. M. Hong, O. Nashima, and T. Suzuki, "Weak ferromagnetism in $Cr_{1-x}Fe_xAs$ compound system," *Physica B*, vol. 237, pp. 164–166, 1997.

[98] T. Frawley, R. Schoonmaker, S. H. Lee, C.-H. Du, P. Steadman, J. Strempfer, K. A. Ziq, S. J. Clark, T. Lancaster, and P. D. Hatton, "Elucidation of the helical spin structure of FeAs," *Phys. Rev. B*, vol. 95, no. 6, p. 064424, 2017.

[99] D. Parker and I. I. Mazin, "Non-nesting spin-density-wave antiferromagnetism in FeAs from first principles," *Phys. Rev. B*, vol. 83, no. 18, p. 180403, 2011.

[100] S. M. Griffin and N. A. Spaldin, "A density functional theory study of the influence of exchange-correlation functionals on the properties of FeAs," *J. Phys.: Condens. Mat.*, vol. 29, no. 21, p. 215604, 2017.

[101] S. Khim, M. Gillig, R. Klingeler, S. Wurmehl, B. Büchner, and C. Hess, "Unusual magnetotransport properties in a FeAs single crystal," *Phys. Rev. B*, vol. 93, no. 20, p. 205129, 2016.

[102] A. Błachowski, K. Ruebenbauer, J. Żukrowski, and Z. Bukowski, "Magnetic anisotropy and lattice dynamics in FeAs studied by Mössbauer spectroscopy," *J. Alloy Cmpd.*, vol. 582, pp. 167 – 176, 2014.

[103] A. Carrington, A. I. Coldea, J. D. Fletcher, N. E. Hussey, C. M. J. Andrew, A. F. Bangura, J. G. Analytis, J. H. Chu, A. S. Erickson, I. R. Fisher, and R. D. McDonald, "Quantum oscillation studies of the Fermi surface of LaFePO," *Physica C*, vol. 469, no. 9, pp. 459–468, 2009.

[104] B. Vignolle, D. Vignolles, D. LeBoeuf, S. Lepault, B. Ramshaw, R. Liang, D. A. Bonn, W. N. Hardy, N. Doiron-Leyraud, A. Carrington, N. Hussey, L. Taillefer, and C. Proust, "Quantum oscillations and the Fermi surface of high-temperature cuprate superconductors," *C.R. Phys.*, vol. 12, no. 5-6, pp. 446–460, 2011.

[105] S. E. Sebastian, J. Gillett, N. Harrison, P. H. C. Lau, D. J. Singh, C. H. Mielke, and G. G. Lonzarich, "Quantum oscillations in the parent magnetic phase of an iron arsenide high temperature superconductor," *J. Phys.-Condens. Mat.*, vol. 20, no. 42, p. 422203, 2008.

[106] J. G. Analytis, R. D. McDonald, J.-H. Chu, S. C. Riggs, A. F. Bangura, C. Kucharczyk, M. Johannes, and I. R. Fisher, "Quantum oscillations in the parent pnictide $BaFe_2As_2$: itinerant electrons in the reconstructed state," *Phys. Rev B*, vol. 80, no. 6, p. 064507, 2009.

[107] T. Terashima, N. Kurita, M. Kimata, M. Tomita, S. Tsuchiya, M. Imai, A. Sato, K. Kihou, C.-H. Lee, H. Kito, H. Eisaki, A. Iyo, T. Saito, H. Fukazawa, Y. Kohori, H. Harima, and S. Uji, "Fermi surface in KFe_2As_2 determined via de Haas-van Alphen oscillation measurements," *Phys. Rev. B*, vol. 87, no. 22, p. 224512, 2013.

[108] Y. Nakajima, R. Wang, T. Metz, X. Wang, L. Wang, H. Cynn, S. T. Weir, J. R. Jeffries, and J. Paglione, "High-temperature superconductivity stabilized by electron-hole interband coupling in collapsed tetragonal phase of KFe_2As_2 under high pressure," *Phys. Rev. B*, vol. 91, p. 060508, 2015.

[109] A. S. Sefat, M. A. McGuire, R. Jin, B. C. Sales, D. Mandrus, F. Ronning, E. D. Bauer, and Y. Mozharivskyj, "Structure and anisotropic properties of $BaFe_{2-x}Ni_xAs_2$ (x = 0, 1, and 2) single crystals," *Phys. Rev. B*, vol. 79, p. 094508, 2009.

[110] C. R. Rotundu, B. Freelon, T. R. Forrest, S. D. Wilson, P. N. Valdivia, G. Pinuellas, A. Kim, J.-W. Kim, Z. Islam, E. Bourret-Courchesne, N. E. Phillips, and R. J. Birgeneau, "Heat capacity study of $BaFe_2As_2$: Effects of annealing," *Phys. Rev. B*, vol. 82, p. 144525, 2010.

[111] T. Nozue, H. Kobayashi, N. Kimura, H. Aoki, and T. Kamimura, "de Haas-van Alphen effect of FeP in double helical magnetic state," *J. Phys. Soc. Japan*, vol. 70, no. 1, pp. 192–198, 2001.

[112] Q. Niu, W. C. Yu, E. I. P. Aulestia, Y. J. Hu, K. T. Lai, H. Kotegawa, E. Matsuoka, H. Sugawara, H. Tou, D. Sun, F. F. Balakirev, Y. Yanase, and S. K. Goh, "Nonsaturating large magnetoresistance in the high carrier density nonsymmorphic metal CrP," *Phys. Rev. B*, vol. 99, p. 125126, 2019.

[113] S. Sun, Q. Wang, P.-J. Guo, K. Liu, and H. Lei, "Large magnetoresistance in LaBi: origin of field-induced resistivity upturn and plateau in compensated semimetals," *New J. Phys.*, vol. 18, no. 8, p. 082002, 2016.

[114] D. Bellavance, M. Vlasse, B. Morris, and A. Wold, "Preparation and properties of iron monophosphide," *J. Solid State Chem.*, vol. 1, no. 1, pp. 82 – 87, 1969.

[115] M. W. Richardson and B. I. Noläng, "Predicting the rate of chemical transport using the flux function method," *J. Cryst. Growth*, vol. 42, pp. 90 – 97, 1977.

[116] P. Syers and J. Paglione, "Ambipolar surface state transport in nonmetallic stoichiometric Bi_2Se_3 crystals," *Phys. Rev. B*, vol. 95, no. 4, p. 045123, 2017.

[117] A. Takase and T. Kasuya, "Temperature dependences of electrical resistivity in MnP," *J. Phys. Soc. Japan*, vol. 48, no. 2, pp. 430–434, 1980.

[118] X. H. Chen, Y. S. Wang, Y. Y. Xue, R. L. Meng, Y. Q. Wang, and C. W. Chu, "Correlation between the residual resistance ratio and magnetoresistance in MgB_2," *Phys. Rev. B*, vol. 65, p. 024502, 2001.

[119] A. Takase and T. Kasuya, "High Field Magnetoresistance in MnP," *J. Phys. Soc. Jpn.*, vol. 49, no. 2, pp. 489–492, 1980.

[120] A. Nigro, P. Marra, C. Autieri, W. Wu, J. Cheng, J. Luo, and C. Noce, "Resistivity measurements unveil microscopic properties of CrAs," *Europhys. Lett.*, vol. 125, p. 57002, apr 2019.

[121] Y. L. Wang, L. R. Thoutam, Z. L. Xiao, J. Hu, S. Das, Z. Q. Mao, J. Wei, R. Divan, A. Luican-Mayer, G. W. Crabtree, and W. K. Kwok, "Origin of the turn-on temperature behavior in WTe_4," *Phys. Rev. B*, vol. 92, p. 180402, 2015.

[122] N. H. Jo, Y. Wu, L.-L. Wang, P. P. Orth, S. S. Downing, S. Manni, D. Mou, D. D. Johnson, A. Kaminski, S. L. Bud'ko, and P. C. Canfield, "Extremely large magnetoresistance and Kohler's rule in $PdSn_4$: A complete study of thermodynamic, transport, and band-structure properties," *Phys. Rev. B*, vol. 96, p. 165145, 2017.

[123] F. Fallah Tafti, Q. Gibson, S. Kushwaha, J. W. Krizan, N. Haldolaarachchige, and R. J. Cava, "Temperature-field phase diagram of extreme magnetoresistance," *Proceedings of the National Academy of Sciences*, vol. 113, no. 25, pp. E3475–E3481, 2016.

[124] O. Pavlosiuk, P. Swatek, and P. Wiśniewski, "Giant magnetoresistance, three-dimensional Fermi surface and origin of resistivity plateau in YSb semimetal," *Sci. Rep.*, vol. 6, p. 38691, 2016.

[125] A. E. Koshelev, "Linear magnetoconductivity in multiband spin-density-wave metals with nonideal nesting," *Phys. Rev. B*, vol. 88, p. 060412, 2013.

[126] P. C. Canfield and S. L. Budko, "Preserved entropy and fragile magnetism," *Rep. Prog. Phys.*, vol. 79, no. 8, p. 084506, 2016.

[127] P. Lyman and C. Prewitt, "Room-and high-pressure crystal chemistry of CoAs and FeAs," *Acta Crystallogr. B*, vol. 40, no. 1, pp. 14–20, 1984.

[128] K. Tanaka, S. K. Suri, and A. L. Jain, "Galvanomagnetic Effects in Antimony," *Phys. Rev.*, vol. 170, pp. 664–667, 1968.

[129] A. Bauer, A. Regnat, C. G. F. Blum, S. Gottlieb-Schönmeyer, B. Pedersen, M. Meven, S. Wurmehl, J. Kuneš, and C. Pfleiderer, "Low-temperature properties of single-crystal CrB_2," *Phys. Rev. B*, vol. 90, p. 064414, 2014.

[130] R. Blachnik, G. Kudermann, F. Grønvold, A. Alles, B. Falk, and E. F. Westrum, "CrAs: heat capacity, enthalpy increments, thermodynamic properties from 5 to 1280 K, and transitions," *J. Chem. Thermodyn.*, vol. 10, no. 6, pp. 507–522, 1978.

[131] A. Takase, H. Yashima, and T. Kasuya, "Low Temperature Specific Heat of MnP; Experiment and Analysis," *J. Phys. Soc. Jpn.*, vol. 47, no. 2, pp. 531–534, 1979.

[132] A. Jesche, K. W. Dennis, A. Kreyssig, and P. C. Canfield, "Nearly itinerant ferromagnetism in $CaNi_2$ and $CaNi_3$," *Phys. Rev. B*, vol. 85, p. 224432, 2012.

[133] S. Doniach and S. Engelsberg, "Low-Temperature Properties of Nearly Ferromagnetic Fermi Liquids," *Phys. Rev. Lett.*, vol. 17, pp. 750–753, 1966.

[134] R. J. Trainor, M. B. Brodsky, and H. V. Culbert, "Specific Heat of the Spin-Fluctuation System UAl_2," *Phys. Rev. Lett.*, vol. 34, pp. 1019–1022, 1975.

[135] K. Motizuki, "Recent advances in the theory of magnetism of NiAs-type transition-metal chalcogenides and pnictides," *J. Magn. Magn. Mater.*, vol. 70, no. 1, pp. 1 – 7, 1987.

[136] L. H. Lewis and J. B. Goodenough, "Metal-metal versus anion-anion bonding in B31 structures," *J. App. Phys.*, vol. 73, no. 10, pp. 5704–5706, 1993.

[137] K. Schwarz, P. Blaha, and G. K. H. Madsen, "Electronic structure calculations of solids using the WIEN2k package for material sciences," *Comput. Phys. Commun.*, vol. 147, no. 1-2, pp. 71–76, 2002.

[138] F.-C. Hsu, J.-Y. Luo, K.-W. Yeh, T.-K. Chen, T.-W. Huang, P. M. Wu, Y.-C. Lee, Y.-L. Huang, Y.-Y. Chu, D.-C. Yan, and M.-K. Wu, "Superconductivity in the PbO-type structure α-FeSe," *Proc. Natl. Acad. Sci. USA*, vol. 105, no. 38, pp. 14262–14264, 2008.

[139] X. Zhou, B. Wilfong, H. Vivanco, J. Paglione, C. M. Brown, and E. E. Rodriguez, "Metastable Layered Cobalt Chalcogenides from Topochemical Deintercalation," *J. Am. Chem. Soc.*, vol. 138, no. 50, pp. 16432–16442, 2016.

[140] P. Amornpitoksuk, D. Ravot, A. Mauger, and J. C. Tedenac, "Structural and magnetic properties of the ternary solid solution between CoSb and $Fe_{1+\delta}Sb$," *Phys. Rev. B*, vol. 77, p. 144405, 2008.

[141] K. Selte, L. Birkeland, and A. Kjekshus, "On the Structural and Magnetic Properties of $Cr_{1-t}Fe_tP$, $Mn_{1-t}Co_tP$, and $Fe_{1-t}Co_tP$," *Acta Chem. Scand.*, vol. 32A, no. 8, pp. 731–735, 1978.

[142] A. Schmidt and R. Glaum, "Zum chemischen Transport von Cobaltmonophosphid mit Iod. Experimente und Modellrechnungen," *Z. Anorg. Allg. Chem.*, vol. 621, no. 10, pp. 1693–1702, 1995.

[143] D. Hirai, T. Takayama, D. Hashizume, and H. Takagi, "Metal-insulator transition and superconductivity induced by Rh doping in the binary pnictides RuPn Pn = P, As, Sb)," *Phys. Rev. B*, vol. 85, p. 140509, 2012.

[144] J. R. Jeffries, N. P. Butch, H. Cynn, S. R. Saha, K. Kirshenbaum, S. T. Weir, Y. K. Vohra, and J. Paglione, "Interplay between magnetism, structure, and strong electron-phonon coupling in binary FeAs under pressure," *Phys. Rev. B*, vol. 83, no. 13, p. 134520, 2011.

[145] C. Raub, W. Zachariasen, T. Geballe, and B. Matthias, "Superconductivity of some new Pt-metal compounds," *J. Phys. Chem. Solids*, vol. 24, no. 9, pp. 1093 – 1100, 1963.

[146] S. Rundqvist and T. Lundstrom, "X-ray studies of molybdenum and tungsten phosphides," *Acta Chem. Scand*, vol. 17, p. 37, 1963.